Evaluation of the UCL Compton Camera Imaging Performance

Mashari A. Alnaaimi

Submitted for the Degree of
Doctor of Philosophy
From the
University College London

RADIATION PHYSICS GROUP
DEPARTMENT OF MEDICAL PHYSICS AND BIOENGINEERING
FACULATY OF ENGINEERING SCIENCES
UNIVERSITY COLLEGE LONDON

July 2011

I, Mashari AlNaaimi, confirm that the work presented in this thesis is my own. Where information has been derived from other sources, I confirm that this has been indicated in the thesis.

بسم الله الرحمن الرحيم

In The Name Of Allah the Beneficent the Merciful

Dedicated to my beloved wife and kids

Acknowledgments

I sincerely wish to thank my principal supervisors Dr Gary Royle and Professor Robert Speller for the endless levels of support, advice and encouragement they have bestowed both academically, and as friends over the duration of the course.

I greatly appreciate the support of the Radiation Physics group as the advice sought was priceless. In particular, thanks go to Mr. Ahmad Subahi as he always brought a smile to my face and is a sincere friend who provides a constant support both at work and in everyday life; Mr Walid Ghoggali for his endless support and suggestions which made my work stronger and Mr Essam Banoqitah for being extremely friendly and helpful. A special thank you is also reserved to Dr Alassandro Olivo who unselfishly contributes to the other individuals in the group with kind advice and knowledge; Dr. Ian Cullum for providing me with the radioisotopes and advising me with his professional experience.

Finally, I would like to say a very special thank you to my family and especially my parents and wife as without their constant stream of love, I could not have dreamed of completing such a task.

Publications

1. M A Alnaaimi G J Royle, W Ghoggali, and R D Speller. 2010 Development of a pixellated germanium Compton camera for nuclear medicine 2010 IEEE Nuclear Science Symposium Conference Record N41-150 pp 1104-1107.

2. M A Alnaaimi G J Royle, W Ghoggali, E Banoqitah, I Cullum and R D Speller 2011 Performance evaluation of a pixellated Ge Compton camera *Phys. Med. Biol.* **56** 3473-3486 (Featured Article)

Abstract

This thesis presents the imaging performance of the University College London (UCL) High Purity Germanium (HPGe) Compton camera. This work is a part of an ongoing project to develop a Compton camera for medical applications. The Compton camera offers many potential advantages over other imaging modalities used in nuclear medicine. These advantages include a wide field of view, the ability to reconstruct 3D images without tomography, and the fact that the camera can have a portable lightweight design due to absence of heavy collimation.

The camera was constructed by ORTEC and the readout electronics used are based on GRT4 electronics boards (Daresbury, UK). The camera comprises two pixellated germanium detector planes housed 9.6 cm apart in the same vacuum housing. The camera has 177 pixels, 152 in the scatter detector and 25 in the absorption detector. The pixels are 4x4 mm^2.

The imaging performance with different gamma-ray source energies was evaluated experimentally and compared to the theoretical estimations. Images have been taken for a variety of test objects including point, ring source and Perspex cylindrical phantom. The measured angular resolution is 7.8° ± 0.4 for 662 keV gamma-ray source at 5 cm. Due to the limited number of readout modules a multiple-view technique was used to image the source distributions from different angles and simulate the pixel arrangement in the full camera. In principle, the Compton camera potentially has high sensitivity but this is not recognized in practice due to the limited maximum count rate.

Although there are a number of limitations in the current prototype camera some potentially useful qualities have been demonstrated and distributed sources have been imaged. The key limitations in the current prototype are acquisition time, processing time and image

reconstruction. However, techniques are available to significantly improve and overcome these limitations. This thesis presents the current state of the Compton camera performance along with a demonstration of its strengths and limitations as a potential candidate for nuclear medicine imaging.

Contents

List of Figures

List of Tables

List of Abbreviations

a.u.	Atomic unit
Ba	Barium
BD	Back detector
BP	Back projection
Cm	Centimetre
Cs	Cesium
CT	Computed tomography
E	Energy
FD	Front detector
FPGA	Field-Programmable Gate Array
FWHM	Full Width Half Maximum
FWTM	Full Width tenth Maximum
HEGP	High Energy General Purpose
keV	Kilo-electron volts
LEGP	Low Energy General Purpose
LOR	Line of response
MLEM	Maximum likelihood expectation maximisation
mm	Millimetre
MRI	Magnetic Resonance Imaging
Na	Sodium
NECR	Noise equivalent count rate
NIST	National institute of standards and technology
PET	Positron emission tomography
PSF	Point spread function
SNR	Signal to noise ratio
SPECT	Single photon emission tomography
UCL	University College London

Chapter 1

1 Introduction

1.1 Principle of gamma-ray imaging in Nuclear Medicine

Nuclear Medicine is a very important branch of medical imaging which utilizes gamma-ray emitting radionuclide to obtain information about the physiology of the organs within the human body as well as the detection of tumour growth sites. This is done by introducing the radioactive labelled substance into the patient body and placing the patient around external radiation detectors. These radioactive labelled substances, which are called radiotracers, can then be used to track physiological processes *in vivo* typically imaged using a gamma camera (Sorenson and Phelps 1987).

The radiotracers participate in the biochemical or physiological processes in the body in the same way as the non-radioactive material. Since the emitted γ-rays from the radioactive material can be detected by an external camera, radiotracers may be used to track the flow or distribution of analogs of natural substances in the body.

There are two major types of radiotracers used: single photon emitters and positron emitters. Single photon emitters may emit one principal gamma ray or a sequence of gamma-rays that are directionally uncorrelated. On the other hand, positron emitters emit a positron that travels a short distance and annihilates with an electron. This annihilation generates two 511keV gamma rays, which travel in opposite directions.

Gamma camera uses mechanical collimators to project the γ-rays from single photon emitters onto the scintillation detector to have a one-to-one spatial correlation between points of emission and detection to accurately form the image. This is done by allowing only photons travelling in a specific direction to be detected otherwise they will be absorbed by the collimator before reaching the detector. The gamma camera 3-dimensional imaging mode is called the Single Photon Emission Computed Tomography (SPECT). SPECT is an extension of planar gamma camera imaging. The three-dimensional distributions of radiotracers within the body are estimated from a set of two-dimensional projection images acquired by planar cameras from a number of views surrounding the patient more details will be discussed in section 1.2.

The PET scanner is used to image radio-nuclides that decay by positron emission. The positron combines with an electron resulting in emission of a pair of gamma-rays travelling in opposite directions as will be discussed in (section 1.3).

There are many limitations in SPECT and PET. The spatial resolution of SPECT images deteriorates with high energy radioisotopes where the detection efficiency and spatial resolution becomes low due to the collimator design and NaI crystal limitation. Moreover, because of the heavy lead collimator gamma camera is practically difficult to be portable.

The main limitations of PET are the high cost and the almost exclusive dependence on cyclotron produced short half-life radioisotopes. Therefore, it is very important to develop alternative methods for gamma-rays imaging that can be used to image positron emitters with lower costs. Compton camera is a promising imaging technique that can be used to provide an alternative for PET and SPECT providing a portable imaging system for high energy (>300 keV) radioisotopes.

In the UCL effort is on the go to produce a pixellated high purity germanium (HPGe) Compton camera imaging system for medical application to overcome some of gamma camera and PET limitations. The motivation is to develop a compact portable imaging system to image gamma-ray emissions in nuclear medicine examinations with high spatial resolution and detection sensitivity. In this work the aim is to present and quantitatively evaluate the imaging performance of the UCL Compton camera and compare it to other systems currently used in nuclear medicine in order to bring into focus its potential benefits in this field.

This chapter describes the principle, applications, and limitations of imaging modalities used in nuclear medicine. In addition, the Compton camera principle, advantages, and a literature review for the most significant contributions in this field are presented in this chapter.

1.2 Mechanical collimation (Gamma camera)

The most commonly used imaging instrument in nuclear medicine is the gamma camera which was developed by Anger (1958). The gamma camera makes use of a scintillation crystal, which is usually made of NaI(Tl), optically coupled to a photomultiplier tubes (PMTs). The gamma camera makes use of collimators to project the gamma rays from the source distribution onto the scintillation detector to have a one-to-one spatial correlation between points of emission and detection for accurate image formation. This is done by allowing only photons travelling in a certain direction to be detected otherwise they will be absorbed by the collimator before reaching the detector. The gamma rays are converted into flashes of light by the NaI(Tl) crystal which is then transformed to electronic signals by the PMTs. The output of the PMTs is then converted into three signals: (X and Y) that give the spatial location of the scintillation and (Z) which gives

the energy deposited in the crystal by gamma ray. The basic component of gamma camera is shown in Figure 1.

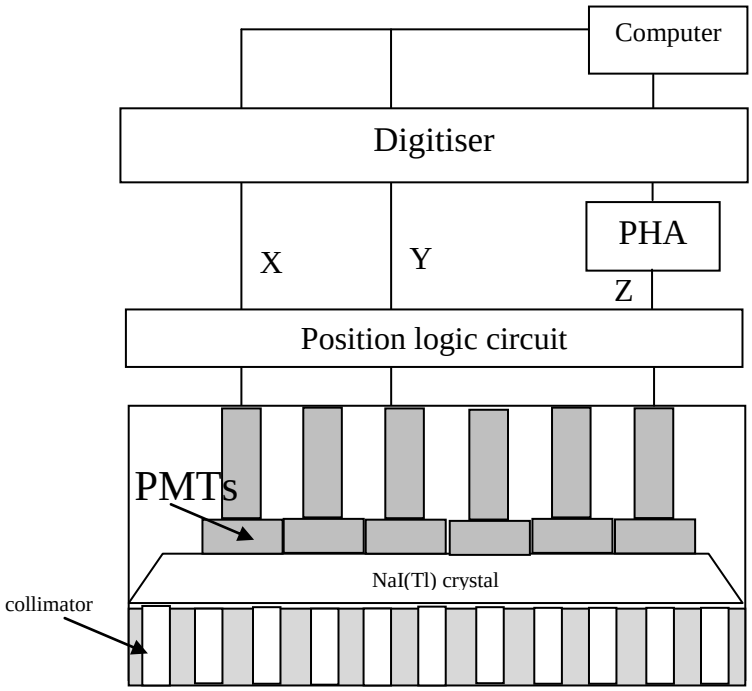

Figure 1: The basic component of a gamma camera.

Moreover, the detection efficiency of the gamma camera is a function of the incident source energy: for source energy equals to 150 keV the camera efficiency ≈ 90%, but for source energy more than 400keV the detection efficiency ≈ 20%.

The collimation method used in gamma camera results in low system sensitivity due to the rejection of many useful photons travelling toward the detector which is the main reason of the poor quality of the images produced with gamma camera compared to radiographic images (Sorenson and Phelps 1987). The collimator defines the system spatial resolution and sensitivity as shown in Table 1. There is a trade-off between collimator resolution and sensitivity such that if greater sensitivity is required, then the hole size needs to be increased or the hole length must be shortened. Either of these choices results in degrading the spatial resolution of images. If only photons with directions near to the ideal are selected by reducing the size of hole or increasing the

length, then the sensitivity is reduced and the counting statistics will be reduced. Therefore, collimators with good spatial resolution but poor sensitivity are called *high-resolution collimators*, but those with opposite features are called *high-sensitivity collimators*.

Collimator type	Recommended maximum energy (keV)	Collimator sensitivity	Collimator resolution (FWHM at 10 cm)
Low energy high resolution	150	1.84×10^{-4}	7.4mm
Low energy general purpose	150	2.68×10^{-4}	9.1mm
Low energy high sensitivity	150	5.74×10^{-4}	13.2mm
Medium energy high sensitivity	400	1.72×10^{-4}	13.4mm

Table 1: The performance characteristics of typical commercially available parallel-hole collimators .

A common gamma camera imaging procedure is the SPECT scan which provides a powerful tool for disease recognition and monitoring especially in cardiology and oncology. This is done by rotating the gamma camera 180° or 360° around the patient region of interest to acquire a set of two-dimensional projection images from different views around the patient. Then a mathematical method of creating transaxial slices from the projections views e.g. filtered back projection or iterative reconstruction is applied to reconstruct the image. However, the presence of mechanical collimator limits the performance of SPECT (R. J. Ott 1996).

1.3 Dual photon electronic collimation (PET)

The PET scanner, which is used to image positron emitters isotopes, is usually designed with a ring of detectors to detect the paired 511 keV annihilation photons. Positron emitters are isotopes of some elements C^{11}, N^{13}, O^{15}, and F^{18} of natural metabolites (such

as glucose, water, and ammonia). For that reason, it is possible to label biological carriers without changing their structure and behaviour. PET provides a great diagnostic means for many medical applications including cardiology, neurology, and oncology. A photograph of a Siemens Biograph PET system is shown in as shown in Figure 2.

The first positron emitter imaging was carried out in the early fifties by (Brownell and Sweet 1953) with NaI(Tl) detector. Since then, different detectors types and numbers have been used for the PET system. Most of PET scanners nowadays are accompanied by a CT scanner in the same machine to be used for the attenuation correction and to provide information about the structural anatomy to provide a better diagnosis (M Pennant et al 2010). Originally, PET scanners have utilised bismuth germinate (BGO) scintillation crystals arranged into ring arrays. Many new dense scintillators with high speed and light output like LSO and $LaBr_3$ have been used to improve the performance of PET scanners (Daube-Witherspoon et al 2010, Bisogni et al 2011)

The image acquisition is based on the external detection of the 511 keV two annihilation photons, as a coincidence event. A true annihilation event requires a coincidence timing window (typically 4.5 nanoseconds) between two detectors on opposite sides of the scanner, hence "electronic collimation". For accepted coincidences, lines of response (LOR) connecting the coincidence detectors are drawn through the object and used in the image reconstruction. This method of detection achieves higher sensitivity and improved image quality compared to mechanically collimated gamma camera (Alberto Del Guerra and Belcari 2007). The spatial resolution of PET scanner depends on the type, size and the geometrical configuration of the detector elements. The spatial resolution and sensitivity of some commercially available PET scanners is presented in Table 2. In addition, the absence of mechanical collimators and the ring design let the field of view of the camera to cover large area (Rahmim and Zaidi 2008).

	Sensitivity (cps/kBq/cc)	Spatial resolution (mm)
PET Philips Gemini -Big bore	7.2	5.2
Siemens –Biograph TruePoint	7	4.8
GE Discovery- PET/CT 600	9.1	5.6

Table 2: The spatial resolution and sensitivity of some of the commercially available PET systems.

However, because PET scanners make use of short half life (usually a few minutes) positron emitters mostly produced from an accelerator and a nearby nuclear cyclotron is essential. In addition, the positron range and photon non-collinearity are inherent resolution-degrading factors in PET (Rahmim and Zaidi 2008). This makes a PET medical examination expensive and limis its routine availability and implementation on a large scale.

Figure 2: A photograph of a PET system (The Siemens Biograph mCT). The detectors form a ring around the patient to detect the annihilation gamma ray pairs.

In recent years, many efforts have been invested in the development of gamma-ray detectors to image high-energy photons and provide an alternative to the costly PET examination. One approach is the use of a dual-head gamma camera without the mechanical collimators with a custom electronics for coincidence detection; this method

is called the dual-headed coincidence imaging (DHCI). This method has improved the spatial resolution and sensitivity of the gamma camera (Patton and Turkington 1999). However, the sensitivity of the DHCI is lower than the PET system and is not sufficient to anatomically locate the uptake of the positron emitter in the body in a short acquisition time (Bergström et al 2010).

Another interesting approach is the use of Multi-wire proportional chambers (MWPCs) which have been used as a position sensitive charged particle detector in nuclear and high-energy physics (R. J. Ott 1993). MWPCs are large-area gas-filled ionization chambers in which large arrays of fine wires are used to determine the position of ionization produced in the gas by the passage of charged particles. Each wire functions as an individual ionization detector in their simplest form the anode and cathode planes. The main advantages of MWPCs are the high-count-rate performance, large area, high spatial resolution and low cost (Ott 1993). Several groups have worked on the development of MWPC detectors for positron emission tomography (Bateman et al. 1980; A. Del Guerra et al. 1988). Intrinsically the gas ionisation chambers have a very low efficiency for detecting gamma rays unless photon-electron convertor is incorporated. Lead is used as a convertor and proved to significantly increase the detection efficiency for 511 keV photons with minimal effect on the spatial resolution of the detector. A large area MWPC camera (MUP-PET) was installed in the Royal Marsden Hospital in Sutton and has been used successfully to measure the radiation dose to the thyroid (R. J. Ott et al. 1987). In addition, this system was used to plan targeted radionuclide therapy that was done by imaging I^{124} mIBG to provide treatment planning information for therapies of neural crest tumors with I^{131} mIBG (R. J. Ott et al. 1992) .

The main drawbacks of MWPCs are the low detection efficiency for 511 keV photons and the high minimum usable coincidence window (~30 ns) which lead to increase the

effect of scattered photons (Ott 1993). Nevertheless, the development of a hybrid system of barium fluoride (BaF2) scintillating crystals and MWPCs has shown great promise to overcome problems of sensitivity and timing resolution (K Wells et al 1994). This hybrid system retains the large area and high spatial resolution of the gaseous detectors but has 10 to 15 times improved sensitivity and a factor of 3 improved timing resolutions; thus, make it perfectly suited for the pre-therapy tracer studies and therapy planning based on pharmacokinetics (R. J. Ott 1996). Recently, Divoli et al. (2005) reported the improvement of this hybrid camera which has a spatial resolution of 7.5 mm, a timing resolution of 3.5 ns, and a total coincidence count-rate performance of at least 80–90 kcps. Preliminary phantom and patient images was presented. The count-rate performance is limited by the read-out electronics and computer system and the sensitivity by the use of thin (10 mm thick) crystals. These limitations are being addressed to improve the performance of the camera.

1.4 Recent advances in nuclear medicine imaging

This section summaries the performance and the recent ongoing development of the two main nuclear medicine studies namely the gamma camera SPECT imaging and PET. Their capabilities in terms of sensitivity and spatial resolution as well as their limitations will be presented to gain a better understanding of their impact on clinical practice. The ongoing developments are focusing mainly in enhancing the performance of PET and SPECT in terms of optimizing the hardware design (e.g. slit, slant, and pinhole collimators), software development (e.g. resolution modelling and compensation, dynamic image reconstruction), and data correction techniques (e.g. attenuation, random, scatter, partial volume, and motion correction) as discussed in (Rahmim and Zaidi 2008, Wells et al 2007, Wells et al 2010).

In SPECT, many approaches were carried out to optimize and develop novel collimator designs in order to increase the sensitivity. For example, Lodge et al (1996) and (Vandenberghe et al 2006) used a rotating slat instead of holes collimator which has larger solid angle of acceptance. Another approach used a smaller field of view (FOV) to gain sensitivity by using converging-hole collimator. One example is the use of rotating multi-segment slant-hole (RMSSH) collimators (Wagner et al 2002). The RMMSH collimators improved the sensitivity by a factor of 2 along with the additional advantage of achieving complete angle tomography with few camera positions, depending on the number of segments in the collimator. Thus, this technique is very useful for SPECT mammography (Brzymialkiewicz et al 2005). Another exciting example is the use of pinhole collimator to acquire SPECT images which has improved the spatial resolution to sub-millimetre scale, but at the expense of system sensitivity (Beekman and Have 2006). To compensate for the sensitivity loss multi-pinhole collimators have been proposed and used by (Vastenhouw and Beekman 2007).

Another area of increasing interest is the simultaneous dual-tracer SPECT imaging which is done by simultaneous imaging of different isotopes energies with multiple energy windows (Rahmim and Zaidi 2008). For example, the use of Tc^{99m} (140 keV) sestamibi stress scan and Tl^{201} (75 and 167 keV) rest myocardial perfusion imaging which results in reducing the acquisition time and increase the patient comfort. The problem of using this approach is the presence of crosstalk between the multiple energy windows. Current research is working on optimising the parameters of the multiple energy-windows (Jong et al 2002).

Moreover, the use of attenuation correction in SPECT is becoming increasingly important (Heller 2004) since the tissue thickness varies with different depths or regions within the patient body. Therefore, lack of attenuation correction can produce errors (artefacts) in

the reconstructed images and affect the quantitative accuracy of SPECT imaging. The introduction of the combined SPECT/CT scanners provides a convenient fast measurement of the X-rays transmission data that can be used for attenuation correction (Blankespoor et al 1996). However, the use of dual-modality system has introduced some artefacts like the misregistration of emission and transmission data due to the respiratory motion artefact (Goetze et al 2007), truncation artefact due to the discrepancies in the fields of view, and beam-hardening artefact caused by the polychromatic nature of the X-ray (Hsieh et al 2000). Recently, researchers are focusing on developing methods to compensate for these artefacts in statistical reconstruction methods (Zaidi and B Hasegawa 2003).

In PET, with the advances in technology and statistical reconstruction algorithms the factors that limit the resolution namely the positron range and photon non-collinearity can be modelled in the reconstruction task to further improve the reconstructed images resolution (Selivanov et al 2000). Moreover, the feasibility of improving PET resolution by application of strong magnetic field, which reduces the positron range, has been verified by (Christensen et al 1995). This approach has increased the interest in designing a combined PET/MRI system which is a potential very powerful technique (Pichler et al 2006).

It is worth noting that the development of fast scintillators such as lutetium oxyorthosilicate (LSO), lutetium yttrium oxyorthosilicate (LYSO) and Lanthanum three bromide (LaBr3) have permitted the coincidence timing window to be reduced to 2 ns compared to (10 -12 ns) with conventional bismuth germinate (BGO) scanners (Derenzo et al 2003, Moses 2003). This improvement will reduce the random events rate and improve the count rate performance in PET scanners. In addition, researches are ongoing to develop faster readout electronics e.g. the use of avalanche photodiodes (APDs) to

replace the bulky PMTs due to their high quantum efficiency, internal gain and insensitivity to magnetic field (Shah et al 2004, Pichler et al 2006). Also, silicon photomultipliers (SiPMs), which is a finely pixellated APD, became recently available commercially from several manufacturers and is potentially a promising candidate for use as photodetectors in PET (Moehrs et al 2006, Dolgoshein et al 2006).

With the constant improvements in the electronics and fast scintillators, the time-of-flight (ToF) PET ,which can measure the difference of the arrival times of the two annihilation photons, was recently reconsidered (Moses 2003, Conti et al 2005). Encoding the ToF information can potentially reduce statistical noise variance and improve the reconstruction of PET images. The first commercially available (ToF) PET scanner was produced by Philips medical systems manufacturer and its performance was presented in (Surti et al 2007).

In order to produce accurate quantitative data some corrections are very important to PET data like: random event corrections, scatter corrections, partial volume effect correction, and motion correction. These corrections are a subject of ongoing research in PET imaging (Rahmim and Zaidi 2008).

1.5 Project motivation and aim

- The Compton camera is a promising imaging system that can be used to provide an alternative for gamma camera and PET scanner and offers a portable imaging device.
- The motivation of this project is to develop a portable Compton camera to be used in nuclear medicine with high spatial resolution and detection sensitivity.

- The main aim of this project is to present and evaluate the imaging performance of the UCL pixellated Ge Compton camera and compare it to other cameras used in nuclear medicine to determine its potential benefits.

1.6 Single photons electronic collimation

Todd et al (1974), firstly, proposed the principle of using gamma camera to detect Compton scattered photons. The idea was to replace the conventional absorptive mechanical collimator with a second detector which works as an electronic collimation for the scattered photons by recording two photons detected within the preset time window which is called coincidence events.

In 1983, Singh and Doria built the first laboratory Compton camera device for medical use (M. Singh 1983; M. Singh & Doria 1983). They replaced the gamma camera mechanical collimator with a germanium detector which served as the front (scatter) detector of Compton camera and the NaI crystals of the gamma camera as the back (absorption) detector. This camera was evaluated and compared to the performance of the conventional gamma camera with mechanical collimation (M. Singh & Doria 1985). After the pioneering work of Singh and Doria many Compton camera designs and different detector types have been proposed and tested. The basic principle, applications, and potential advantages of Compton camera as well as a review of the literature will be presented in the following section.

1.7 The Principle of Compton Camera

A Compton camera is a type of gamma camera that makes uses of the kinematics of Compton scatter to build the image without using mechanical collimators. The mechanical collimator is replaced with a second detector which works in coincidence

with the first detector and electronically collimates the incident photons. A Compton camera is designed usually with two planar detectors and a specific distance is placed between them to choose a preferred range of scatter angles.

In a Compton imaging system, the incident photons interact with the first detector and Compton scatters from an electron in the detector. The scattered photon is then absorbed in the second detector. A Compton imaging system, therefore, decouples the trade-off between spatial resolution and detection efficiency that characterizes a conventional collimated gamma camera.

A cone, see figure 3, will be defined from each photon emission, if this photon interacts with the first detector by one Compton interaction and the scattered photon is then photoelectrically absorbed or deposits part of its energy in the second detector. The location of source is defined by backprojecting and intersecting all conic surfaces from many emitted photons in the image space. Hence, the likely position of the source can be somewhere on the surface of a cone, which creates serious uncertainty in the reconstruction (K Iniewski 2009). The cone semi-angle is the Compton scatter angle, thus if the source energy is known the angle between the incident and the scattered gamma ray photon direction can be determined from the energy of recoil electron measured in the front detector as given by (1.

$$\cos\theta = 1 - m_o c^2 \left(\frac{1}{E_\gamma - E_{re}} - \frac{1}{E_\gamma} \right)$$

(1)

where $m_o c^2$ is the electron rest mass (0.511 MeV), Eγ is the source energy and E_{re} is the recoil electron energy. The line that joins the two points of the interaction in the two detectors, defines the cone axis and the cone apex is at the scattering point in the front

detector (Solomon and Ott 1988) as shown in Figure 3. The point source will be imaged as the intersection of all cones from many gamma-ray interactions which can be ellipses, parabolas, or hyperbolas.

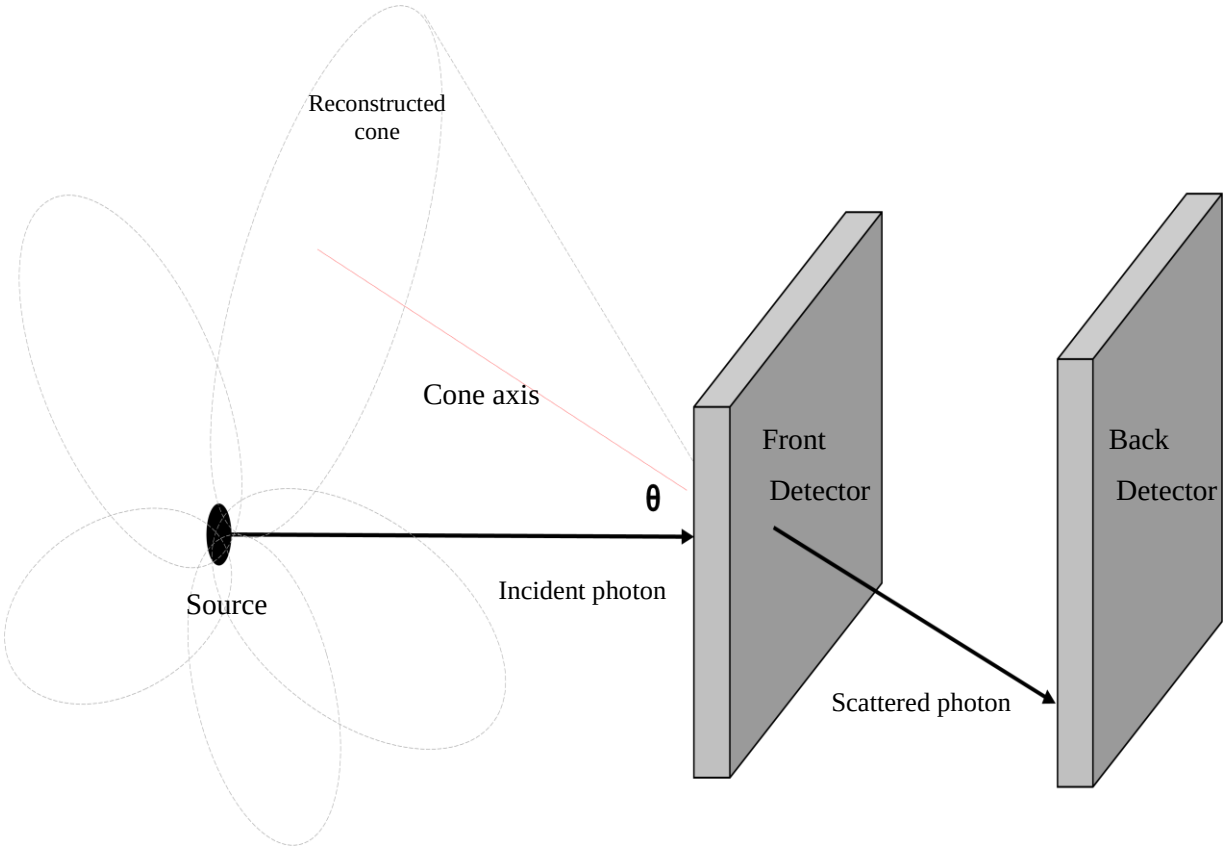

Figure 3: The principle of Compton camera imaging.

The tracking of the original direction of the emitted photons depends strongly on the accuracy of determining the parameters of the conic surfaces. Therefore, the energy resolution of the front detector and position resolution of both detectors play a crucial role in locating the point source and in eventually determining the image quality (Manbir Singh 1983, Solomon and Ott 1988, Du et al 2001).

1.7.1 Compton Camera potential advantages for medical imaging

The Compton camera has been used and proposed for many applications including gamma-ray astronomy (Herzo et al 1975), industrial imaging (Martin et al 1994), security

applications (Dedek et al 2008), and medical imaging (M. Singh 1983). In this thesis the medical application of the Compton camera will be investigated.

The Compton camera offers many potential advantages for nuclear medicine application. These advantages include the increased sensitivity which results in an improved signal-to-noise ratio, shorter counting times, and reduced patient dose. In addition, the absence of heavy mechanical collimators permits the Compton camera to be designed in a compact portable setup that can be used to image high energy gamma-rays (>300 keV) with high spatial resolution and sensitivity. The principle of image reconstruction in Compton camera can be utilized to reconstruct 3D images without the need to acquire tomographic images. The following sub-sections summaries the potential advantages of Compton camera.

1.7.1.1 **Sensitivity gain**

In principle, the Compton camera provides better sensitivity than gamma camera due to the absence of the mechanical collimators and the wide field of view that results in using larger fraction of photons emitted from the source to reconstruct the image (G W Phillips 1995). The sensitivity gain with Compton camera is about 15 to 20 times better than the mechanical collimators in 140 to 511 keV energy range (Han and Clinthorne 2009). In theory, this could result in a reduction of both the administrated dose to the patient and the scanning time, thus, achieving an increase in patient comfort and minimizing the patient motion artefacts. However, practically the effect of noise in the image reconstruction process can reduce the sensitivity gain as discussed by (M. Singh et al. 1988; Bolozdynya et al. 1997). In addition, the energy dynamic range for Compton camera is very wide, in comparison with PET or SPECT, due to the absence of mechanical collimator. Thus, the Compton camera can be used for simultaneous multi-energy imaging as reported by (S. Kabuki et al 2006). Unlike gamma-camera there is no

trade-off between resolution and sensitivity, thus fulfilling the two main requirements for emission medical imaging (LeBlanc et al 1998). Compared to the Compton imaging system, a conventional gamma camera system with lead collimator imposes a trade-off between resolution and sensitivity because of the physical constraints resulting from the mechanical collimation. As the imaged γ-ray photons exceed ~250keV, the collimator septal thickness must be increased to reduce the penetration and scattering of higher energy photons in the collimator material. Because the sensitivity for a fixed hole size collimator is reduced as the square of septal thickness, resolution must be sacrificed by increasing hole size if sensitivity is to be maintained.

1.7.1.2 **Reconstruct 3D images without tomography**

The concept of image reconstruction in Compton camera allows images to be reconstructed at different depths from a single shot without tomography and without moving the patient as shown in Figure 4. Thus, 3-dimensional images can be reconstructed with a more simplified system design and setup that allow the camera to be positioned closer to the patient (Phillips 1995).

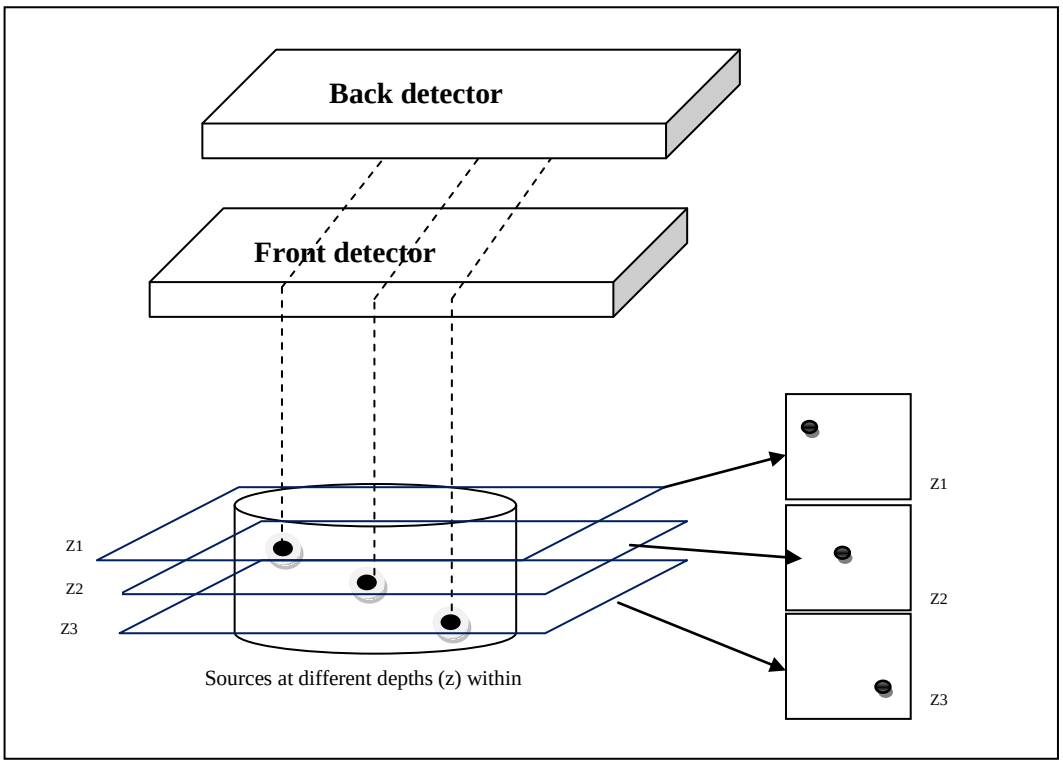

Figure 4: Principle of 3 dimensional image reconstruction of Compton camera.

1.7.1.3 **Compact and lightweight**

The absence of heave mechanical collimator potentially makes the Compton camera a more compact and lightweight system. Thus, it can be constructed as a portable mobile unit for many imaging purposes allowing the clinical investigation to be carried out in the operation theatres and variety of environments (Scannavini 2001).

1.7.1.4 **Superior performance with high energy (>300 keV)**

In principle, Compton imaging has superior performance with high energy radioisotopes compared to the mechanical collimated gamma camera. Therefore, a variety of possible high energy applications can benefit from Compton camera: including I^{131}(364 keV) imaging for thyroid glands, In^{113m} (393 keV) which can be used as a substitute for In^{111} to label blood cells to investigate infections and inflammation sites, and positron emitting isotopes(C Hua 2000). Therefore, coincidence imaging of positron emitters and single photon emitters can be carried out with the same instrument. In addition, the development

of Compton camera could facilitate the development of new physiological tracers for different diagnostic applications based on radioactive elements that have not been considered suitable currently because of their high energy radiation.

1.7.2 Factors governing Compton camera performance

The performance of any nuclear medicine imaging system is characterised by the spatial resolution and detection sensitivity for gamma ray photons. Since the tracking of the emitted photon original direction depends on the accuracy of determining the photon scatter angle then consequently defines the conic surface parameters. As mentioned by Phillips (1995) the key factors to define the expected Compton camera performance are the angular resolution and the camera efficiency as shown in Figure 5. Each factor in Figure 5 will be discussed in the following paragraphs.

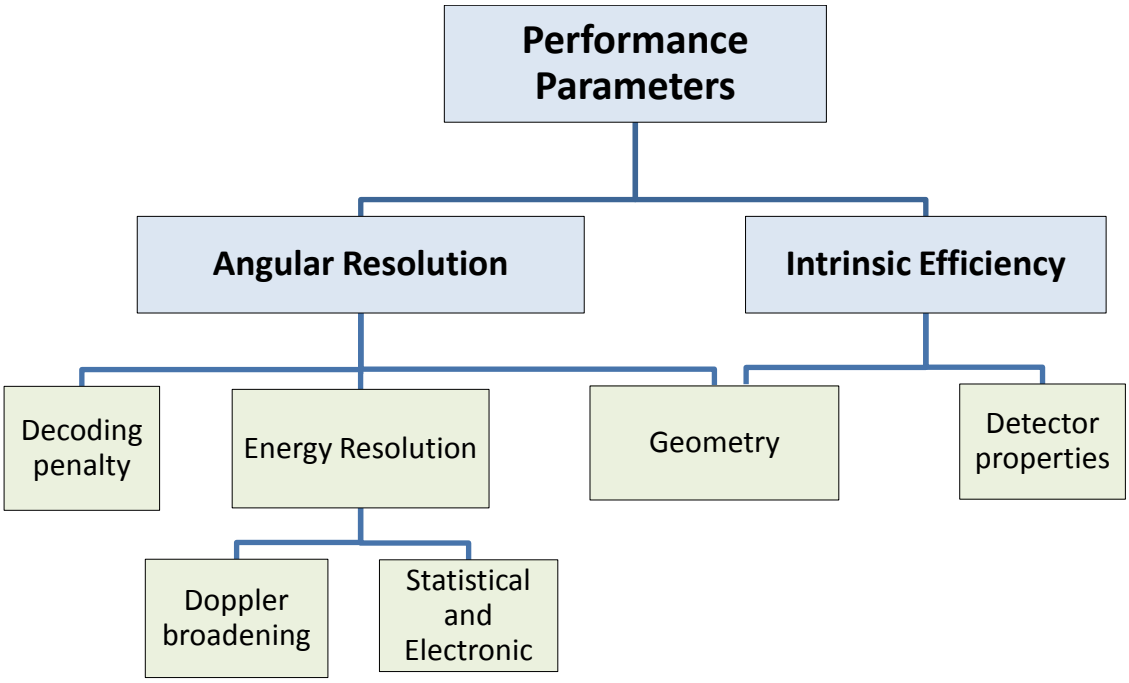

Figure 5: The key performance parameters for Compton camera

1.7.2.1 **Angular resolution**

The angular resolution is defined as the uncertainty related to the measurement of the incident direction of the incoming photons (M. Singh & Doria 1983). The energy resolution of the front detector, the position resolution of both detectors and the geometry of the detectors govern the angular resolution of the camera (Du et al 2001). The overall angular resolution can be computed from the quadratic addition of the three factors contributing to the angular uncertainty (M. Singh 1983) as seen in (2) below:

$$\tan^2(\Delta\theta_{\text{overall}}) = \tan^2(\Delta\theta_1) + \tan^2(\Delta\theta_2) + 4\tan^2(\Delta\theta_3) + \tan^2(\Delta\theta_4) \quad \textbf{(2)}$$

where $\Delta\,\boldsymbol{\theta}_1$ is the scatter detector energy resolution contribution, the $\Delta\,\boldsymbol{\theta}_{2,3}$ are the geometrical contribution, and $\Delta\,\boldsymbol{\theta}_4$ is the position resolution contribution.

Energy resolution

The response of the detector to a radiation source is characterised by a pulse height distribution which is called the detector response function. These distributions are centred on the same average value which is called the energy photopeak and reflects the source energy. The width of the photopeak reflects the amount of fluctuation in measuring the energy deposited in the detector for each event. The energy resolution of the detector is defined as the FWHM of the photopeak divided by the peak centroid (Knoll 1999). The poor energy resolution of the front detector results in large energy uncertainty and eventually affects the angular resolution of the camera and final reconstructed image. The energy resolution contribution to the angular uncertainty ($\Delta\boldsymbol{\theta}_1$) can be calculated as:

$$\Delta\theta_1 = \frac{(1 + \alpha\,(1 - cos\theta))^2}{E_\gamma\,\alpha\,sin\theta}\,\Delta E$$

(3)

where ΔE is the energy measurement uncertainty which represents the inherent statistical fluctuations in the number of charge carriers created by each interaction and the electronic noise .This can be calculated by using the (4) as the following:

$$\Delta E^2 = 2.35^2 \, FwE_{re} + (ELN)^2$$

(4)

where F is the Fano factor (0.13 for Ge), w is the ionisation energy (2.96 eV in Ge), ELN is the electronic noise, and the energy of the recoil electron E_{re} can be calculated for any given angle providing that the source energy is known.

Doppler broadening

The assumption that the incident photon interacts with a free electron at rest before being scattered is not correct. In reality the incident photon interacts with a moving electron bound to the atom and has a pre-collision finite momentum (p). Because of this momentum some of incident photon energy will be lost in the front (scatter) detector. Therefore, the effect of electron momentum will results in a broadening of the energy spectrum which leads to an additional source of energy uncertainty that is independent of the detector energy resolution. This broadening is known as Doppler broadening (Reed and Eisenberger 1972a). Doppler broadening represents an inherent limit to the Compton camera angular resolution. Therefore, (1 should be corrected to include the electron momentum (p).

The degree of Doppler broadening is calculated from the probability of Compton scatter from an electron in n^{th} shell scatter energy and angle E_A and θ respectively. The amount of Doppler broadening is given by the double differential cross section from the following expression (Ordonez et al. 1997):

$$\left(\frac{d^2\sigma}{d\Omega\, \mathrm{dE_A}}\right)_n = \frac{r_0^2\, m_o}{2E_\gamma}\left(\frac{E_c}{E_\gamma} + \frac{E_\gamma}{E_c} - \sin^2\theta\right)\frac{\mathrm{E_A}}{\sqrt{E_\gamma^2 + E_A^2 - 2E_\gamma\, E_A \cos\theta}}\; J_n(P_z)$$

(5)

where σ is the Compton cross section, E_c is the predicated scattered photon energy predicated by the Compton equation, m_oc^2 is the electron mass, r_o is the classical electron radius (r_o = 2.818 fm). In (5), the term $J_n(P_z)$ is the Compton profile which represents the pre-collision electron momentum along the scattering vector which has been compiled and tabulated for different materials by (Reed and Eisenberger 1972). The Compton profiles offer a hint of the electron movement in an atom. The Compton profiles were used in (Leblanc et al 1998) to derive the uncertainty in energy caused by Doppler broadening.

The intensity of scattered photons at any scatter energy E_A is proportional to the value of Compton profile at the corresponding (p_z) which is referred to as "electron momentum" and is given by:

$$p_z = -\mathrm{mc}\,\frac{\left(\left(\mathrm{E_\gamma - E_A}\right) - \mathrm{E_\gamma E_A}(1-\cos\theta)/\mathrm{mc^2}\right)}{\sqrt{\mathrm{E_\gamma^2 + E_A^2 - 2E_\gamma E_A}\cos\theta}}$$

(6)

where m is the electron mass (9.1 x10^{-31}kg) and c is the speed of light (3 x 10^8 m/s). P_z is usually expressed in atomic unit **a.u** (1 a.u = 1.9x10^{-24} kg m/s). The scattered photons energy spectrum can be directly calculated by evaluating (5) for each sub-shell for a specific E_A. Then, the p_z is calculated from (6) and then $J_n(P_z)$ is interpolated from the Compton profile tables available by (Reed and Eisenberger 1972). The angular uncertainty due to the effect of Doppler broadening can be calculated from the (7) (Ordonez et al 1997):

$$\sigma_\theta = \frac{1}{k_\theta}\left(k_{pz}\,\sigma_{pz}\right) \tag{7}$$

where

$$k_\theta = \left(\frac{1}{m_o c^2} - \frac{\overline{p_z}}{m_o c w}\right)\overline{E_A} E_\gamma \sin\theta \tag{8}$$

$$k_{pz} = \frac{w}{m_o c} \tag{9}$$

$$w = \sqrt{E_\gamma^2 + \bar{E}_A^2 - 2E_\gamma \bar{E}_A \cos\theta} \tag{10}$$

In (7), the term k_θ is the contribution of the energy resolution and k_{pz} is the contribution of the Doppler broadening to the angular uncertainty. The parameter σ_{pz} can be estimated by the width of the total Compton profile of the target atom and the over-bars indicate the mean values of the corresponding variables. The width parameter σ_{pz} is ≈ 1.3 a.u the Compton profile of germanium available from (Reed and Eisenberger 1972).

Statistical and electronics noise

The uncertainty in measuring the front energy (E_f) in (1 affects the system ability to estimate the scattering angle. This uncertainty can be caused by the statistical and electronics noise. The uncertainty in the number of charge carriers created by each photon interaction is known as the statistical noise (Wernick and Aarsvold 2004). This noise makes a physical limit on the energy resolution. Since the number of charge carriers, N, is proportional to the deposited energy and is described by a Poisson process, then the energy resolution is defined by:

$$E_{Res} = \frac{2.35}{\sqrt{N}}$$

(11)

However, in fact the process is not Poisson and the initial recoil electron energy is divided between electron-hole pair production and other energy loss mechanisms. The ratio of the observed variance in N to the predicted by Poisson model is known as the Fano factor. The electronics noise in the detector readout is usually expressed as the equivalent noise charge (ENC) at the input of the preamplifier. The ENC is defined as the amount of charge that would give rise to an output voltage equal to the root mean square level of the output due only to noise (Knoll 1999).

Detectors geometry

The geometry of the Compton camera detectors plays an important role in determining the interaction positions and choosing the range of the scattering angles. Any change in the camera geometry will affect the position uncertainty of the camera. As explained by (M. Singh & Doria 1983) the angular uncertainty due to the geometry contribution is inversely proportional to the square of the distance between the front and back detectors. To calculate $\Delta\Theta_{2,3,\text{and } 4}$ which represents the effect of geometry and position resolution on the overall angular resolution in (2) the following formulas (M. Singh 1983) are used:

$$\boldsymbol{S}\tan(\boldsymbol{\theta} + \Delta\boldsymbol{\theta_2}) = \frac{\boldsymbol{d}}{\boldsymbol{2}} + \boldsymbol{S}\tan(\boldsymbol{\theta} + \boldsymbol{\Phi})$$

(12)

$$\boldsymbol{S}\tan(\boldsymbol{\theta} + \Delta\boldsymbol{\theta_3}) = \left(\boldsymbol{S} + \frac{\boldsymbol{L}}{\boldsymbol{2}}\right)\tan\boldsymbol{\theta}$$

(13)

$$\boldsymbol{S}\tan(\boldsymbol{\theta} + \Delta\boldsymbol{\theta_4}) = \boldsymbol{S}\tan\boldsymbol{\theta} + \boldsymbol{r}$$

(14)

where S is the separation between the detectors, d and L are the front pixel width and thickness respectively, Φ is the half angle subtended by a pixel in the front detector, and r is the FWHM position resolution of the back detector (Singh 1983). The effect of geometry on the angular resolution of the Compton camera was calculated and will be presented in (section 3.2.2.2).

Reconstruction decoding penalty

Compton cameras include computationally costly decoding (reconstruction) calculations and noise propagation during the decoding phase. The reconstruction of Compton camera images is complicated due to the lack of a physical collimator, thus, the angular resolution due to measurement errors can vary from event to event (Parra 2000). Since the interaction of the backprojected cone and the source plane is not a straight line as in SPECT, the reconstructed Compton camera image exhibits artefacts that degrades the image spatial resolution. As a result, the intensity information in the reconstructed image does not reflect accurately the source activity distribution (Du et al 2001). In addition, reconstructing distributed sources is difficult and can be ineffective due to the inherent geometrical complexity of Compton camera data image (Andreyev et al 2011). Image reconstruction of Compton camera images has to overcome many difficulties, such as the large amount of data, noise arising from both low counts recorded and imaging response.

Several approaches were proposed to develop an efficient reconstruction method for Compton cameras as discussed in section 2.3 and compensate for resolution loss. For instance, analytical approaches that can compensate for the resolution degradation and improve the spatial resolution of the reconstructed images by modelling the factors that contribute to the angular uncertainty and include it in the reconstruction task was proposed by (Hirasawa and T Tomitani 2004).

A mathematical model, based on the uniform Cramer-Rao bound, was used by (C H Hua et al 1999) to measure the information loss during the reconstruction stage. Their model showed that the decoding penalty degradation effect is significant especially with extended source distributions and with low source energy due to Doppler broadening effect.

Another approach based on statistical image reconstructions (OSEM) that includes a resolution recovery technique was proposed by Kim et al (2010). This method considered a Gaussian resolution model for the inherent angular and geometric uncertainties which were incorporated into the OSEM reconstruction algorithm. The results showed that this method improved the image spatial resolution by an order of magnitude (Kim et al 2010). However, these methods are based on simulated data and validating these results with real data is needed.

1.7.2.2 **Intrinsic efficiency**

The efficiency of any radiation detector is a combination of two factors; geometric (absolute) and intrinsic efficiency. The geometric efficiency is ratio of the number of photons emitted by the source to the number of useful signals detected in the camera. Whereas, the intrinsic efficiency of a radiation detector is defined as the fraction of the gamma rays striking the detector which results in useful signals in the detector (G F Knoll. 1999). The intrinsic Compton camera efficiency is defined as the fraction of photons entering the first detector that undergo only one Compton scattering and are then photoelectrically absorbed in the second detector (Du et al 2001) and is expressed as:

$$\varepsilon_{icc} = \frac{1}{\Omega_1}\int_{det1} v_1 \int_{det2} dv_2\, \Delta\Omega_1 \mu_c(E_o) e^{(-\mu_t(E_o)L_1)} \frac{d\sigma}{d\Omega}(\theta_{12}) \Delta\Omega_2 e^{(-\mu_t(E_1)L_{12})} \mu_p(E_1) \quad \textbf{(15)}$$

Where Ω_1 is the solid angle subtended by the front detector at the source, $\Delta\Omega_1$ is the solid angle for a differential volume element dV1 in the front detector, Ω_2 is the solid angle subtended by the back detector at the interaction position in the front detector, L1 is the attenuation length in the front detector between the source and dV1, L12 is the attenuation length between the two elements dV1 and dV2, μ_c, μ_p and μ_t are the Compton, photoelectric, and the total linear attenuation coefficients respectively, and $\frac{d\sigma}{d\Omega}$ is the *Klein-Nishina* Compton scattering angular cross-section per electron (G F Knoll. 1999).

As indicated in Figure 5 in (section 1.7.2) the intrinsic Compton camera efficiency depends on the detector geometries. The front and back detector geometries defines the solid angles Ω_1 and Ω_2 in (15).

The efficiency is determined by the energy of the photons, system geometry and detector martial. In fact, the interaction probabilities, energy deposition in both detectors, and intervals between emitted photons are random process, thus, it is very complicated to estimate the efficiency by a simple calculation. Therefore, a Monte Carlo program (EGS4) was used by Royle et al (2003) to calculate the UCL Compton camera efficiency (ε_{icc}) for a point source at 5 cm from the front detector surface and the result is presented in (section 2.9.2).

Detector properties

Many types of detectors were considered for the construction of the Compton camera like scintillators, gaseous detectors, and semiconductors. Semiconductors are the best candidate for their excellent energy resolution due to the larger number of charge carriers created by each incident radiation photon.

The choice of front and back detector material is crucial in order to achieve high detection efficiency with Compton camera. The front detector should ideally have high probability of Compton scattering, good charge transport properties and high energy resolution. In addition, the back detector is required to have high stopping power, good energy and spatial resolution. The physical characteristics of the detector p-n junction define the operational behaviour of the semiconductor. In the following sections the key detector properties will be highlighted.

a.) Single Compton efficiency

Singh (1983) determined the interaction probabilities for a Compton camera setup to find the optimum size and type of the detector material. The parameter (P_c) was derived to define the probability of a single Compton scatter event followed by an escape of the scattered photon within a pre-described solid angle. The maximum and minimum scatter angle is determined by the detector noise and geometry (M. Singh 1983). The values of P_c were computed for Ge and Si with incident different gamma energies as shown in Figure 6.

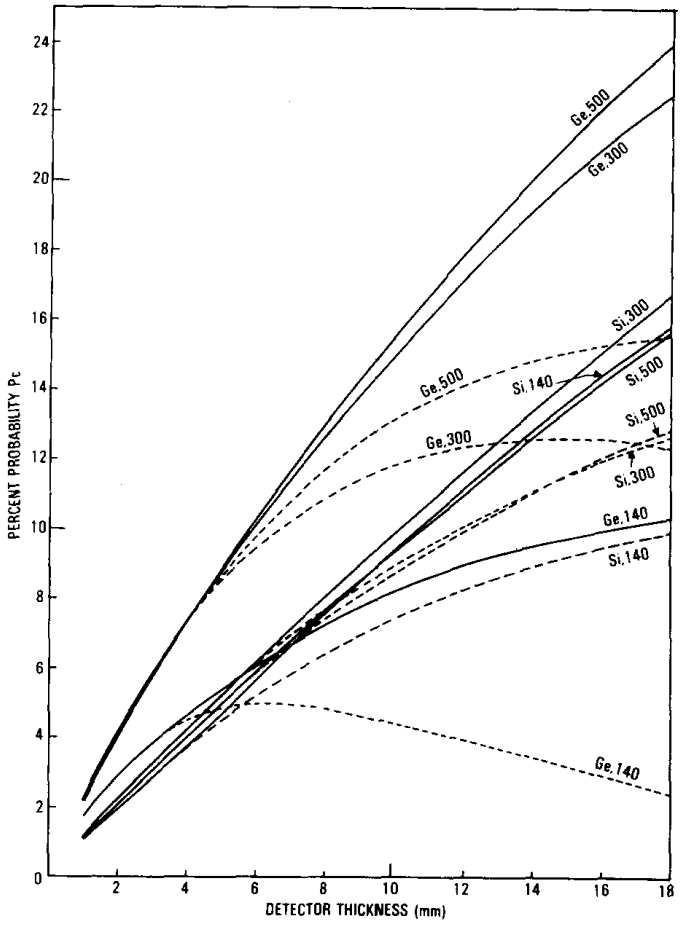

Figure 6: the probability of single photon scatter P_c for Ge and Si with different incident gamma energies (Singh 1983). the dotted lines and the solid lines represent a close-packed array and isolated detection elements respectively.

In Figure 6 the dotted lines represent a close-packed detection elements array and the solid lines represent isolated detection elements respectively. As seen in Figure 6 for the close-packed array P_c level off and then decrease above certain Ge thickness. Thus, the optimum thickness for a germanium close-packed array can be defined for the energy of interest. Moreover, Figure 6 shows that Ge has higher single Compton scatter efficiency (Pc) than silicon and the front detector thickness should be kept as thin as possible (less than 10 mm) to have an acceptable spatial resolution . Therefore, Ge is the preferred choice over Si to be used as a front detector for imaging 140 to 511 keV photon energies.

b.) Band gap and Ionisation energy

The band-gap is the energy difference between the top of the valence band and the bottom of the conduction band in the material (G F Knoll. 1999). The smaller the bandgap the lower the ionisation energy required to excite an electron-hole pair, thus leading to a better energy resolution. This is due to the fact that with smaller ionisation energy more charge carriers are produced per unit deposited energy, hence decreasing the statistical fluctuation.

c.) Leakage current

To achieve an efficient collection of charge carriers from any semiconductor a voltage is applied across the active volume to create an electric field. All detectors will show a limited conductivity (a steady-state current) even in the absence of ionizing radiation which is called a leakage current (G F Knoll 1999). Random fluctuations in the leakage current will obscure any small signal current following an ionizing event and this represents a significant source of noise and thus affecting the energy resolution and system efficiency.

Thermal generation of electron-hole pairs within the depletion region is a source of leakage current which can be reduced by cooling the detector. Some detectors have a low thermally generated current like silicon and can be operated at room temperature, but germanium detectors must always operate at reduced temperature due to their low bandgap energy as shown in Table 3 in page39. Therefore, monitoring the change in the leakage current is important and any change or increase indicates a change in detector efficiency that will effect the energy resolution.

d.) Charge collection properties

The preamplifier represents an interface between the detector and the signal processing electronics. The charge carried by an incoming pulse is integrated on a capacitor and then

removed by a low discharge, hence, the pulse is produced with a fast leading edge (rise time) that corresponds to the charge collection time in the detector followed by slow exponential decay as shown in Figure 7 . The interval between the times at which the pulse reaches 10% and 90% of its final amplitude is called the pulse rise time (G F Knoll 1999). The detector contribution to this rise time is defined by the charge transit time which corresponds to the migration time of the electrons and holes across the region of high electric field in the depletion region. Therefore, the rise time of the output pulse is limited by the time required for a complete migration of these charges from their point of formation to the opposite extremes of the depletion region. Eventually, the time resolution obtained from Ge detectors strongly depends on the average rise time and the variation of pulse shape from event to event (Knoll 1999). The time resolution will be further discussed in section (3.2.6.1).

The rise time for a complete charge collection relies on the interaction depth in the detector and the drift velocities of the charge carriers in the detector medium and can be calculated using the following formulas (Knoll 1999, J Gabathuse 2006) :

$$t_e = \frac{Z_0}{V_e} \tag{16}$$

$$t_h = \frac{d - Z_o}{V_h} \tag{17}$$

Where t_e and t_h are the electron and hole rise time respectively, d is the detector thickness, Z_o is the interaction position (from the anode), V_e and V_h are the electron and hole drift velocities respectively. The order of magnitude rise time (T_r) of germanium detectors at liquid Nitrogen temperature is given by (18) (Giauque et al 1973):

$$T_r \approx W \times 10^{-8} \text{ s} \quad \textbf{(18)}$$

where W is the thickness of the depletion region (~ detector thickness of planar detector) measured in millimetre (mm). For the front detector in the UCL prototype camera the active thickness of the detector is 4 mm, thus, the theoretically expected rise time (T_r) is 40 ns. Note that the theoretical rise time calculations do not take into account the effect of trapping and de-trapping of charge carriers on the pulse shape which leads to an increase the observed rise time.

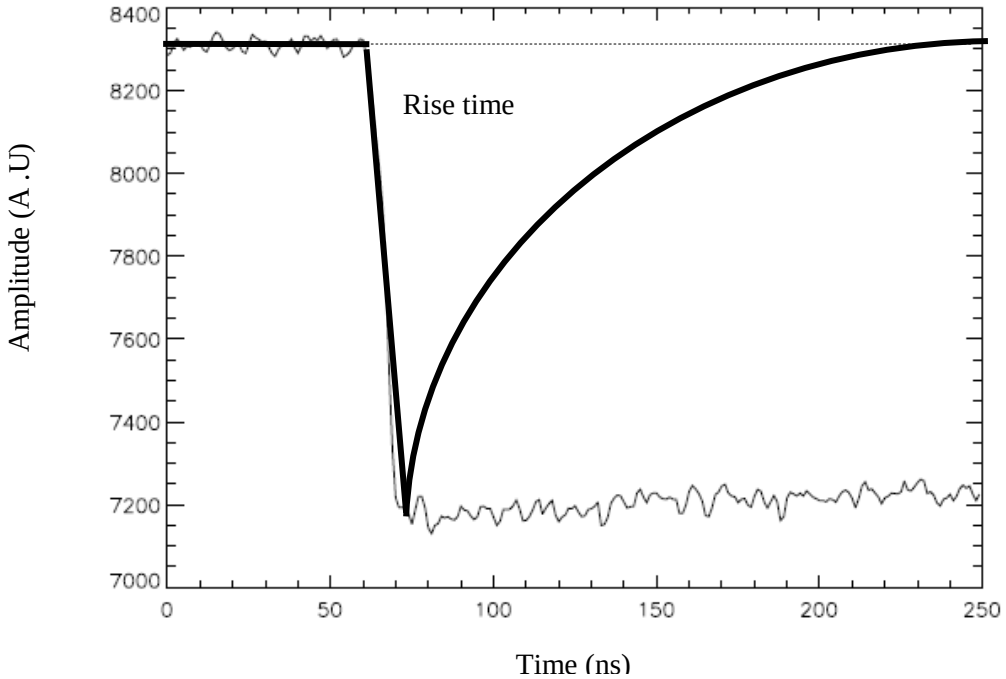

Figure 7: Example of a preamplifier output trace fed to an oscilloscope along with a sketch of a fast leading edge and a slow exponantial tail.

The motion of the electrons and holes formed when the incident photon deposits energy in a semiconductor detector constitutes a current that will continue until those carriers are completely collected. Thus, the resulting pulse represents a measure of the energy deposited by the photon. Table 3 shows the electron and hole mobility for different semiconductors. Note that the Ge detector has a greater charge carrier mobility than other

detectors that determines its superior energy and timing resolution. Table 3 summaries the physical properties of semiconductor materials.

Material	Si	Ge	CZT	HgI_2	CdTe
Atomic number (Z)	14	32	48/30/52	80/53	48/52
Bandgap energy [eV] @300 K	1.12	0.67	1.6	2.13	1.52
Ionisation energy [eV] @300 K	3.6	2.95*	4.6	4.2	4.43
Electron mobility [cm^2/Vs] @300 K	1400	3900	1000	100	800-1100
Hole mobility [cm^2/Vs] @300 K	480	1900	50-80	4.0	60-90
Energy resolution @ 122 keV	0.45%	0.32%	2.3%	2.8%	2.6%

Table 3: Physical properties of semiconductors of importance in selecting front detector materials.*value at 77 K temperature (Knoll 1999, Scannavini et al 2000, Dedek et al 2008).

The most suitable material for Compton camera system is required to have room temperature operation, high single Compton efficiency, small bandgap (low ionisation energy), good charge transport properties, and excellent energy resolution. In addition the use of high Z material to detect high energy photons minimises the degradation effect of Doppler broadening on the camera angular resolution (M Scannavini 2001).

From Table 3 and Figure 6, Ge followed by Si are the most suitable materials for the construction of Compton camera to image high energy gamma radiation due to their high Compton efficiency, good charge transport properties, and excellent energy resolution. However, Ge has higher Compton efficiency than Si for gamma energy above 300 keV

and the fabrication of silicon with small thickness less than 5 mm is difficult and requires stacking of detectors, hence increasing the cost and complexity of the system. On the other hand, fabrication of Ge detectors with up to 10mm thickness is simple (Singh 1983). The cooling requirement for germanium detectors is a limitation and the use of cryostats increase the camera size. The cost of germanium and silicon increases linearly with the detector thickness.

A room temperature operated CZT detector could be used for the Compton camera, but the low energy resolution degrades the angular resolution of the Compton camera (Dedek et al 2008). Also, the CdTe and HgI2 room temperature operated semiconductors are not suitable for the construction of Compton camera due to their poor energy resolution, low Compton efficiency and poor charge collection properties as shown in Table 3. In this thesis our studies are based upon germanium detectors as the front and back detectors as will be explained in chapter 2. In the following section the recent and most motivating contributions in the design and experimental development of the Compton camera for medical applications will be reviewed.

e.) Effect of scattering materials

The absorption or scattering of the photons emitted by the source as they pass through the object is known as the attenuation. Uncorrected attenuation results in underestimated activity due to the reduced number of detected photons, and hence, reduces the system sensitivity (Zaidi and Koral 2004). In emission tomography, the majority of attenuated photons are likely to be scatter-corrupting photons. Therefore, an energy window is usually used for the sole purpose of minimising the number of detected scattered photons. Since Compton imaging system (similar to PET) operates at a quite large energy window to maintain the system sensitivity, it is difficult to separate scatter primary photons (Saha

2010). The scatter fraction increases with increasing the energy window width. Using a narrow energy window width is possible with the excellent germanium energy resolution but at the expense of sensitivity (Floyd et al 1988). More details about the energy window settings will be discussed in section 2.2.3.

The detection probability for a given event is obtained by simply multiplying the detected photon intensity by the photons survival probability (I_o/I) which is ratio of transmission intensity before (I_o) and after attenuation (I) using (19) (Rahmim and Zaidi 2008):

$$I_o/_I = e^{-\mu x} \tag{19}$$

where μ is the attenuation along the attenuation medium of thickness x. Methods for determining the transmission data in SPECT and PET are discussed in (section 1.4). The interaction probabilities of incident photons with the detectors can be calculated from the XCOM photon cross-section library available from Berger et al (1990). Reconstructing SPECT, PET, and Compton camera images without attenuation correction can result in reducing the count density and introduces image artefacts (Zaidi and B Hasegawa 2003). Therefore, applying attenuation correction for Compton camera data similar to those used in SPECT which is described in Zaidi and Hasegawa (2003) to compensate for the attenuation effect is required for accurate quantitative measurement.

1.7.3 Development of Compton camera for medical imaging

The first experimental prototype of a Compton camera for medical use was designed in the early eighties by Singh (1983). Since then, the rapid advance in the detector technology has increased the interest in the development of the Compton camera for medical imaging. Many studies have been carried out to develop Compton camera systems however the actual clinical application of the camera has not yet been fully addressed.

The focus in recent Compton camera research is mainly on the optimisation of the Compton camera by studying the performance of different detector materials, setup, and geometry as well as the development of appropriate image reconstruction algorithm (Wernick and Aarsvold 2004). More effort is needed to experimentally study the usefulness of Compton camera for nuclear medicine applications in which it can provide an enhanced performance compared to other imaging modalities.

In the following section the recent and most motivating contributions in the design and experimental development of the Compton camera for medical applications will be reviewed. These contributions will be categorised by the type of the detector material used .i.e. semiconductors, gaseous, and scintillation detectors. The following sections describe the most significant contributions made in the last three decades to this field.

1.7.3.1 **Semiconductors**

a) Ge detectors

In 1983, Singh replaced the gamma camera mechanical collimator with a single 6x6 mm germanium (Ge) element which served as the front (scatter) detector of Compton camera using the NaI crystals of the gamma camera as the back (absorption) detector. Images of Tc^{99m}(140 keV) and Cs^{137}(662 keV) sources were obtained with spatial resolution of approximately 7 and 5 mm respectively. The sensitivity of the experiment was lower than theoretically expected sensitivity due to the presence of dead layers on the surface of the germanium detector used for the measurement, the low absorption efficiency of the NaI crystal with high photon energy and the effect of Doppler broadening with low photon energy. The camera design was improved in 1985 by using a 4x4 high purity germanium detector array which was segmented into 16 independent 5x5x6 mm elements. Each element was interfaced with its own circuitry to achieve better position capability. After that in 1990, three-dimensional images of a cylindrical phantom filled with Tc^{99m} were acquired and compared to gamma camera SPECT data acquired with the same phantom (Manbir Singh & R. R. Brechner 1990). The spatial resolution of the images obtained with electronic collimation showed no improvement compared to SPECT images mainly due to the design and detector arrangement. The pioneer work presented by Singh in the concept of the Compton camera medical imaging forms the basic theory and inspiration behind all current camera developments work.

At Liverpool University, a position sensitive high purity germanium HPGe Compton camera system was developed and evaluated (Cooper et al 2007, Boston et al 2007). Their system was named (SmartPET) as it was meant initially to be used for small animals imaging. The total active volume of the detector is 60 x 60 x 20 mm. The minimum detectable gamma energy is 244 keV due to the thickness of the front detector (20 mm).

The spatial resolution achieved for 511 keV and 1408 keV emitting sources placed at 5 cm is 7.7 and 6.3 mm respectively. The spatial resolution of the system at 511 keV is lower than PET as shown in Table 2. An improvement in the spatial resolution by a factor of 2 has is expected by implementing a pulse shape analysis (PSA) technique (Cooper et al 2007). However, the limitation of the current design and geometry necessities the need to optimize the system to improve the imaging performance and provide a competitive gamma ray detection system to current small animal PET. The reported camera efficiency is $4x10^{-2}$ at 662 keV (Harkness et al 2009).

Recently, a hybrid Compton camera and coded mask system was developed and evaluated for radioisotope (RI) labelled molecular probes (Takeda et al 2010). PET allows the tracking of only one RI-labelled probe, however, their hybrid system is able to image and track multiple probes, hence, providing better diagnosis. The spatial resolution achieved at 3.5 cm from the camera for 834 keV emitting gamma source is 3.2 mm. However, the efficiency of the Compton camera decreases with the thickness of the mask, thus, optimisation of the mask thickness is needed to enhance the spatial resolution while preserving the efficiency. Also, it is difficult to precisely calibrate the interaction position in the encoded image detector and hence, the position resolution of the front detector needs to improve to be 1 mm. The task of image reconstruction is more complex in the hybrid system.

At UCL university, a pixellated Ge Compton camera was developed to image high energy (>300 keV) gamma ray emissions in nuclear medicine examinations (G J Royle et al 2003). The system design and geometry is explained in detail in chapter 2 and the imaging performance is discussed in chapter 3.

b) Si detectors

Many other researchers used Silicon (Si) as front detectors for its room temperature operation, low cost, wide availability. An interesting study for the feasibility of Compton camera imaging (Compton cameraI) to reconstruct the dose delivered to the patient during radiotherapy was carried out by (Mundy and Herman 2010). An analytical model used Si and Ge double sided strip detectors in planar configuration to study the spatial and dosimetric resolution. The results showed that Compton cameraI is capable of reconstructing dose distribution with a 5mm spatial resolution and 5% dose resolution. Many technical challenges need to be addressed before implementing such a system clinically. For instance, with the high photon energies used in radiotherapy the probability of photon interaction with the back absorbing detector is very low .i.e. most photons will be transmitted without interaction or may be scattered outside the detector volume. Thus, large detector or multilayer detectors are needed. Another challenge is the image reconstruction because many photons will be incident on the detector per second (about $4x10^5$ photons per second), and it takes 1.5 s to back project the cone associated with one events on a 3.0 GHz processor. At this rate it will take one week to reconstruct one backprojection image. Thus, a fast reliable reconstruction algorithm is needed for this application.

Watanabe et al (2005) developed a Compton camera that consisted of six layered double-sided Si Strip detectors and CdTe pixel detectors. The energy resolution was 9.1 keV (2.5%) and 14 keV (2.7%) at 356 keV and 511 keV, respectively. Improvements in CdTe detectors to achieve better energy resolution are needed. Images for different radioisotope energies (122 to 662 keV) were obtained and reconstructed using a backprojection algorithm. The images were distorted by the backprojection artefacts due to the asymmetric arrangement of the CdTe absorbers used. Thus, having a symmetric CdTe

absorbers arrangement is required. The angular resolution was 3.9° (FWHM) for 511 keV gamma-ray photons.

At Michigan University, a prototype Compton camera (C-SPRINT) designed with a single pad Si detector surrounded by a SPRINT scintillation ring intended for low energy gamma-ray imaging for nuclear medicine applications was developed by Leblanc et al (1998). The SPRINT scintillation ring is a SPECT imaging system made up of eleven modules arranged in a 50 cm diameter ring shape with its lead collimators removed. Employing ring geometry improved spatial resolution and reduce single count rates in the second detector. Simulations results show angular uncertainties of 4.1° and 2.2° FWHM for Tc^{99m} and I^{131} point sources, respectively. The results showed that the C-SPRINT sensitivity is 2.7 $x10^{-3}$ at 140 keV which is lower than the mechanically-collimated gamma camera. Thus, it is necessary to improve the design by stacking arrays of silicon pad detectors in conjunction with an optimized second detector cylinder with **a** ring radius reduced to 12.5 cm. The C-SPRINT system had approximately equal performance for I^{131} compared to gamma camera, and could exceed the sensitivity with an optimized design. The overall position uncertainty for an I^{131} point source at 10 cm was 4.1 mm.

Ten years later, Han et al (2008) compared theoretically the imaging performance of a planar Si (scatter detector) and NaI (absorption detector) Compton camera with a HEGP collimator gamma camera using a statistical model. A cylindrical hot spot disk with 0.6 cm, 0.8 cm, 1.0 cm, 1.5 cm, 2.0 cm and 2.4 cm diameter spots was simulated with I^{131} emitted photons. The results show that if the same number of events is used the imaging performance of the Compton system is better than the gamma camera for hot spots width below~1.1 cm, this advantage decrease for spot size above 1.1 cm. The result shows that the effect of Doppler broadening is the limiting factor for Compton camera performance for imaging 364.4 keV photons. Also, the results show that the detection sensitivity of the

Compton imaging system is about 15–20 times higher than that of the collimated gamma camera. This work needs an experimental validation and a detailed quantitative analysis to confirm the statistical model results.

Takeda et al (2009) developed a new Compton camera design which employed a Si scatter detector and Cadmium Telluride (CdTe) absorption detector. Images for a point and extended I^{131} source distributions have been acquired with 18 mm spatial resolution at 15 cm. The normalized efficiency is 40% for 356 keV and 30% for 511 keV. An extended "C" shape source with 3mm gap has been imaged and reconstructed. This prototype needs further improvements in terms of efficiency which decreases as the source energy increases due to the thickness of both detectors (500 μm). This indicates that it is very difficult to image high photons energies (>500 keV) with the current system configuration because the probability of interaction is very low .i.e. photons will be transmitted without interaction.

Another approach using a Si detector was carried out by Lee et al 2008 and Seo et al 2010 They used a Monte Carlo simulation toolkit to design their system which is composed of a double sided silicon strip detector (5x5x0.15 cm^3) as the front detector and a segmented Ge detector (5x5x2 cm^3) as the back detector. The simulated spatial resolution of this system is 17, 16, and 15 mm for I^{131},F^{18}, and Cs^{137} respectively. The authors claimed that the poor imaging resolution of this system is due to the poor interaction position localisation in the absorber detector. Thus, implementing a PSA technique to improve the position accuracy is needed. In addition, the simulation does not take the effect of the image reconstruction algorithm on the image resolution into account. Also, the time resolution of a 2 cm thick germanium detector proposed for this setup is expected to be poor due to the long theoretical rise time (~ 200 ns). This approach needs further improvement in the detector configuration and setup to achieve better imaging

performance especially at 356 keV to be comparable to the conventional gamma camera performance.

c) CZT detectors

Cadmium Zinc Telluride (CZT) which is a compound semiconductor detector was proposed by many authors to be used for Compton camera imaging. The advantages of CZT are the room temperature operation and low cost compared to Ge detectors. A Compton camera prototype based on two 3-D position sensitive CZT detectors has been proposed by Du et al 2001. The simulation results showed that 2° and 3° angular resolution can be achieved for 1 and 0.5 MeV energy respectively. Moreover, the intrinsic efficiency estimated for a 500 keV emitting point source placed at 10 cm distance would be $1.5x10^{-4}$. Again, the simulation does not take account of the effect of image the reconstruction algorithm used on the resolution and verifying the simulation experimentally is needed.

A Compton camera based on the use of CZT sensors was presented by Dedek et al 2008. The camera was designed with 98 SPEAR (Single Point Extended Area Radiation) sensors which were arranged in two arrays as front and back detectors. The sensor has 5x5x5 mm CZT crystals which are encased in low attenuating aluminium housing. The energy resolution of the sensors is 3% at 662 keV. Images of a simulating Cs^{137} point source were reconstructed using a back projection algorithm. The simulated results showed that angular resolution better than 10º is achievable taking the effect of the reconstruction into account. However, the energy resolution of CZT detectors is the main limitation compared to of Ge (0.7% at 662 keV) detectors, hence the performacne of Compton imager rely mainly on the energy resolution of the scatter detector. For that reason many others have suggested using CZT as an absorption detector (Du et al 2001, Harkness et al 2009).

1.7.3.2 **Gaseous detectors**

a.) Proportional gas chamber

Kabuki et al (2006), from Kyoto university (Japan), developed a new design of Compton camera based on micro-time projection chamber (μ-TPC) filled with 90% Argon and 10% Ethane as scatter detector and GSO scintillators as absorption detector. Their system was named Electron Tracking Compton Camera (ETCC) because it makes use of the information given by tracking the direction of the recoil electron and the absorption point of the scattered photon to reconstruct the gamma ray direction event by event. The front detector is made of a 10x10x10 cm^3 Time Projection Chamber (TPC) as scatter detector and 15x15 cm^2 GSO scintillator array as an absorber.

A simultaneous image of a rat injected with I^{131} and FDG was presented (S Kabuki et al 2009). The author admits that the efficiency of this system is low due to the low gas density. In addition, the energy resolution of this system is 19% at 356 keV which is lower than other types of detectors used in Compton camera. The spatial resolution of this system is 23 mm which is lower than the conventional gamma camera. Even when the GSO absorber detector was replaced with LaBr3, the operation gain of the TPC raised the spatial resolution to 17 mm which is still not comparable to SPECT (Kabuki et al 2010a, Kabuki et al 2010b). The detection efficiency of the gaseous chamber is low and hence the long imaging time (19 hours) needed to collect the events.

Despite the poor spatial and energy resolution of the ETCC system various kinds of images for distributed sources were obtained. A thyroid gland phantom filled with I^{131} was imaged successfully and reconstructed by Kabuki et al (2006). Also, they imaged two sources with different energies at different depths in a simultaneous observation. Their results confirmed the ability of Compton camera system to image multiple sources at different depths from a single acquisition. Furthermore, the concentration of F^{18}-FDG wa

monitored and imaged in a living rat. The F^{18} concentrated initially in the shoulder bone and heart and then moved to the bladder. However, the authors have not presented any quantitative analysis of the images compared to PET. Work is needed to improve the spatial and energy resolution of the ETCC system.

Other types of gaseous detectors e.g. argon and xenon have also been considered to be used for Compton camera due to mainly the good spatial resolution and large field of view. However, the reduced energy resolution of gases detectors compared to other detector like germanium is the main disadvantage (Bolozdynya et al. 1997).

Table 4 presents the performance characteristics of the most interesting designs of medical Compton imaging camera categorized by the type of detector materials used. The system imaging performances in terms of energy, angular, and position resolution as well as the detection efficiency are summarised. To date, in accordance with the data reported in the literature it is noticeable that current Compton camera systems have suboptimal performance compared to that required for a potential clinical system. This is due to the limited resources used which characterised mainly by crude coincidence evaluation methods, slow readout electronics, inefficient reconstruction algorithms and the small detector active area size. Efforts are underway to overcome these issues as will be discussed in section 4.3.

Research group	Year	Detector materials	Energy resolution	Angular resolution	Efficiency	Position resolution
Ge detectors						
University of Southern California	1983	HPGe/NaI(Tl)	HPGe = 1.7 % NaI=10 % at 140 keV	11.5º at 662 keV	2.6 x10^{-3} at 140 keV	-
UCL university	2004-2011	HPGe	2% at 122 keV 0.8% at 662 keV	2.8º at 662 keV	3.1 x10^{-5} at 662 keV	2 mm (x-y-z)
University of Liverpool	2007	HPGe	2% at 122 keV	6.0º at 1.4 MeV	4 x10^{-2} at 662 keV	1mm(x-y-z)
RIKEN centre of Molecular imaging Japan	2010	HPGe / coded aperture	-	5.2º at 843 keV	-	1mm(x-y-z)
Si detectors						
University of Michigan	1998-2008	Si/NaI(Tl)	Si = 1 % at 140 keV NaI=9 % at 140 keV	4.1º at 140 keV 2.2º at 360 keV	2.7 x10^{-3} at 140 keV	4 mm (x-y-z)
Japan Aerospace Exploration Agency, Japan	2005	Si/CdTe	2.7% at 511 keV	3.9º at 511 keV	1 x10^{-2} at 360 keV	-
Hanyang university	2010	Si/NaI(Tl)	Si = 1 % at 140 keV NaI=8 % at 140 keV	8.6º at 511 keV	4.1 x10^{-8} at 511 keV	3mm(x-y) 5mm(z)
CZT detectors						
University of Michigan	2001	CZT	1.7% at 662 keV	3º at 511 keV	1.5x10^{-4} at 511 keV	1mm(x-y) 0.5mm(z)
UCL university	2007	CZT	3% at 662 keV	3.7º at 662 keV	-	-
Gaseous detectors						
Kyoto university	2006-2009	TPG /GSO (ETCC)	TPG= 15.4 % GSO= 8% at 662 keV	7º at 662 keV	1x10^{-5} at 360 keV	6 mm (x-y-z)
	2010	TPG/LaBr3(ce)	TPG= 15.4 % LaBr3(ce)= 3% at 662 keV	4.2º at 662 keV	-	-

Table 4: The performance characteristics of the most interesting designs of medical Compton imaging camera.

1.8 Structure of Thesis

The following information is divided into three chapters: materials and methods, results and discussions, and conclusions and future works. The materials and methods chapter describes the UCL Compton camera design and the associated controlling readout electronics as well as the operational mode, data filtering, and image reconstruction principles

The results and discussions chapter describes the physical and imaging performance of the camera followed by a detailed quantitative analysis of the results. Moreover, the images obtained with the Compton camera are compared to other systems used in nuclear medicine (gamma camera and PET).

Finally, the conclusions and further work chapter will indicate the theoretical and practical implication of the work presented in this thesis and the contribution that this work presents to the field along with the limitations of this work and how can it be overcome and optimized with future research.

1.9 Novel Work Undertaken

- A Multiple views technique was used to image the source from different angles and simulate the pixel arrangement in the full camera.
- A Cylindrical Perspex phantom was designed and imaged with F^{18} and I^{131} for the first time with the UCL Compton camera.
- The UCL Compton camera phantom images were compared to gamma camera and PET images quantitatively for the first time.

Chapter 2

2 Materials and Methods

2.1 Camera geometrical design description

The camera is a prototype for medical application built at the ORTEC detector R&D plant at Oak Ridge Tennessee, and it consists of two planes of pixilated HPGe detectors in the same vacuum housing. The front (scatter) detector pixels are clustered in 8 arrays distributed around a ring. The front detector is a solid disc of germanium which has a diameter of 100 mm and a thickness of 4 mm, but only the outer region is active. The total number of pixels in the front detector is 152.

The back (absorption) detector consists of one 5 x 5 pixel group and has a diameter of 28 mm and thickness of 10 mm. The pixels are 4x4 mm^2 and are spaced by 1 mm. The front and back detector are separated by 9.7 cm as shown in Figure 8. The pixellated outer ring has a 10 cm width. The front detector plane is positioned towards the front of the outer surface of the cryostat as shown in Figure 8. A circular indentation has been made in the end cap to position a lead disc to shield the back detector from direct interaction as will be discussed in section 3.1.2.

Germanium detectors cannot operate at room temperature due to the small bandgap and the large thermally induced leakage current that would result. The camera is cooled to about 200°C (77° K) by liquid Nitrogen to reduce the leakage current noise and prevent it from spoiling the excellent energy resolution of germanium (G F Knoll. 1999). The liquid

Nitrogen Dewar, which has 12 liters volume, is kept in thermal contact with the detector. The Dewar holding time is 48 hours. The liquid Nitrogen Dewar is mounted vertically on the cryostat as shown in Figure 8. Between the liquid Nitrogen Dewar and the Aluminium (Al) end cap, a larger hexagonal (Al) housing can be seen in Figure 8 which houses the preamplifiers. Outputs for each detector and power supply inputs are located on the sides of this housing.

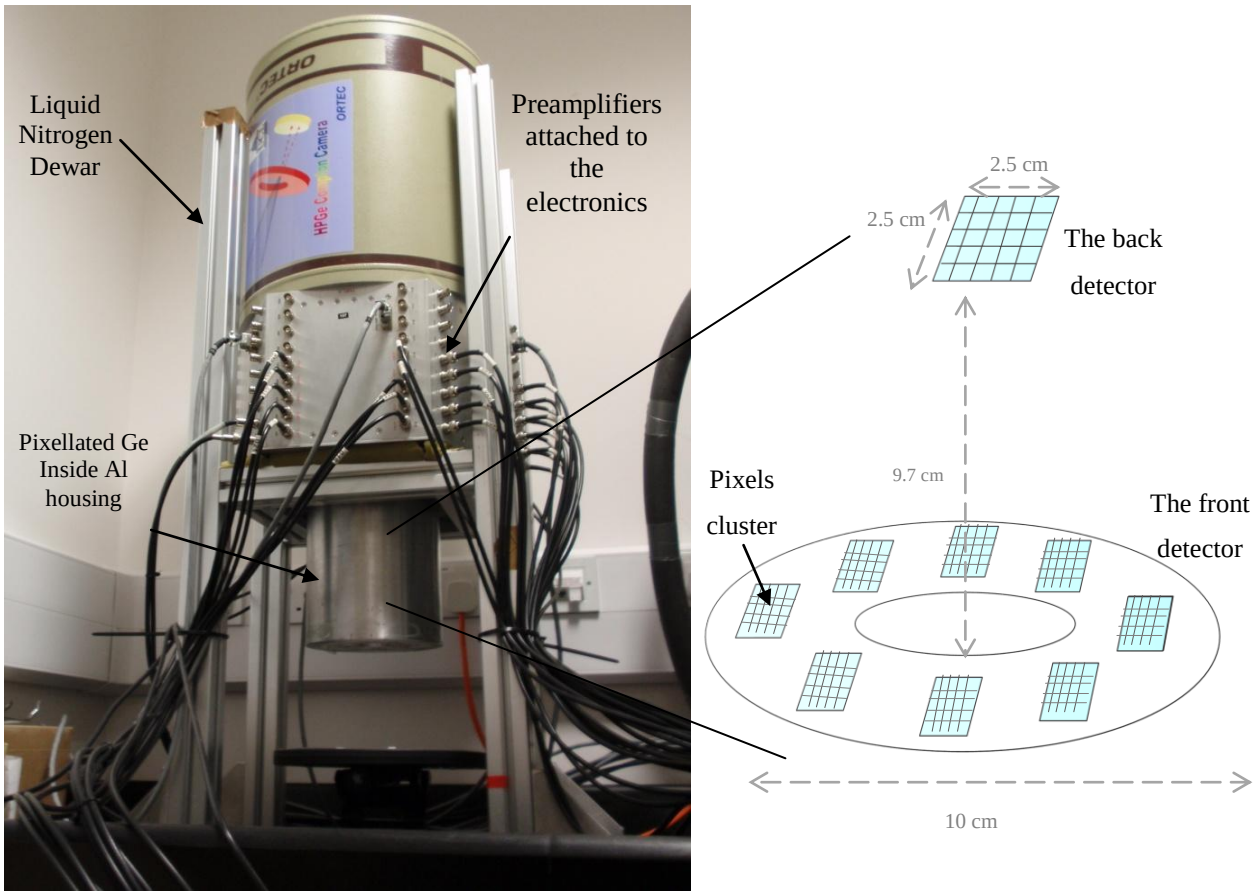

Figure 8: A photograph of the UCL pixellated Ge Compton camera along with a description of its detector geometry.

A cross-sectional view of the camera is shown in Figure 9. The front and back germanium detectors are encapsulated by Copper (Cu). The copper practically eliminates the lead x-rays resulting from photoelectric interactions of gamma rays with the surrounding

materials (ORTEC 2011). In addition, due to the high energy of the gamma rays employed very thin aluminum end window (0.013 mm) is located in front of the crystals to minimize attenuation of gamma ray before entering the germanium. Aluminium is used and preferred for its robustness.

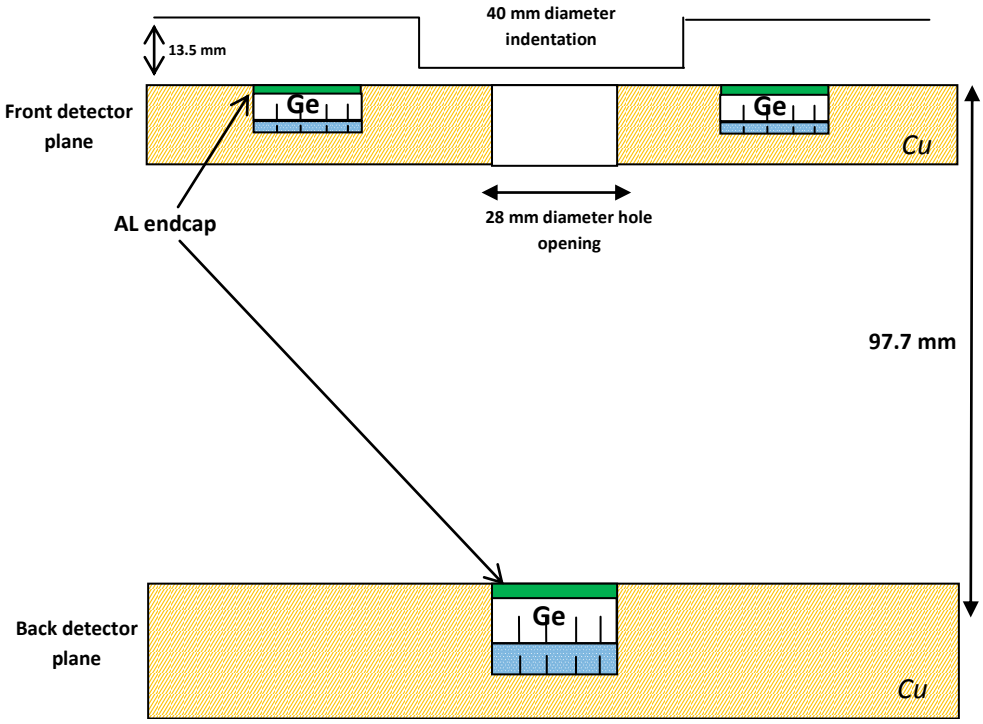

Figure 9: Cross-section of the camera highlighting the precise diameter and components of the camera.

The purpose of the geometrical arrangement of the front detector is to provide a stereoscopic view of a small source distribution in front of the camera (Royle et al 2004). This will maximise depth resolution in the image. The camera geometry of a large ring scatter detector backed by a smaller cylindrical absorbing detector was designed to select a preferred range of scatter angles. Differentiating the Compton equation with the scatter angle indicate that maximum energy deposition per unit angle occurs within angular

range of 20° and 80° as shown in Figure 10. Thus, at these scatter angles the measurement of the scattered photon energy will be more accurate and is limited by the detector energy resolution (Royle et al 2004).

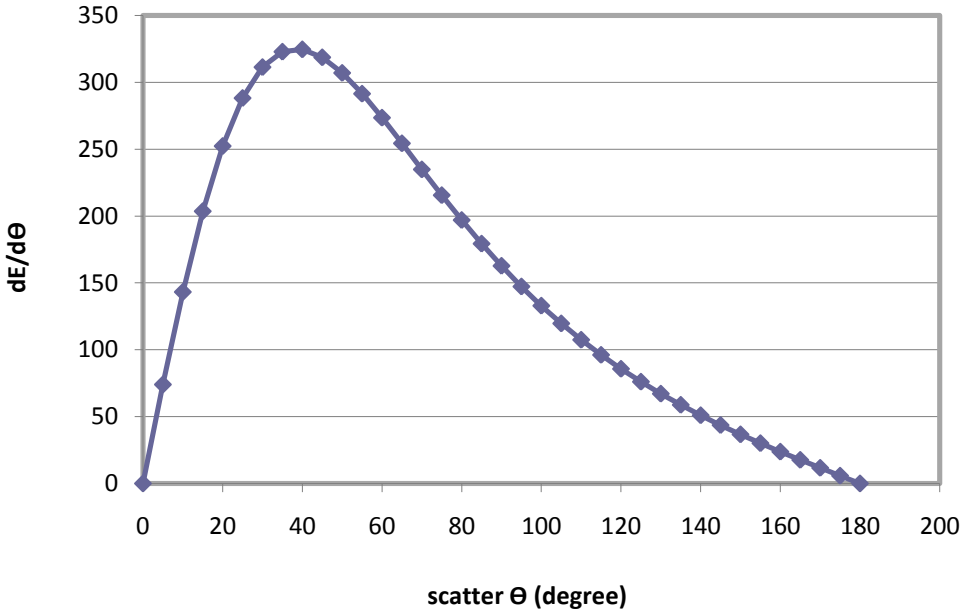

Figure 10*:* preferred Compton scatter angles at 662 keV

2.2 The controlling readout electronics

The GRT4 card (Gamma-Ray Tracking 4 channel) was designed and built by the nuclear physics group at Daresbury laboratory in the UK (I H Lazarus et al 2004) for the UK Gamma-Ray Tracking and Digital Pulse Processing project, a joint research project between the CCLRC2 Daresbury Laboratory (DL), University of Liverpool and University of Surrey. The GRT4, shown in Figure 11 (b), is a VME module featuring four acquisition channels operating in parallel. Each GRT4 card has four channels operating in parallel each with an analogue signal input, amplifier, 40 MHz low pass filter, ADC

(14bit, 80MHz flash ADC), and two Xilinx Spartan field programmable gate arrays (FPGA) as shown in Figure 11. The VME board includes three Sub-Miniature version A (SMA) connectors that are used for NIM logic signals as shown in Figure 11 (a). The connector labeled *Trigger In* can be used to feed an external trigger signal into the GRT4 and the trigger logic can be configured to listen to the external trigger instead of the internal trigger. The connector labeled *Trigger Out* can be used if a coincidence between different detectors is required. It can also be programmed to function as a Busy Out. Together with the *Gate In* connector one can assure a common start and stop if the setup consists of multiple GRT4 modules (Lazarus et al 2004).

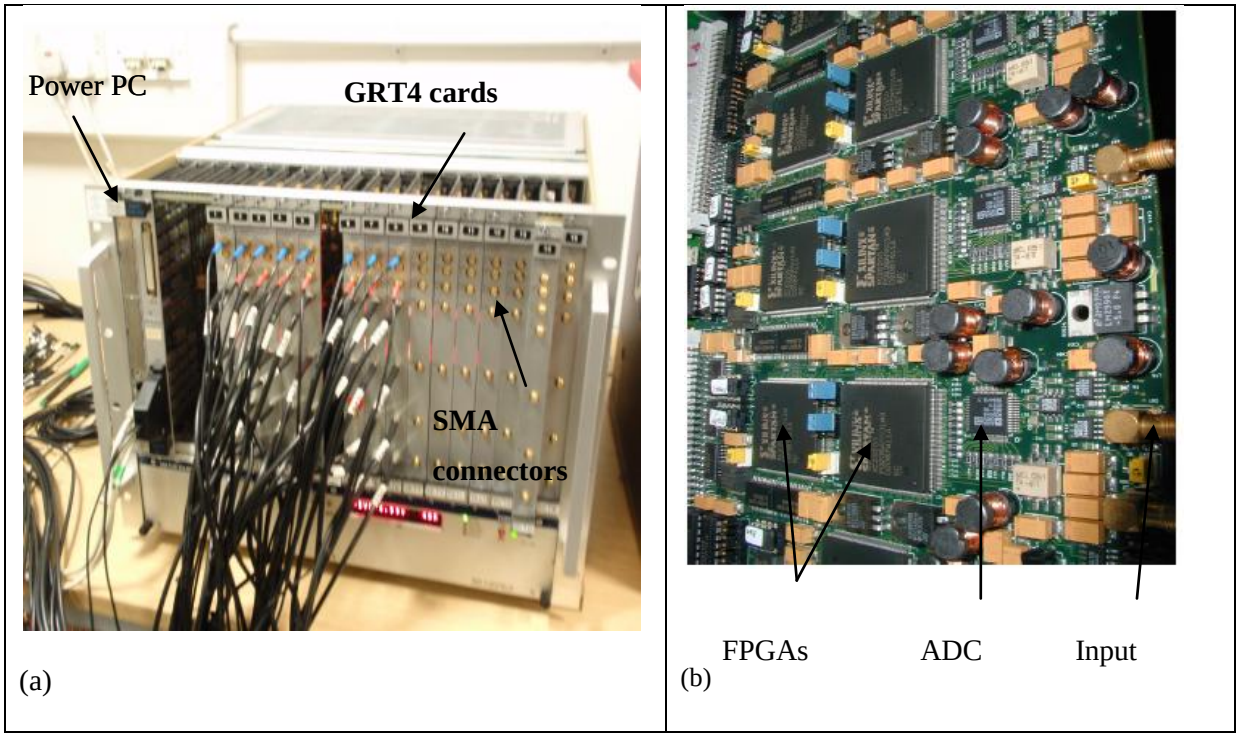

Figure 11*: A photograph of the GRT4 readout electronics (a), the outline of one GRT4 card VME module (b)*

The first FPGA contains a circular buffer with a programmable pre-trigger register delay, an algorithm for digital self triggering and timing information, and a moving window de-convolution (MWD) energy discrimination algorithm see p.61 for a description of use (Georgiev et al 1994). The second FPGA is provided for online data processing.

Moreover, a VME PowerPC (PPC) card is used as an interface between GRT4 readout electronics and the PC used for data acquisition control. This provides a route of intercommunication between pixels and allows the GRT4 cards to communicate with each other. Ethernet protocol is used to send the data to the PC for offline processing. The controlling readout electronic components of the camera are shown in Figure 12. The UCL camera readout electronics contain the following parts: GRT4 (Gamma Ray Tracking 4 Channel) VME cards, Emerson MVME5500 PowerPC, XVME260 relay card, Philips 740 gate/delay generator, logic fan in/out control, High voltage (HV) power supply, and a Linux PC as shown in Figure 12. The acquisition software used is called MIDAS (Multi Instance Data Acquisition System) which was developed by Pucknell (2004) to controls the readout electronics and data acquisition.

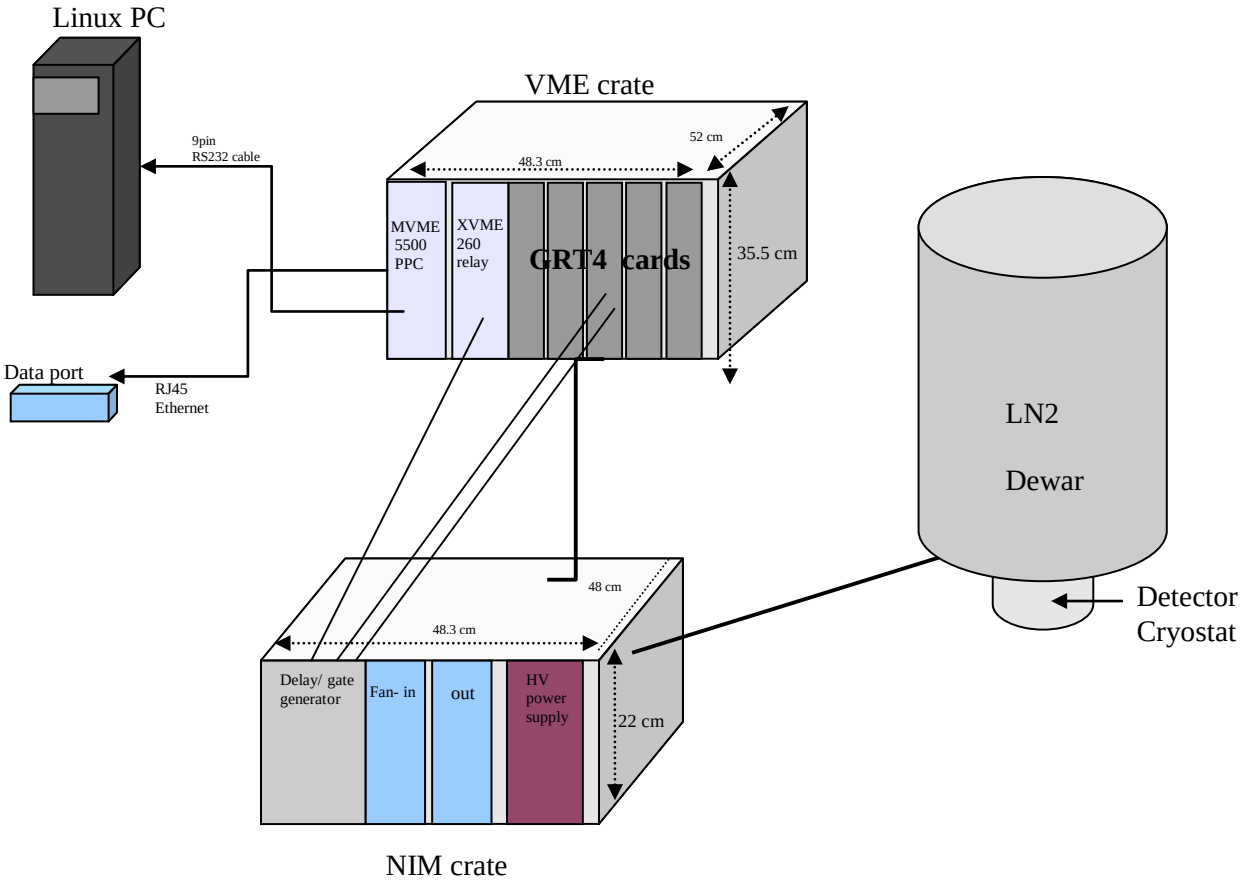

Figure 12*: the UCL Compton camera and GRT readout electronics components*

When a gamma-ray interacts with the detector medium a cloud of charge carriers will be generated as demonstrated in Figure 13. The cloud will then drifts to the sensing electrodes under the influence of an applied bias voltage of -500 V. Then, a signal (trace) will be recorded in the pixel where the interaction took a place and sent to the readout electronics. This signal is digitised using the analogue to digital convertor (ADC) allowing pulse shape to be stored for offline analysis. For each gamma ray interaction a trace of 250 samples, corresponding to 3.1 μs is recorded from each channel.

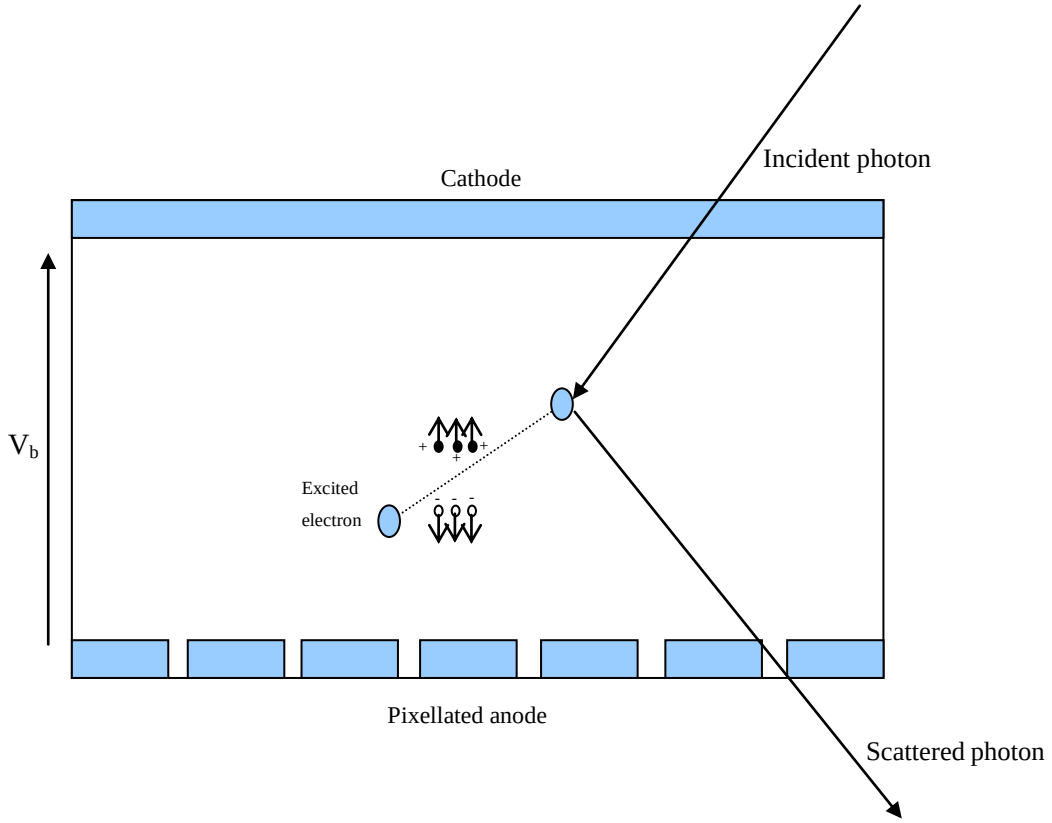

Figure 13: The principle of operation for the pixellated Ge Compton camera

The GRT4 allows the implementation of an external analog Constant Fraction Discriminator (CFD) to generate a common trigger signal from the central contact and put this signal onto the Trigger inputs of all the GRT4 modules needed to read out this detector. More details about the trigger control and the energy extraction will be discussed in the following sections.

2.2.1 Moving window deconvolution (MWD) energy extraction

The capability of extracting accurate energy information from the digitized pulse shape is very important for Compton imaging. The energy of each pulse is determined by using the MWD algorithm for signal processing. The energy is digitally extracted from the digitized preamplifier signals by measuring their amplitude which is proportional to the collected charge.

The MWD algorithm transforms the signal from a preamplifier (featuring an exponential decaying signal) into a signal which would be obtained from a transistor reset amplifier (featuring a stair case signal), before a moving average operation removes high frequency noise from the signal and at the same time generates the trapezoidal signal shape, as shown in Figure 14, which provide information about the deposit energy from its amplitude (Georgiev et al 1994).

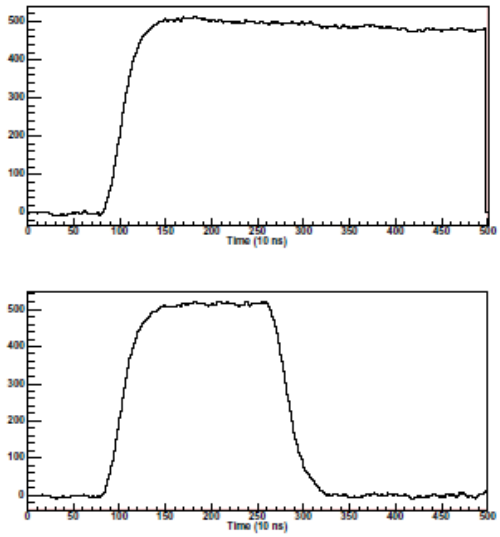

Figure 14: The original signal measured from a preamplifier (top) and the deconvoluted signal trapezoid shape (bottom) following the application of MWD routine. The total charge deposited by the photon interaction is calculated as the average value between the start and the end of the flat top of the deconvoluted pulse (Descovich 2002).

The MWD parameters are set in the MIDAS acquisition control software based on the required filtering. These parameters are: the pulse shaping time, peaking time, peak separation and peak sample time. The parameters were measured by looking at preamplifier pulses with an oscilloscope and analyzing them. An example of the pulse parameters is shown in Figure 15 and the typical MWD setting parameters provided by the GRT4 developer (Lazarus et al 2004) are summarized in Table 5.

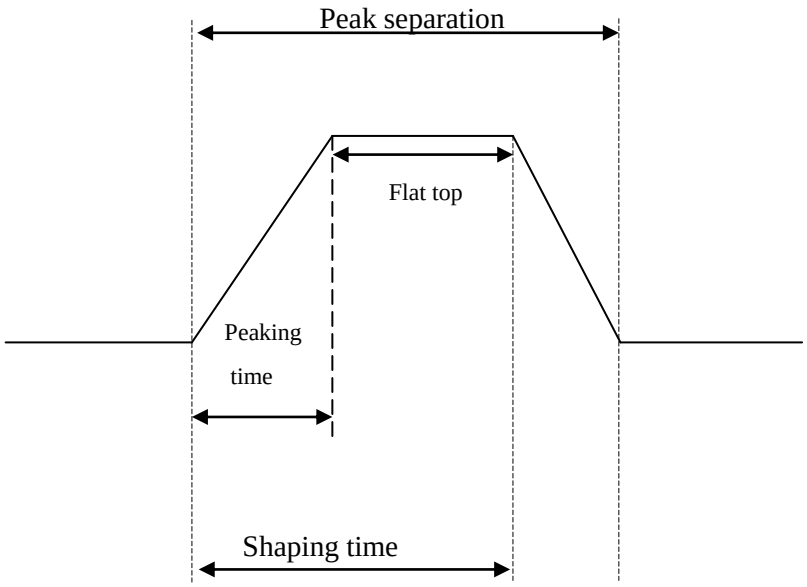

Figure 15: Sketch of the MWD algorithm pulse parameters

MWD parameter	Setting value
Clock frequency (fixed)	80 MHz
Shaping time	8 μsec
Peaking time	6 μsec
Peak separation	14 μsec

Table 5: The MWD algorithm setting parameters used with the GRT4 readout electronics.

The peaking time is an indicator of the rise time. The shaping time, which equals the rise time plus the peak flat top, reflects the trapezoid (deconvolution) width. The trapezoid flat

top value reflects the total charge (energy) deposited by the gamma-ray interaction. The peak separation is set to the sum of the shaping and two peaking times. Further details will be presented in section 3.2.1 about the effect of the trapezoid window width on the energy resolution.

2.2.2 Triggering and flow control

Discriminators generate precise logic pulses in response to input signals exceeding a given threshold. There are two key types of discriminators: the leading edge discriminator and the constant fraction discriminator (CFD). The leading edge discriminator produces an output pulse at the time when the input pulse crosses a given threshold voltage. The CFD is used as an internal trigger for each GRT channel to generate a logic pulse whose leading edge indicates the timing information for input signals above constant fraction of the peak pulse amplitude (Knoll 1999). The digital CFD can be described by the following formula (Crespi et al 2010):

$$S_{out_{ti}} = S_{in_{[ti-d]}} - F\, S_{in_{[ti]}} \qquad \textbf{(20)}$$

where S_{in} is the input signal, S_{out} is the output signal, t_i is the sampling time (=12.5ns), F is fixed fraction value (=0.5) and d is the shaping delay time (=50 ns). The only programmable parameter is the CFD threshold set (discriminator level). The CFD will trigger (produce an output pulse) only if the voltage of the input from the detector preamplifier crosses the threshold set. The best leading edge timing characteristics are obtained when the timing discriminator is set to about 10 to 20 % of the pulse amplitude (Knoll 1999). A detailed investigation of the effect of the CFD discriminator level on the reconstructed data will be described in (section 3.2.6.3).

The camera coincidence events are currently captured by the self triggered back detector that sends a trigger to the front detector. Thus, the front detector will rely on an external trigger. The back detector was chosen to trigger the front since it will see fewer events due to the small detection area compared to the front detector. In addition, the front detector will have more incident photon flux than the back detector. Following a trigger, 250 samples (3.1µs) of data will be recorded from all cards. Then, the energy and position information for each pixel is sent to the PC in list mode and stored for offline analysis and image reconstruction.

The only way to control the triggers (block/permit) and synchronies the GRT4 cards is the use of gate. The gate/delay generator (Philips NIM -794) is used to generate gate/delay periods for triggering events. In addition, the XVME260 relay card is used as an electronically operated on/off switch which is used to control the trigger input. The GRT4 output can be programmed to be either Trigger out or Inhibit/Busy. When an external trigger is in use, the Inhibit/Busy signal is used to control flow and is fanned into the inhibit signal on the gate/delay card. The diagram in Figure 16 shows the common dead time operation with external trigger and flow control.

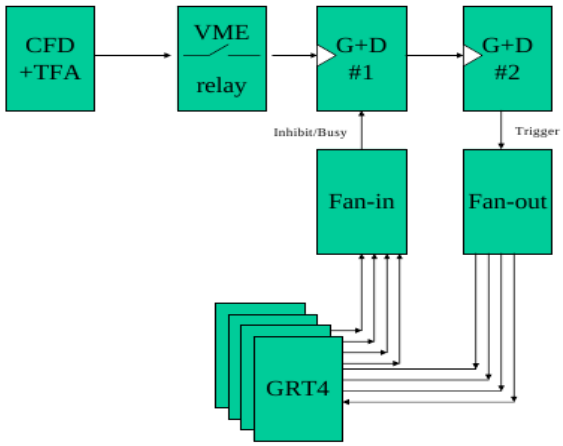

Figure 16: Common dead time operation (I H Lazarus 2006)

The system is currently being modified to collect only coincidence events from both detectors. Thus, efficient data flow will save time to exclusively collect good events. The intention is to divide the digital pulse processing between the different parts of the system and use a coincidence logic unit to control the operation. The coincidence operation between the two detectors can be controlled by a coincidence timing control logic circuit. When operating in coincidence mode the coincidence control circuit inhibits processing of single events from the back detector to reduce the system dead time.

If two timing pulses from both detectors arrive within the predefined time window, a coincidence signal will be generated to initiate data processing and readout sequence. While the detector is reading data from the temporary data storage, any new coincidence events will be inhibited until the current events is processed and the data readout sequence is initiated. Two enable signals will be generated and fed back to the GRT4 cards to process the events and send the data out. Data outputs are stored in temporary data storage, the First in First out (FIFO) buffer memory. The FPGA tells the computer to read data in if data is available in FIFO. The FPGA also sends read signals to FIFOs to release the stored data to the VME data bus. A simplified block diagram of the intended logic control circuit is shown in Figure 17.

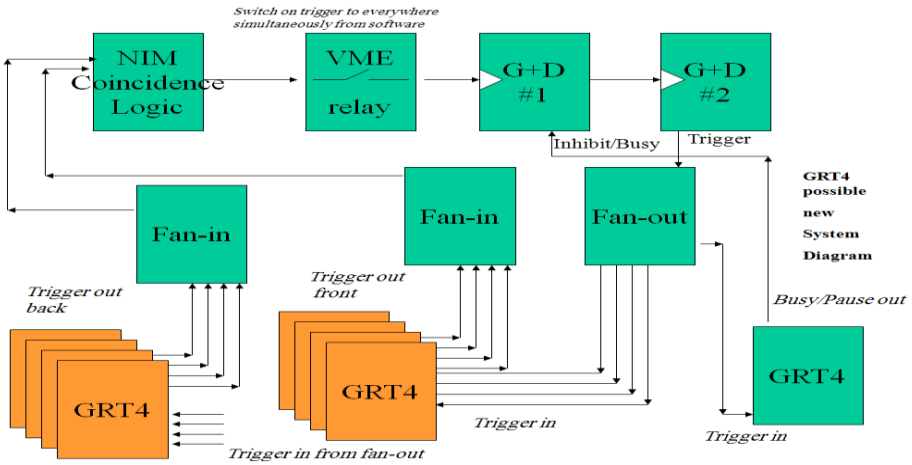

Figure 17: Block diagram of the intended improved GRT4 readout system

2.2.3 Data filtering

Currently, the camera operates in an offline data analysis mode i.e. all events will be collected from the camera and then only coincident event will be selected offline for image reconstruction. About 1 TB of data is usually collected for each image. Then an offline data filtering code is used, which is written in Interactive Data Language (IDL), to filter the data and chose only events interacting with front and back detectors within a predefined time and energy window. This reduces the data set by about 80% resulting in a 4 GB data size.

For each interaction the GRT4 electronics channel number, MWD energy, and a timestamp were all recorded in the raw data file. The data filtering code works by first removing single events which only occurs in the back detector without being scattered in the front detector. Then, the code select only coincident (useful) events that falls within 75 ns time window (more details about the time window selection will be discussed in section 3.2.6) and fulfilling the energy window condition; which is described by (21):

$$| E_f + E_b - E_{source} | < \text{energy window} \quad \textbf{(21)}$$

where E_f and E_b are the measured front and back detector energy respectively. For instance, if the energy window is set to 350 keV only events deposit total energy minus the source energy smaller than 350 keV (i.e. the total deposited energy should be less than or equal to 313 keV) will be selected as useful event. The electronics channel numbers in which the interaction was recorded will be converted into physical positions in space (pixel positions) and the energy will be extracted from measuring the height of the signal by MWD algorithm. The data is then stored in a data file which will be created for the

image reconstruction algorithm including the x, y, z, and the energy (E_{mwd}) for pixels in which the coincidence event was detected. This data file is then used as an input for the image reconstruction code which is written in C++ language.

2.3 Image reconstruction

The backprojection is the most common straightforward algorithm used in the reconstruction of the cross-sectional images data obtained from many imaging modalities (R J Ott 1986). A simple backprojection algorithm is used for straightforward image reconstruction for the data obtained from Compton camera simply by superposition of all conical surfaces resulting from each interaction (Wilderman et al 1998). Using a 3GHz Pentium processor the time taken to reconstruct 100x100 pixels image with 20000 events is 6 seconds. Back projection is a very useful reconstruction method that provides an easy to interpret image as well as providing a starting point for some iterative image reconstruction methods.

To reconstruct a 2D image a specific image plane should first be chosen. Then, the intersection of the cones with the image plane is then determined which can be an ellipse, a parabola or a hyperbola depending on the angle between the cone axis and the plane. Thus, the intensity of every image pixel is given by the number of conic sections crossing the pixel. The superposition of all conic sections is simply the back projection image (Wilderman et al 1998). The backprojection image of a point source is also called point spread function that describes the response of the imaging system. Image reconstruction is particularly challenging for Compton camera because the point spread function is not constant and varies with source position (Wilderman et al 1998, Dedek et al 2009).

For 3D image reconstruction this procedure is repeated for several image planes as shown in Figure 4. The main problem of backprojection reconstruction for Compton camera images is the introduction of image artifacts that leads to degradation in the image resolution (Martin et al 1994) as will be demonstrated in the results chapter.

Although list mode backprojection reconstruction is simple and fast, in Compton scatter imaging the intersection of the backprojected ellipses and the source plane results in image error or artifacts. These artifacts can be defined as the extra unwanted information that is artificially produced by the reconstruction algorithm that the original imaged object did not contain (Ahmed 2007). Iterative algorithms like MLEM (Maximum Likelihood Expectation Maximization) or order subset expectation maximization (OSEM) could be used to overcome these problems and result in a better estimate of the source activities and location (Parra 2000). They are however computationally intensive and their convergence points can be ambiguous (Wieczorek 2010). Possible alternative solutions could be provided using the stochastic origin ensembles (SOE) algorithm (Andreyev et al 2010). The image reconstruction decoding penalty will be discussed in section 1.7.2.1.

2.4 Imaging objects

The objects used to carry out the imaging experiments are mainly the calibration point sources either imaged statically or moved by mechanical motors to draw the required extended source shape as will be further explained in the results chapter.

2.4.1 List of sources

A sealed Cesium (Cs^{137}) calibration point source which has 2 mm diameter and 3 mm thickness was used. The activity used is 3.7 MBq. This source was used for most of the experiments carried out in this project due to its long half-life (30 years) and high gamma

ray energy (662 keV). Moreover, Barium (Ba^{133}) which have 10.5 year half-life and 356 keV (70%) gamma ray energy and sodium (Na^{22}) with 2.6 year half-life and 511,1230 keV energy calibration point sources were used for some experiments. Moreover, I^{131} and F^{18} which are widely used in nuclear medicine radioisotopes were used for some experiments. Table 6 lists the radioisotopes used in this project along with their physical properties.

Radioisotope	Half-life	Main Energy(keV)	Images
Cs^{137}	30 years	662 (85%)	Point, line, and ring source
Ba^{133}	10.5 years	81(34%) 276 (7%) 303 (18%) 356 (62%)	Point source
Na^{22}	2.6 years	511 annihilation photon 1274 (100%)	Point source
I^{131}	8 days	284 (6.05%) 364.4 (81.2%) 636 (7.26%) 723 (1.8%)	Vail and phantom
F^{18}	110 min	511 annihilation photon	phantom

Table 6: The radioisotopes used in this project along with their properties and images obtained for them. The numbers between brackets represents the percent yield per decay.

2.4.2 Achieving distributed sources

To achieve distributed sources the point source was moved into different positions using a stepper motor to draw the required shape. A 2cm line source was imaged by moving a Cs^{137} point source parallel to the camera front surface into 8 positions separated by 0.25cm to draw a line shape.

In addition, a ring shaped source was drawn by mounting a point source on a propeller attached to a motor as seen in Figure 18. The point source was attached to one end of the propeller which was rotated at 3 revolutions per minute. The point source was placed at different distances from the center of the propeller to have variable radius of rotations and draw ring source with different diameters. This concept of using a motor and propeller was proposed by (Zoglauer A. 2005).

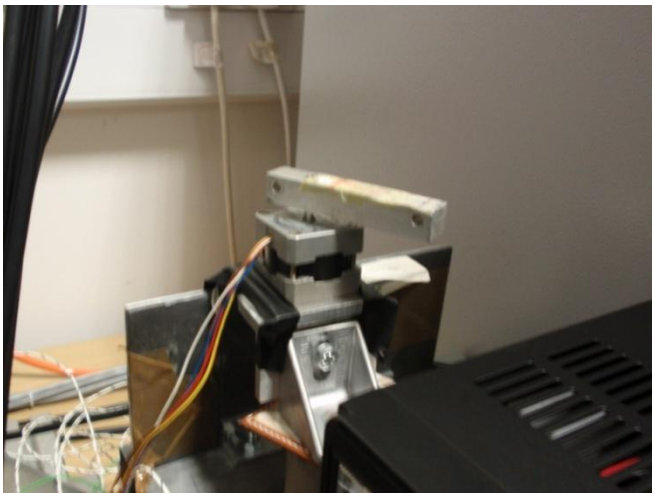

Figure 18: Propeller attached to a rotating motor

Additionally, a vial filled with I^{131} was used with a different experiment setup to test the camera performance using 360 keV source energy. The vial width and length are 20 x 40 mm respectively. The activity used was 10 MBq. The vial was positioned horizontally in air and imaged, and then it was placed in a water phantom and imaged again with the

same setup as shown in Figure 19. After that, the same vial was positioned vertically and imaged in air and water as shown in Figure 20.

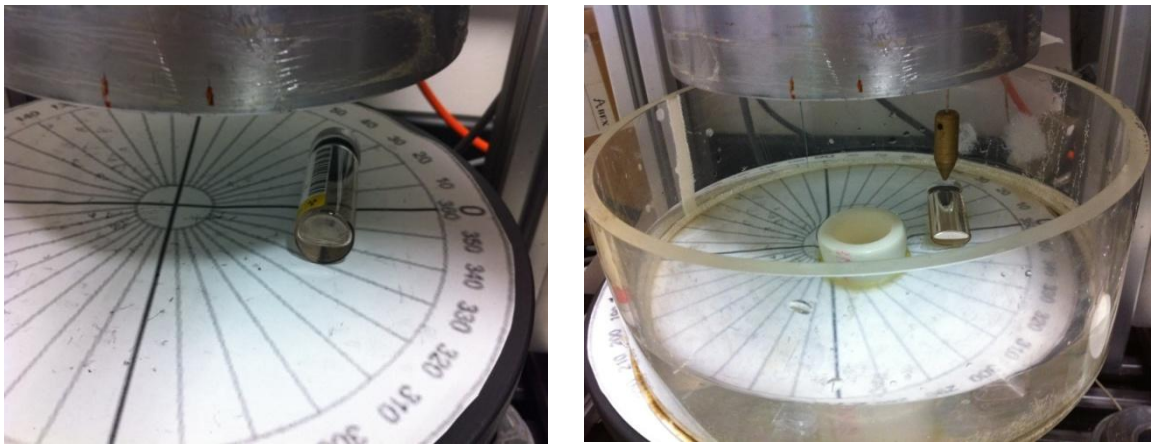

(a) (b)

Figure 19: A photograph of the horizontal I^{131} vial placed below the camera front detector (a) in water phantom (b).

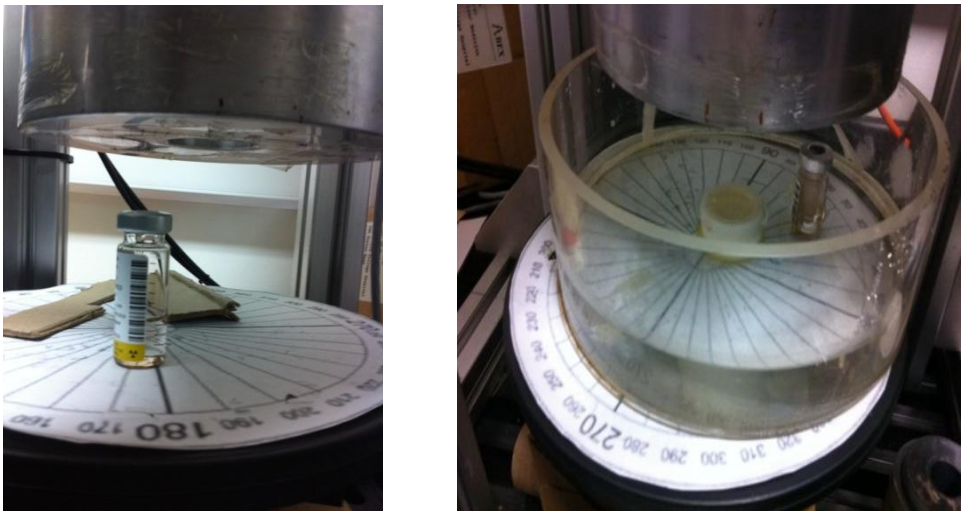

Figure 20: The experiment setup in air (left) and water (right) for the vial placed vertically.

2.4.3 Nuclear medicine phantom

A Perspex cylindrical phantom with 17 cm outer diameter and 9 cm height was designed with hollow Perspex inserts as shown in Figure 21. Perspex was chosen as a scattering material due to the fact that it has a good degree of compatibility with human tissue which mainly contains water (Liu et al 2009) as shown in Table 7. The cylinder wall thickness is 3.2 mm and the inside diameter and height are 15 and 7 cm respectively. Each insert was crafted by drilling a 9 mm diameter hole in a Perspex rod. Both the inserts and the outer cylinder can be filled with water or radioisotope concentrations. The phantom inserts can be positioned in many orientations and shapes.

Five mountable Capillary test tubes were inserted in the phantom and arranged in a triangular shape. The tubes were arranged as two triangles, one with 2cm sides and the other with 4 cm sides. Each tube was crafted by drilling a 9 mm diameter cylindrical hollow in a Perspex rod that can be filled with radioactivity. The tubes were arranged as two triangles one with 2 cm sides and the other with 4 cm sides. The radioactivity doses (F^{18} and I^{131}) were obtained from the University College London Hospital (UCLH) and transported to the Medical physics radiation laboratory for imaging. Details about the phantom transportation plan, local rules and safety procedures, and contingency plans are provided in the appendix.

Material	Effective atomic number (Z)	Density $g.cm^{-3}$	Mass attenuation coefficient* $cm^2\ g^{-1}$	linear attenuation coefficient* cm^{-1}
Water	7.4	1.0	0.085	0.085
Perspex	6.8	1.2	0.083	0.099

Table 7: Properties of water (tissue) and Perspex.* The mass and linear attenuation coefficient is at 662 keV.

Figure 21*:* Photographs of the triangles phantom design

2.4.4 Gamma camera and PET scanner specifications

A Siemens Biograph Emotion duo PET /CT (BGO) Scanner was used to acquire the phantom images and compare it to the Compton camera as demonstrated in section 3.5.1. The detector has 144 blocks each block has 64 crystals. The diameter of the detector ring is 830 mm. The camera has 24 detector rings and there are 384 detectors per ring so the total number of detectors is 9216. The transaxial FOV is 585 mm and the axial FOV is 162 mm. The PET acquisition parameters used is shown in **Table 8** . The Computed Tomography (CT) parameters were: 25 mAs, 130kV, 5mm slice thickness, 72 ms scan time, 3 ms delay time, 0.8s rotation time, and number of images is 356.

Parameter	Setting value
Acquisition Protocol	Whole Body (WB)
coincidence time window	4.5ns
Acquisition time	3 min
Acquisition mode	3D
The energy threshold	350 keV

Table 8: The PET acquisition parameters used to acquire the images.

For I^{131} imaging a High Energy General Purpose (HEGP) collimator was used with Siemens e.cam gamma camera. The Siemens e.cam camera has a 53.3 x 38.7cm field-of-view (FOV) and the NaI(Tl) crystal size is 59.1 x 44.5 cm. The camera has 59 photomultiplier tubes (PMTs). The system spatial resolution (FWHM) with HEGP collimator for a point source at 10 cm is 14.5 mm. The system sensitivity is 185 kcps/Mbq.

The triangles phantom was used with 10 MBq of activity in each tube. The main phantom container was filled with water without background activity. The uniformity and attenuation corrections were disabled. The matrix size used is 128x128 without zoom.

2.5 Multiple views setup

As mentioned earlier in (section 2.1) the front detector of the Compton camera is designed with 8 pixel clusters to have stereoscopic view for the imaged object from the reconstruction of different cone angles. Currently, some pixels from only two pixel clusters are active (16 in the Central right and 11 in the Lower central clusters as shown in

Figure 22(a). This is due to the limited number of readout electronics which will results in cones emerging from only two directions. The camera was designed and meant to be used with 8 pixel clusters i.e. having cones from 8 directions. Therefore, to obtain a glimpse of the images expected with the full camera; one solution is to obtain images from different equally spaced projection angles and then superimposing these images to bring cones from different angles into focus. The other solution is to rotate the camera to acquire images for the imaged object from different angles which is problematic due to the weight of liquid Nitrogen dewar and the large number of cables used to connect the detector pixels to the readout electronics and the power supply. This technique was used to maximize the information yield from Compton camera images and simulate the full camera (M A Alnaaimi et al 2011). The principle of acquiring Compton camera images from different angles was proposed by (Singh and Brechner 1990, Kohara et al 2008).

To acquire images from multiple views, a rotating table (platform) with 25 cm diameter was used to take image at different angles from the camera central axis as shown in Figure 22. Then, each point source position (x, y) was defined in the reconstruction algorithm relative to the camera central axis to have the right ellipse orientation in each projection. The rotating platform was aligned with the camera end cap such as the camera central axis is parallel to the platform center of rotation. The estimated position uncertainty is 2 mm that corresponds to one-half the pixel size (Singh 1983). The position uncertainty leads to an angular uncertainty of the source location and distortion in the reconstructed image (Du *et al* 2000).

In the first view the point source was placed 4.15± 0.2 cm to the right of the camera central axis below central right pixel cluster which is used as the starting angle 0°. To collect enough statistics in a reasonable time with the limited number of readout

electronics the source was placed at 3 cm from front detector. Then, the point source was moved and imaged beneath each pixel cluster i.e. 45° equally spaced positions from the starting angle as shown in Figure 22.

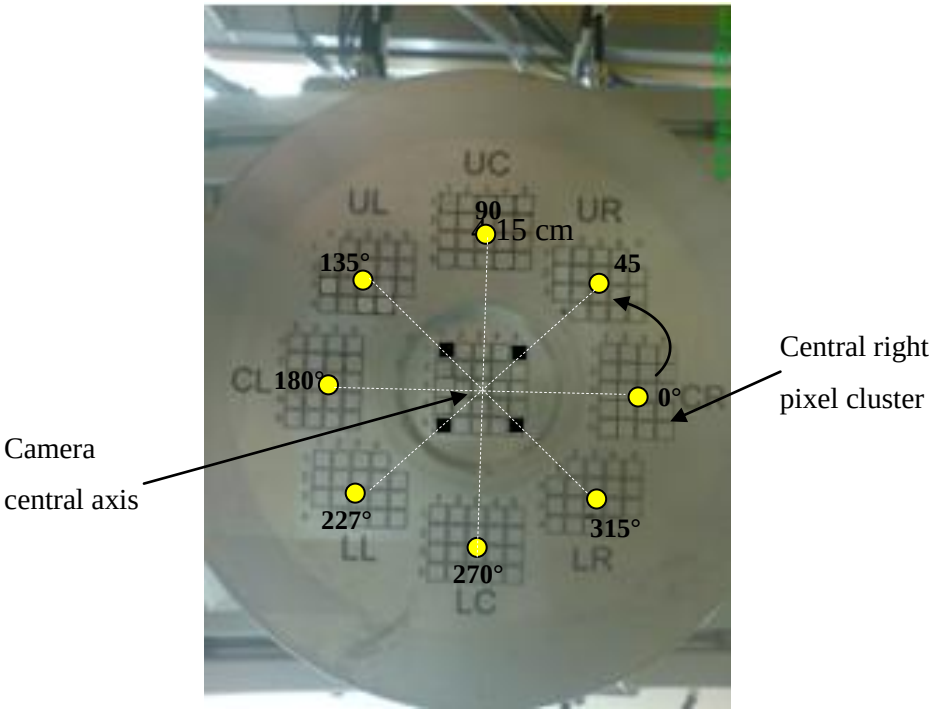

(a)

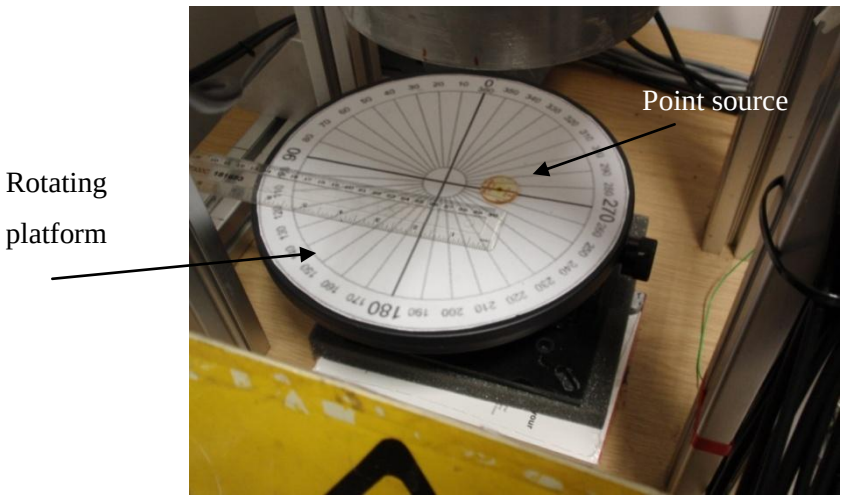

(b)

Figure 22: (a) A bottom view for the camera with a map of the front and back pixels. The point source position for the multi-view acquisition is indicated by the yellow dots (b) the rotating platform used for multiple views imaging.

2.6 Data analysis

Proper evaluation of the imaging system performance is required to have a fair comparison of Compton camera to conventional cameras. Predicting system performance accurately is critical in imaging system design. System geometry and system parameters can be optimized and determined accordingly before actual hardware implementation.

Nuclear medicine imaging systems are often described in terms of physical quantities that characterize various aspects of their performance. These quantities include measures of spatial resolution, signal to noise ratio, and contrast as described in the following paragraphs.

Point spread function (PSF)

Line profile was taken across the imaged point source and the FWHM of the profile was measured by taking the width of half the peak maximum value. In some experiment asymmetric pixels geometry was used which results in non-uniform cone shapes and directions, thus, the average PSF for the line profiles taken from different angles through the imaged source was taken. The PSF is used in chapter 3 to evaluate the spatial spread of the point source images obtained at different distances and variable source energies.

Signal to noise ratio (SNR)

The SNR was calculated within a circular region of interest ROI (1cm diameter) which was defined in the center of each image around the imaged source within which the mean was divided by standard deviation (Dahlbom et al 2005). The SNR was used to evaluate the count rate performance and the effect of noise on the point, line, ring and phantom images presented in chapter 3. It is assumed that the image noise originates from the

statistical noise in the counting data (Sorenson and Phelps 1987). The SNR increases as the total counts increase and decreases as the number of image pixels increases.

Percentage contrast

The contrast of the image which refers to the difference in intensity in parts of the image related to different concentrations of activity (Sorenson & Phelps 1987) was measured by using (22):

$$\boldsymbol{contrast} = \frac{|\boldsymbol{max} - \boldsymbol{min}|}{\boldsymbol{max} + \boldsymbol{min}} \quad \textbf{(22)}$$

Where max and min refers to the maximum and minimum pixel value. The results were multiplied by 100 to obtain the percentage contrast.

2.7 Image acquisition

To controls the readout electronics and data acquisition the MIDAS (Multi Instance Data Acquisition System) acquisition software developed by V. Pucknell (2004) was used. The GRT4 VME modules are configured, controlled and monitored by the MIDAS software. The experiment setup can be saved and used by the automatic experiment control in order to restore the hardware to its predefined state. The MWD energy determination algorithm parameters can be defined in the MIDAS software as well as the CFD and trigger values. The MIDAS software communicate with GRT4 cards via the Power PC and receives a block of data that contains the trace of each pixel which is then recorded it in a tape storage media for offline analysis.

2.8 Errors

All measurements are subject to errors which can be systematic or statistical. Systematic errors are those caused by incorrect settings and produce results that consistently differ from the correct result by some fixed amount. Random error on the other hand is the variation in the results from one measurement to another due to the physical limitation of the system or from the actual random variations of the measured quantity itself (Sorenson and Phelps 1987). The inherent measurement position and energy errors results in a miss-estimation of the cone parameters which eventually lead to a density distribution about the true location of the point of emission (Solomon and R J Ott 1988).

Some possible sources of errors in this work include: positioning, random and backprojection reconstruction errors. Positioning error is caused by the uncertainty in the exact position of the front and back pixels relative to the source position. The pixel is assumed to be within half a pixel size (± 2 mm) of its nominal position (Singh 1983). Positioning errors lead to source to detector alignment errors. The back projection algorithm is sensitive to the errors in detector and source alignment i.e. small misalignment can cause large distortion in the reconstructed image (Du *et al* 2000).

Random errors in the measurement arise from the inherent counting fluctuations due to the random nature of radioactive decay and the statistical variation of the number of charge carriers produced for an incident photon (Knoll 1999).

In addition, the intersection of the backprojected ellipses and the source plane results in image error (artifacts). This artifact can be defined as the extra unwanted information that is artificially produced by the reconstruction algorithm that the original imaged object did not contain (Ahmed 2007).

In the multiple-view setup rotation error may arise from the misalignment of the projected data due to centre of rotation errors. Poor alignment of detector central axis and the centre of rotation can result in a blurred image.

2.9 Previous Characterisations

2.9.1 Position sensitivity

The position sensitivity measures the variation of the shape of signals as a function of interaction position. The quality of the signal shapes depends on the noise level in the detector, sampling frequency and the dynamic range of the digitizer determines the position sensitivity (Descovich 2002). Previous work to study the position resolution of the UCL Compton camera was carried out by studying the induced charges to main signal neighbouring pixels as well as the rise time of different interaction depths (Ghoggali et al 2004).

Signals from radiation detectors carry information in their time, amplitude, and shape. The position sensitivity can be estimated by analysing the parameters related to the signal (trace) timing properties along with exploring the information given by the induced charges in the surrounding pixels. Pulse shape analysis (PSA) is a method that utilised digital signal processing to analyse the shape of the pulses produced and extract position information Example of neighbouring pixel induced charge is shown in Figure 23.

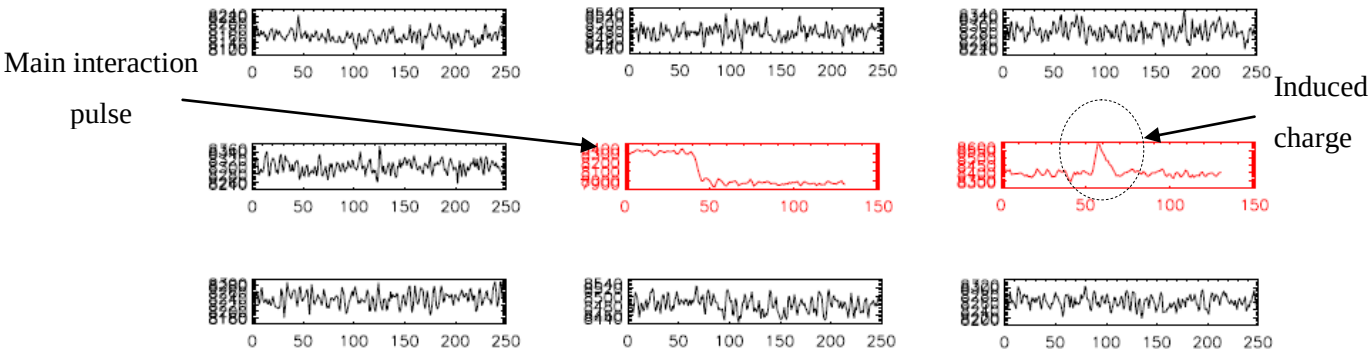

Figure 23: example of the induced charge in neighbouring pixels with positive polarity

The amplitude of the induced pulse in a neighbouring pixel depends on both the distance of the interaction from that neighbouring pixel and the depth of interaction (Vetter et al 2004). Thus, if the amplitude and polarity of the induced charge in all neighbouring pixels and the initial pulse rise time are recorded this information can be used to determine the interaction x, y, and z location. The relative amplitude of the induced pulses that is used to determine the interaction position is given by:

.

$$X = \frac{Q_r - Q_l}{Q_r + Q_l} \qquad Y = \frac{Q_t - Q_b}{Q_t + Q_b} \tag{22}$$

Where Q_r , Q_l , Q_t and Q_b represents the charges on the right, left, top and the bottom pixel respectively. For instance, if the induced charge occurred in the right of the main interaction pixel we can define the interaction position to by 1mm toward the right neighbouring pixel instead of assuming that the interaction is in the centre of the pixel.

Moreover, the polarity of the induced charges can be used to estimate the depth of the interaction. It is negative if the main interaction happens near the cathode, and positive if the interaction happens close to the anode (M Descovich 2002). Thus, by knowing the

polarity of the induced charge the depth can theoretically be estimated within ± 2 mm from the centre of the pixel. Figure 24 shows an outline of the front pixel dimension and the expected improvement in the localization of the interaction position by studying the induced charges in neighbouring pixels. The position sensitivity of the system can be defined within 2x2x2 mm^3 voxel for the front detector pixels as shown in Figure 24.

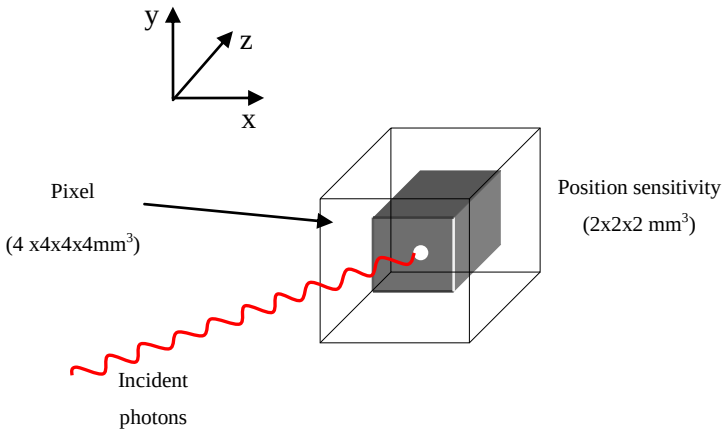

Figure 24: position sensitivity of the system can be defined within 2 mm^3 voxel

A position sensitivity of 2 mm was achieved by studying the charge induced in neighbouring pixels (Ghoggali et al 2004). The position sensitivity could improve to about 0.5 mm by measuring the rise time and the polarity of the induced charges (Descovich 2002).

2.9.2 Simulated efficiency

A Monte Carlo program (EGS4) was used to compute the UCL Compton camera detection efficiency for a point source at 5 cm from the front detector surface (Royle et al 2003). An estimation of the efficiency of the camera has been computed using (15) by considering the various interaction probabilities and solid angles for a gamma ray emitted by the source and then Compton scattered in one of the front detector pixels followed by an absorption in one of the back detector pixels.

It should be noticed that the simulated efficiency was done for the full system i.e. 152 front pixels and 25 back pixels. The Compton camera efficiency for different source energies is shown in Figure 25.

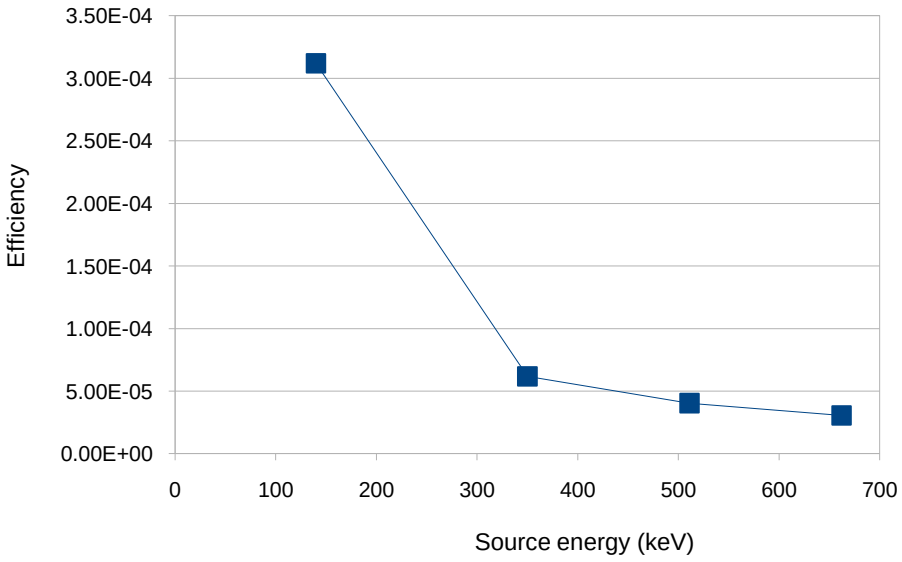

Figure 25: simulated efficiency of the UCL Compton camera for a point source at 5 cm from the front camera face (G J Royle et al 2003).

As can be seen in Figure 25 the absolute efficiency computed from Monte Carlo simulation was estimated to range from $3.6x10^{-04}$ to $3.06\ x10^{-05}$ for 140 and 662 keV respectively. The absolute efficiency of Compton camera shown in Figure 25 for the

energy range 140 to 662 keV is comparable with that of conventional SPECT gamma cameras (1.9×10^{-4} and 4.2×10^{-4}) as reported by (Madsen 2007).

The efficiency of the camera could be improved by increasing the mass of detector elements in the front detector; however this would increase the cost due to the additional readout electronics. The low UCL camera efficiency compared to the Compton camera developed by (J. B Martin et al 1993, Du et al 2001) is mainly due to the large separation between the two detectors and their geometrical arrangement. The efficiency decreases exponentially with increasing the separation between the detectors (Martin et al 1994) The back detector has smaller detection area than the front detector and subtended a small angular range, thus suffers from low efficiency. The reason of having larger front detector backed by a smaller one is to maximise the depth resolution as described in (section 2.1)

Chapter 3

3 Results and Discussions

This chapter contains a description of the system performance characteristics and imaging performance. In the beginning of this chapter the probability of interaction of incoming photons with the camera will be presented. Then, the effect of random events on the camera and how to minimise it will be described. The system performance characteristics in terms of resolution, efficiency, and counting performance are presented. The imaging performance of the UCL Compton camera with extended source distributions was evaluated. A quantitative analysis of the experimental results is given and discussed. Moreover, a multiple views technique was used to simulate the full system. The camera resolving power was measured and reported. Finally, phantom images were acquired and compared to SPECT and PET.

3.1 Probability of interaction

In Compton camera systems it is required to maximize the probability of single Compton interaction in the front detector followed by an escape and total energy deposition in the back detector (Singh 1983). This requires that the back detector subtend a large solid angle at the first detector and also the back detector need to be thick enough to stop the scattered photons. The probability of interaction of photons with the front and back detector was investigated to have more understanding for the amount for energy deposited in each detector and its relation with the source energy. With the scatter (front) detector

Table 9 shows the theoretically calculated front detector energy as a function of scatter angle (20° to 80°) for different incident photon energies. The theoretically expected front energies for a given scatter angle were derived using the Compton formula in

(1 assuming that the Compton scattering occurs with a free electrons.

Scatter angle *(theta)*	Source Energy *(keV)*				
	140	**250**	**360**	**511**	**662**
20	2.2	7.0	14.6	29.1	48.0
25	3.5	10.8	22.2	43.8	71.6
30	4.9	15.1	30.9	60.4	97.9
35	6.5	20.0	40.5	78.3	125.6
45	10.3	30.8	61.3	115.8	153.9
50	12.3	36.6	72.0	134.5	182.0
55	14.5	42.5	82.8	152.8	209.4
60	16.7	48.4	93.3	170.3	260.2
65	18.9	54.3	103.6	187.0	283.2
70	21.1	60.0	113.5	202.8	304.6
75	23.3	65.6	123.0	217.5	324.2
80	25.5	71.0	131.9	231.2	342.2

Table 9: Theoretical calculation of the front detector energy as a function of scatter angle with different source energies

The probability of single scatter in the front detector depends on the Compton to total cross section, the atomic number, and the geometrical coverage of the detector about the source to be imaged (Wernick and Aarsvold 2004). Based on the calculated front energies in Table 9 the energy threshold was set to 10 keV for all measurement (unless mentioned) to accept only gamma-ray photons scattered by > 20° in the front detector and minimize

the detector noise effect particularly for source energy > 360 keV. Any energy value below the energy threshold value will be considered as noise distribution and rejected. The detector noise determines the minimum scattering angle that can be detected. The Compton to total cross section and the Compton cross section for Si, Ge, and CZT as a function of energy are shown in Figure 26.

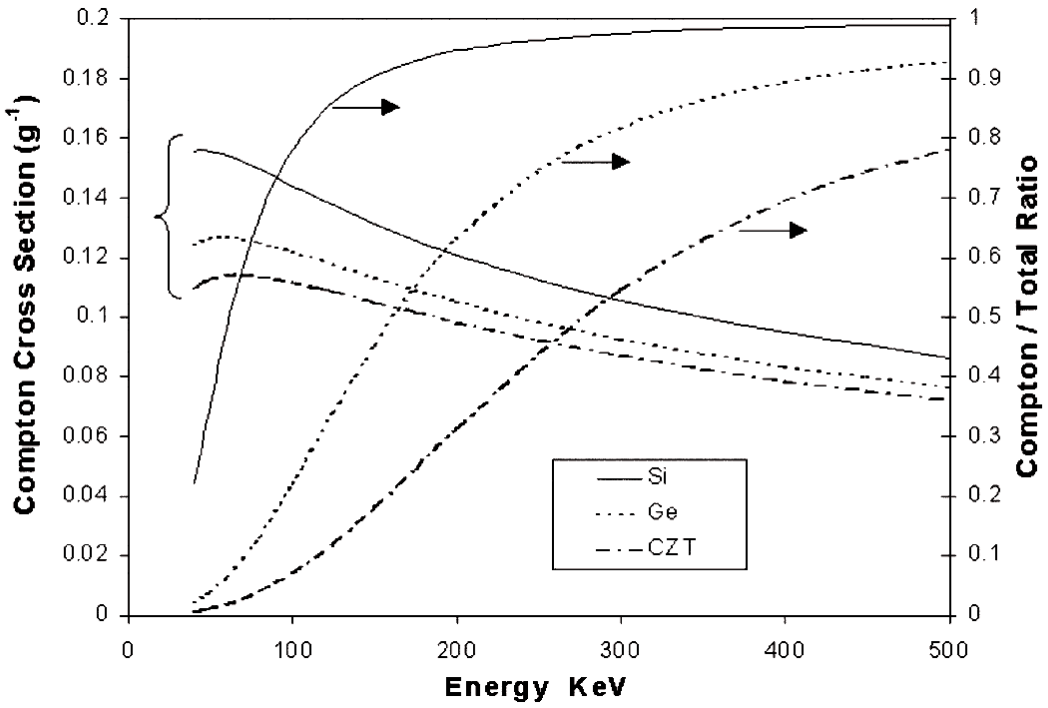

Figure 26: Compton cross section and Compton/Total cross section ratio for Si, Ge, and CZT (Wernick and Aarsvold 2004).

The Compton/ total cross section ratio is higher for Si, however, the Si volume should be twice the Ge to obtain the same probability of Compton interaction due to the low density of silicon. From Figure 26 it is apparent that the Compton/ total cross section is a function of energy. For low incident gamma-ray energy most of the photons will be photoelectrically absorbed and few photons will interact by Compton scatter in the front detector. Therefore, the uncertainty in measuring the scatter angle increases by using low gamma-ray source energy due to the very little energy measured in the front detector as

well as the effect of Doppler broadening. For instance, only 18% of the incident photon energy is transferred to the recoil electron when a 140 keV photon is scattered by 80°, whereas, 50% of the incident 662 keV photon energy is transferred to the recoil electron in the same scatter angle. This explains why the Compton camera performs better with increasing the source energy (Phillips 1995).

From NIST tables (Berger at al 1990) for 662 keV photons incident to 0.4 cm thick germanium detector the transmission factor ($e^{-(\mu/\rho)x}$) is 0.84 and the absorption factor ($1-e^{-(\mu/\rho)x}$) is 0.16 , where (μ/ρ) is the mass attenuation coefficient and x is the mass thickness. Table 10 summarise the probability of interaction with the front detector for different source energies. The results in Table 10 show that with high source energy (>300 keV) more than 90% of the photons will interact with front detector by Compton scattering, whereas the percentage of photons absorbed in the front detector increase with low photon energies. As shown in Table 10 the Compton/photoelectric ratio is a function of source energy.

E source (keV)	% of photons interacting with Front pixel	% of photons that photoelectrically absorbed in FD	% of photons that is Compton scattered in FD
140	46.4 %	53.1%	48.7 %
360	21.4 %	9.4%	91.3 %
511	17.8 %	4.2%	94.3 %
662	15%	2.5%	95.6%

Table 10: interaction probabilities for different energy sources placed 10 cm from the front detector pixels.

3.1.1 With the absorption (back) detector

The results in Table 10 can be used to estimated the fraction of photons incident to the back detector which can be calculated by multiplying the solid angle subtended by the back detector Ω_b with the fraction of photons that interact with front detector by Compton scatter ($front_{Cs\gamma}$) as shown in (23):

$$photons\ incident\ to\ the\ front\ detector = front_{Cs\gamma} \ . \ \Omega_b \quad \textbf{(23)}$$

From the theoretical calculation of the front energies in Table 9 the energy of the photons incident to the back detector can be estimated. For instance, if a 662 keV source is imaged and the energy measured in the front detector is 182 keV for a photon scattered by 50º toward the back detector then the energy of the scattered photon can be calculated by subtracting the source energy from the energy measured in the front detector. Thus, in the previous example the scattered photon energy is 480 keV. From NIST tables, only 37% of the scattered photons with this energy will interact with the back detector and the rest will transmit through the detector without interaction. Table 11 summaries the theoretically expected fraction of photons interacting with the back detector by photoelectric absorption and Compton scattering.

E source (keV)	% of photons that photoelectrically absorbed in back detector	% of photons that is Compton scattered in back detector
140	56.1 %	34.6 %
360	15.4 %	79.2 %
511	8.7 %	87.6 %
662	6.2 %	90.3 %

Table 11: the theoretically expected no. of photons interacts with the back detector (1cm thick) and probability of PE and CS for different source energies.

The results in Table 11 show that the fraction of photons that interact with the back detector by Compton scatter is a function of the source energy. The principle of Compton

camera imaging favours the probability of single Compton interaction in the front detector followed by a total residual energy deposition in the back detector (Wernick and Aarsvold 2004). Nevertheless, the back detector is used mainly to detect the position of the photon which is considered to be in coincidence with the front detector regardless of its energy "as long as it lies within the energy window" to define the axis of the cone in the reconstruction process. Thus, optimising the back detector position sensitivity is important.

To verify the theoretical estimations of the energy deposited in both detectors a Cs^{137} source was placed at 5 cm from the front detector and the energy deposited in both detectors were measured. The measured energies of 9,000 coincidence events were plotted against the frequency of occurrence (counts) as shown in Figure 27.

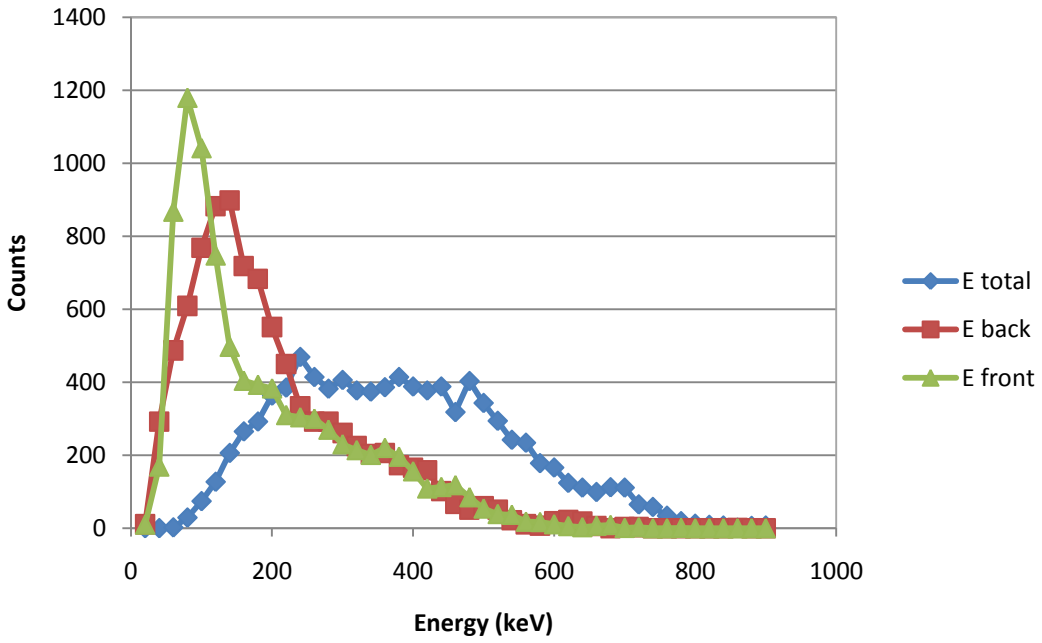

Figure 27: The measured front, back, and total energy deposited in the camera by a 662 keV source.

The result in Figure 27 shows that majority of incident photons deposit energy range from 60 to 120 keV in the front detector which correspond to 20° to 35° scattering angle as

shown in Table 9. In average the measured front energy is about only 18 % of the source energy due to the small detector thickness (4 mm). The measured energy in the back detector shows that the photons incident to the back detector deposit only part of its energy range from 120 to 160 keV (~ 20 % of source energy). Note that higher energies were recorded in the back detector compared to the front detector due to its 10 mm thickness.

The total energy measured for every coincidence event shows that with 662 keV source most of coincidence photons escape without full deposition of its energy. The result in Figure 27 shows that the majority of the events deposit total energy which range from 220 to 440 keV in both detectors. Thus, wide energy window width was used to avoid loss of useful true events as discussed in section (2.2.3) the energy window was set to 450 keV for 662 keV photons imaging. Possible reason of incomplete energy deposition in the detectors is the high source energy used for this analysis (662 keV) compared to the small thickness of the detectors (4 and 10 mm). Therefore, the incident photons have high Compton scatter probability in both detectors, as indicated earlier, and loss only part of its energy rather than its total energy.

3.1.2 Random coincidence in Compton camera

The method of coincidence detection used in Compton camera has an obstacle (similar to PET) in that two unrelated photons might accepted simultaneously within the same coincidence timing window mainly due to the finite uncertainty in the time of arrival of a photon at the detector (Webb 1988). These events are called random (accidental) events. The direct consequence of random events is the addition of noise to the measured data due to the inaccurate assignment of the lines of response in PET and cone axis parameters

in Compton camera. It is difficult to distinguish a random from a genuine coincidence event (Webb 1988). The random events increase as the square of source activity (Budinger 1998). Correction of random events is the focus of ongoing research in PET (Rahmim and Zaidi 2008). Mathematically, the random events rate for a particular LOR connecting to detectors i and j is given by:

$$R_{ij} = 2\tau S_i S_j \tag{24}$$

Where τ is the coincidence time window and S_i and S_j refer to the singles rates at the two detectors (Rahmim and Zaidi 2008). The conventional approach to correct for random events in PET is to observe the rate of events in a second delayed-coincidence window and subtract the estimate of the random from the measured coincidence. However, this approach does not remove and increases the noise in the data along with producing data which is no longer Poisson distributed (Rahmim and Zaidi 2008). Alternatively, an average estimate of the single rates can be modelled and included in the image reconstruction task to avoid the problem associated with the subtraction technique (Oliver and Rafecas 2010). The estimate of singles rate and the expected random events can be calculated using (24). The single rate estimation method has less noise than the delayed window method because it uses exclusively true coincidence counts. Effort is needed to implement and develop random events correction techniques for Compton camera data.

The geometrical arrangement of the camera (refer to section 2.1) impose a limitation at high counting rate in that the rate of single events in the back detector becomes prohibitive. The single events have two main effects: the first is the increase in the system dead time due to the time needed to process the high number of events collected. The

second effects are the increase probability of random coincidence events detected as shown in Figure 28.

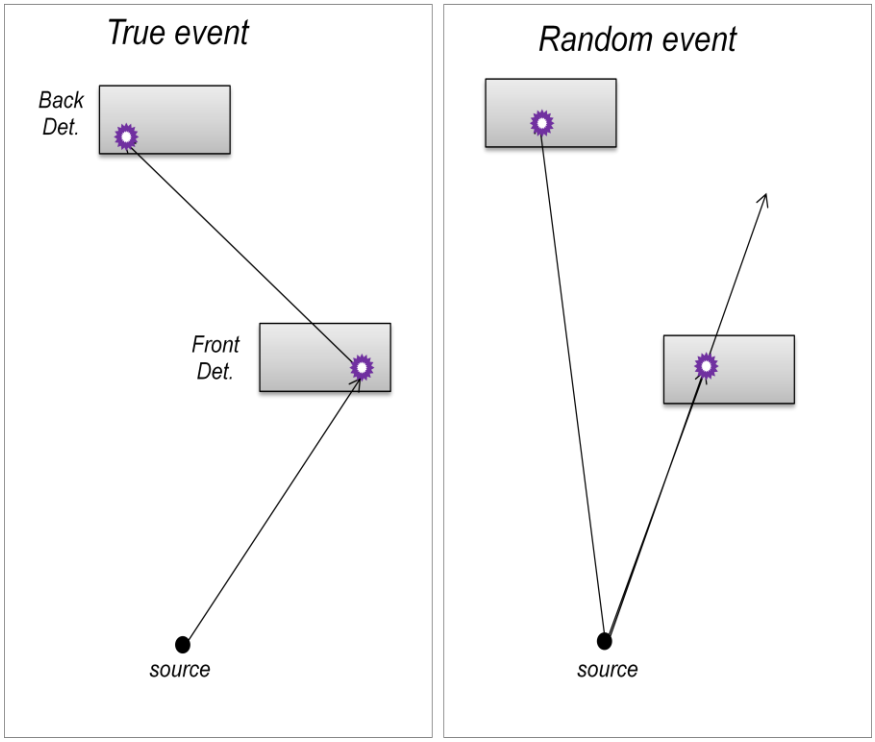

Figure 28: Types of coincidence events in Compton camera; true events (left) and random events (right).

Partial shielding of the back detector is appealing because it offers a way to reduce the random events without largely reducing the system sensitivity to true events. Thus, if a proper shielding is provided against direct photons from the source such that only photons that scatters in the front detector is allowed to hit the back detector, thus, reducing the single events rate.

A lead brick (50 mm thickness) was placed beneath the central axis of the camera to minimise single hits for the back detectors as shown in Figure 29. This lead thickness will lead to reduce the number of gamma rays transmitting through to the back detector by ~ 40% providing that the lead shield is between the source and back detector.

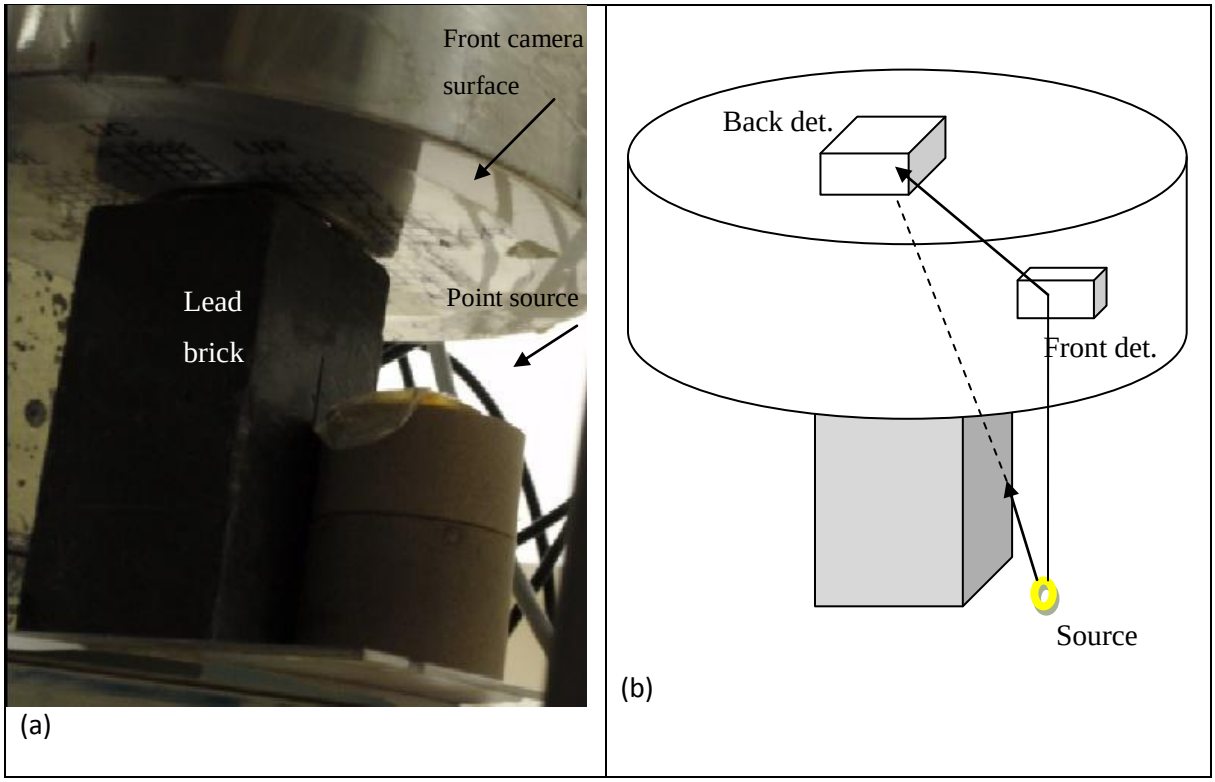

Figure 29: (a) photograph of the experiment setup with lead brick to shield the back detector (b) sketch of the setup with the expected path of the photons

To see the effect of this technique on reconstructed image quality a Cs^{137} point source was imaged with and without shielding the back detector. The source was placed at 10 cm from the camera front surface and imaged for 24 hours. The images are shown in Figure 30. As expected, the number of counts collected has reduced with shielding the back detector compared to the image without shielding. Despite the reduced sensitivity (~ 20%) with shielding the back detector the SNR of the image taken with the shielding has improved by a factor of 2 compared to the image without shielding.

Without shield	With shield
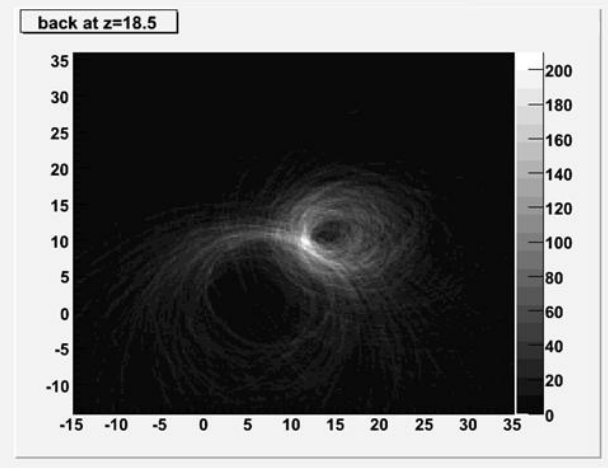	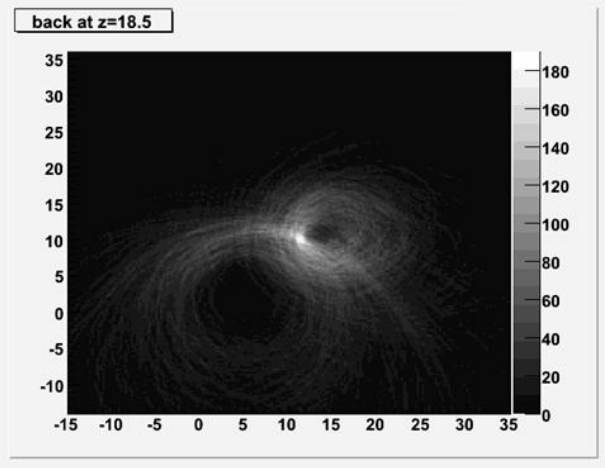
(a) Number of events = 5599	(b) Number of events = 4491
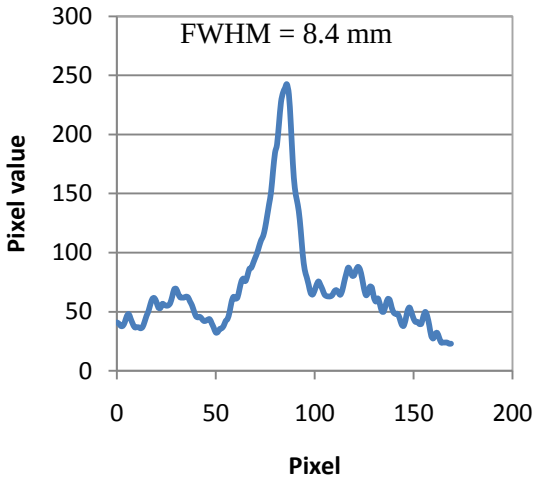	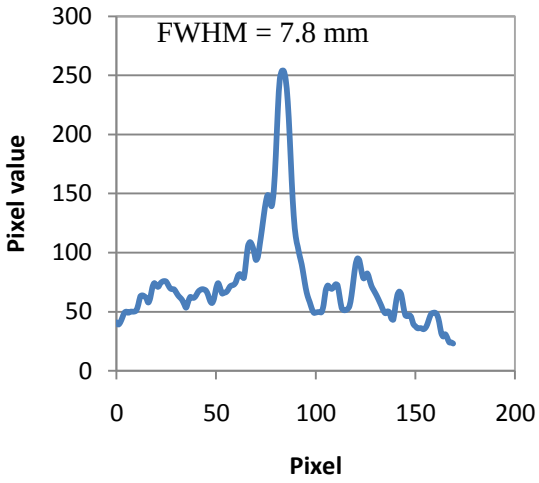
(c)	(d)

Figure 30: Cs^{137} point images acquired with and without shielding the back detector pixels.

The PSF was measured for the images as shown in Figure 30 (c) and (d). The FWHM value has slightly improved by ~ 7% with shielding the back detector which is explained by the reduction of noise in the data and the minimized degradation effect of random events on the image quality.

This crude shielding setup proved that the image quality can be improved by minimising single events rate. Nevertheless, the shielding can be more effective to further reduce the singles count in the back detector if a lead disk is placed in front of the inactive inner

region of the front detector such that the lead shield is placed between the source and the back detector (Royle et al 2004).

Since the geometrical coverage of the camera decreases with extended source distribution, a higher fraction of the singles is expected to hit the back detector. Consequently, the partial shielding technique becomes less effective and depends on the source geometry. Proper modelling of the estimated singles with different source distributions (to include it in the reconstruction task) such that the estimation is independent of the source geometry is required. Singles rate approximation becomes more correct with extended source (Oliver and Rafecas 2010). Therefore, appropriate estimation of random coincidence and their enclosure in the image reconstruction algorithm can remove the bias in the images and minimize the noise amplification in the data without altering the camera geometry (Rahmim and Zaidi 2008).

3.2 System performance characterises

There are several factors that define the performance characteristics of the Compton camera. These can be classified into hardware, software and physics related factors. The hardware factors include the detector materials, geometry, and the readout electronics. The physics related factors include the Doppler effects, random/true coincidence ratio, and multiple Compton scatter issues. In addition, the characteristics of the software used to process and reconstruct data are another factor that influences the system performance because they play an important role in defining the image quality. The technicalities of the Compton camera cannot be fully understood nor be optimized for clinical use, unless these factors are addressed. In this section the main parameters that characterise the system performance of the UCL prototype Compton camera will be demonstrated.

3.2.1 Energy resolution

To relate the energy of the incident radiation accurately with the signal detected by the interaction of radiation with the detector the system was calibrated by acquiring gamma ray photopeak spectra for different gamma ray energies. Two sources with different energies (Ba^{133} and Cs^{137}) were used. The photopeak energies and their corresponding ADC responses are fit with a linear gamma-ray energy calibration curve as shown in Figure 31. Calibration curves were generated for all the pixels currently in use (31 pixels). Slight variation (about 0.8 keV) was noticed from pixel to pixel which might be due to the fact that each pixel has an independent preamplifier and amplifier that result in slightly different output.

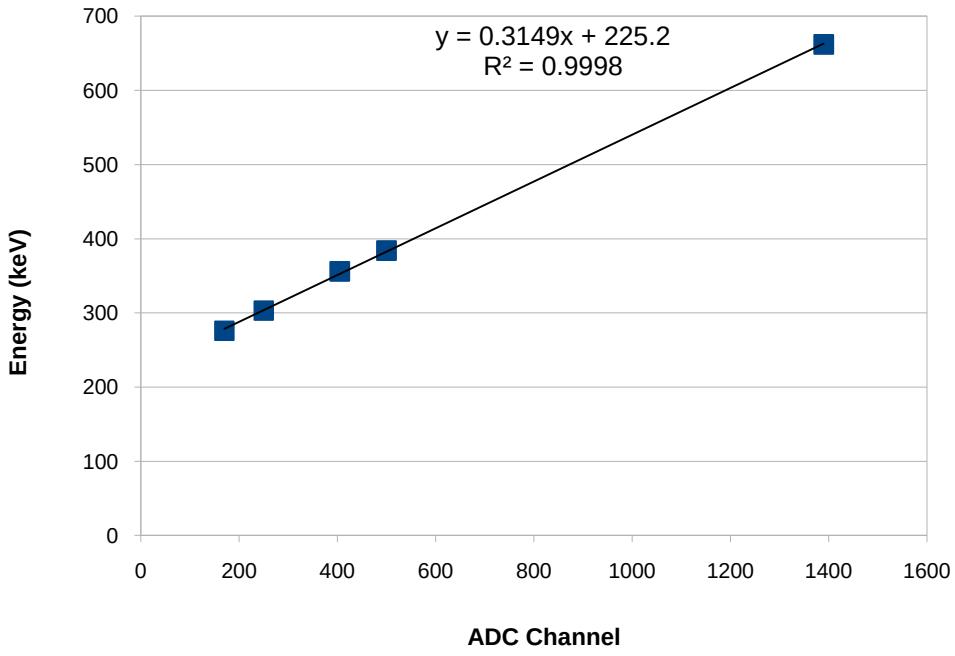

Figure 31: Energy calibration linearity curve for a front pixel (CR11) based on Ba^{133} and Cs^{137} photopeaks.

Figure 31 shows the energy calibration curve in that the energy is plotted against the ADC channel. The detector function was found to be linear with the spectral response and the R^2 suggests a good fit. A comparison between the GRT4 readout electronics and the analog NIM standard electronics energy resolution values was carried out. NIM standard electronics was used to set a benchmark.

The energy resolution was measured by histogramming the collected events from each pixel to from an energy spectrum. The average energy resolution for the HPGe Compton camera is 1.8 keV (0.5%) and 1.9 keV (0.3%) for 356 and 662 keV respectively across all pixels was achieved with the standard NIM electronics multi-channel analyzer (MCA). With using the MWD energy extraction algorithm the average energy resolution obtained with GRT4 readout electronics 4.2 keV (1.2%) and 4.6 keV (0.7%) for 356 and 662 keV respectively. Figure 32 shows the energy resolution values across all active pixels along with pixel maps obtained with NIM and GRT4 electronics.

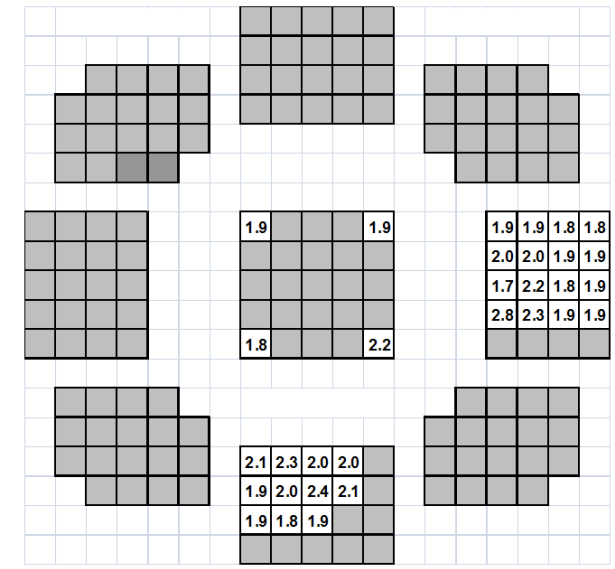

	NIM	
	%	keV
LC11	0.32	2.11
LC12	0.35	2.31
LC13	0.31	2.05
LC14	0.30	2.01
LC21	0.29	1.90
LC22	0.31	2.08
LC23	0.36	2.41
LC24	0.32	2.15
LC31	0.29	1.89
LC32	0.28	1.88
LC33	0.29	1.93
CR11	0.30	1.96
CR12	0.29	1.93
CR13	0.28	1.87
CR14	0.27	1.82
CR21	0.31	2.04
CR22	0.30	2.01
CR23	0.29	1.94
CR24	0.30	1.96
CR31	0.27	1.79
CR32	0.34	2.22
CR33	0.27	1.82
CR34	0.29	1.92
CR41	0.42	2.80
CR42	0.35	2.30
CR43	0.29	1.93
CR44	0.29	1.91
BC11	0.29	1.94
BC15	0.29	1.93
BC51	0.28	1.87
BC55	0.34	2.22

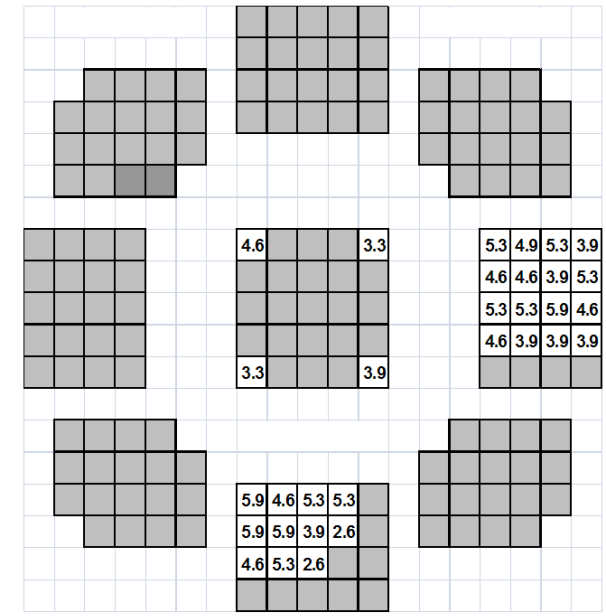

	GRT4	
	%	keV
LC11	0.90	5.96
LC12	0.70	4.63
LC13	0.80	5.30
LC14	0.80	5.30
LC21	0.90	5.96
LC22	0.90	5.96
LC23	0.60	3.97
LC24	0.40	2.65
LC31	0.70	4.63
LC32	0.80	5.30
LC33	0.40	2.65
CR11	0.80	5.30
CR12	0.70	4.63
CR13	0.80	5.30
CR14	0.60	3.97
CR21	0.70	4.63
CR22	0.70	4.63
CR23	0.60	3.97
CR24	0.80	5.30
CR31	0.80	5.30
CR32	0.80	5.30
CR33	0.90	5.96
CR34	0.70	4.63
CR41	0.70	4.63
CR42	0.60	3.97
CR43	0.60	3.97
CR44	0.60	3.97
BC11	0.70	4.63
BC15	0.50	3.31
BC51	0.50	3.31
BC55	0.60	3.97

Figure 32: The energy resolution pixels map along with the FWHM table for the NIM analogue electronics (top) and the GRT4 electronics (bottom) obtained with 662 keV source.

The FWHM values obtained with the MWD method are factor of 3 worse than the value measured with the analogue NIM electronics. This is mainly due to the noise arising from all the preamplifiers of the detector connected to the GRT electronics compared to the

NIM analog system which was connected with only one channel under test. Also, the MWD setting parameters (mentioned in section 2.2.1) need adjustment and fine tuning to obtain the required filtering. The FWHM value for a 662 keV energy peak was measured as a function of the MWD window width as shown in Figure 33.

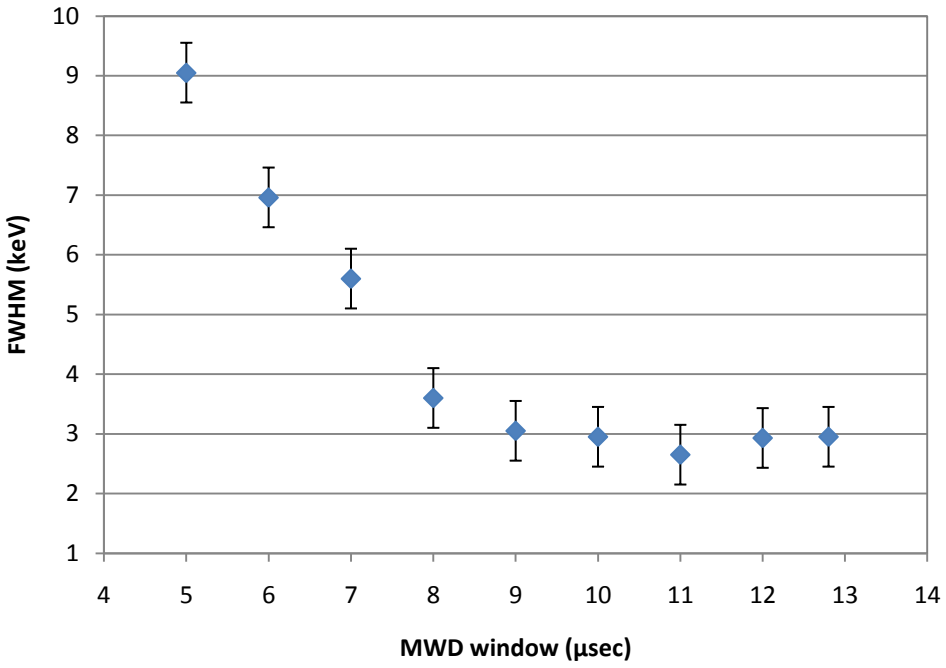

Figure 33: The FWHM value energy vs. the MWD window width. The bars represents the standard errors.

The results showed that energy resolution values depend strongly on the width of the deconvolution window and a minimum window of 8 µs needs to be used to obtain good energy resolution, and the best FWHM was obtained with 11 µs window. Similar result was found by (Descovich 2002). Therefore, optimizing the MWD window width in the GRT4 system for accurate energy extraction is required.

Another method that can be used as an alternative to MWD method which is based on wavelet transform pulse shape analysis was presented by (Yousefi and Lucchese 2008). This method is based on using wavelets to discriminate between pulse shapes in the frequency domain rather than in the time domain, thus, provide efficient energy

determination and improved performance due to its features which are less sensitive to the pulse shape and though less sensitive to the signal noise. This algorithm can be easily implemented with FPGA technology. However, this method was not compared quantitatively with MWD and has no prove that it will provide an enhanced energy resolution for gamma-ray spectroscopy.

3.2.2 Angular resolution

The angular resolution was measured experimentally and compared to theoretical estimations as will be demonstrated in the following sub-sections. The overall angular resolution was estimated theoretically by using Singh's (1983) quadratic addition in (2), refer to section 1.7.2.1. The combined angular resolution including all uncertainties is calculated as a sum in squares of the uncorrelated geometrical contribution and the combined effect of Doppler broadening and limited energy resolution. The following sub-sections illustrates the calculated contributions of these factors to the angular resolution for a 662 keV emitted photons from a source placed at 5 cm from the camera front surface.

3.2.2.1 **Energy resolution contribution**

The combined effect of the system energy resolution and Doppler broadening on the overall angular resolution was calculated from (3) and (7). The calculation assumes an intermediate scattering angle 45°. The system measured average energy resolution is 4.6 keV for 662 keV incident gamma-ray energy. Therefore, from (3) the contribution of energy resolution for the overall angular resolution is 0.07°.

In addition, (7) was used to calculate the contribution of Doppler broadening to the angular uncertainty. Table 12 shows the effect of Doppler broadening on the angular

resolution which was calculated for 360 keV and 662 keV photon energies. The results obtained were derived using (6), 8 , and 9 which were discussed in details in (section 1.7.2.1).

	360 keV	**662 keV**
p_z *(a.u)*	121	146
k_θ	2.3 x10^{22}	9.3 x10^{22}
k_{pz}	1.1 x10^{21}	1.5 x10^{21}
σ_θ	0.062°	0.021°

Table 12: the electron momentum, the contribution of energy resolution, the contribution of Doppler broadening and the angular uncertainty due to Doppler broadening for 360 and 663 keV source energy.

As shown in Table 12 the effect of Doppler broadening on the angular resolution increases with low source energy. Therefore, the contribution of the system energy resolution and Doppler broadening on the overall angular resolution $\Delta\Theta_1$ is 0.09°. The expected system energy resolution with a germanium detector is 2 keV, as achieved with the analogue NIM electronics (section 3.2.1). This energy resolution could reduce the $\Delta\Theta_1$ contribution to 0.05° to the overall angular resolution. Thus, enhanced system energy resolution will improve the angular resolution by about 30%. The system energy resolution is limited by the effect of electronic noise level and the Doppler broadening effect.

3.2.2.2 **Geometry contribution**

The contribution of geometry to the angular resolution was computed using

(12), 13, and 14. The geometrical effect on the overall angular resolution with 662 keV source placed at 5 cm from the camera front detector was calculated. The contribution of the pixel size (width and thickness), solid

angle subtended by the front detector and separation between detectors ($\Delta\theta_2$) and ($\Delta\theta_3$) equals 2.8° and 0.5° respectively. As indicated by Singh (1983) the geometry contribution ($\Delta\theta_2$) to the angular uncertainty is inversely proportional to the separation between the two detectors. For instance, if the separation between the two detectors is 5 cm $\Delta\theta_2$ will increase to 3.2° and if the separation increased to 15 cm the contribution $\Delta\theta_2$ to the angular uncertainty decrease to 2.5°. However, increasing the separation between the two detectors will decrease the Compton camera efficiency because the solid angle subtended by the back detector will decrease. Thus, the detectors separation should be carefully chosen to compromise between efficiency and angular resolution (Du et al 2001).

In addition, the position resolution contribution ($\Delta\theta_4$) was calculated using (14). The achievable position resolution in the current system with applying simple pulse shape analysis technique is 2 mm (as explained in section 2.9.1). From (14), with 2 mm position resolution ($\Delta\theta_4$) equals 0.57°. Note that without pulse shape analysis the realistic position resolution equals the pixel size is 4 mm and the contribution to the overall angular resolution will be 1.12° i.e. worse by a factor of 2. Nevertheless, by measuring the rise time and the polarity of the induced charges 1 mm position resolution is obtainable which translates to ($\Delta\theta_4$) of 0.28° i.e. improvement by a factor of 2. Table 13 summaries the theoretically calculated factors that contribute to the angular uncertainty for a 662 keV source placed at 5 cm from the front detector.

Factor	Angular uncertainty (degree)
Energy resolution $\Delta\theta_1$	0.09°
Geometry $\Delta\theta_2$	2.8 °
Geometry $\Delta\theta_3$	0.50 °
Position resolution $\Delta\theta_4$	0.57 °

Table 13: Summary of the calculated factors that contribute to the overall angular resolution using in Singh's quadratic equation for a 662 keV source placed at 5 cm.

As expected the effect of energy resolution is smaller than the geometrical effect due to the excellent energy resolution of the germanium detector. From Table 13, the theoretically calculated angular resolution for 662 keV source placed at 5 cm from the camera front detector is 3.96 º which is translated to 3.4 mm spatial resolution. Note that the angular uncertainty is dominated by the geometrical contribution ($\Delta\theta_2$) of the detectors. Note that the camera geometry is fixed in the current prototype and cannot be modified.

3.2.3 Point source images

The angular resolution was measured by imaging a range of point source energies and compares it to the theoretical predictions in (section 3.2.2). The PSF was measured for point source images obtained from single view (limited geometry) and compared to images obtained from multiple views as will be presented in the following sections.

3.2.3.1 Limited geometry images

As described in (section 2.1) a few number of pixels are currently active (31 out of 177 pixels) and, thus, the images are obtained from a limited pixel geometry compared to the proposed full system. The images for different radioisotopes placed at 5 cm away from the camera front detector are shown in Figure 34. The effect of the geometry is reflected

by the asymmetric cones allocation in the reconstructed images in Figure 34. The reason of having asymmetric point shape is due to the fact that asymmetric pixels geometry is used in this experiment that result in non-uniform overlapping cones associated with a specific combination of front and back pixel. The Ba^{133} and Cs^{137} images were reconstructed with 3000 coincident events in Figure 34 (a) and (b). The Na^{22} image in Figure 34 (c) was reconstructed with 100 events. The source activities used are 3.7, 0.37, and 0.1 MBq for Cs^{137}, Ba^{133}, and Na^{22} respectively. The imaging time used for data collection is 96 hours for Ba^{133} and Na^{22} and 10 hours for Cs^{137}. The cross marked in Figure 34 indicates the nominal source location (from the experiment setup) and it can be seen that the algorithm reconstructed the point source within few millimetres from the expected source position and within the expected measurement position uncertainty ($\pm$ 2 mm).

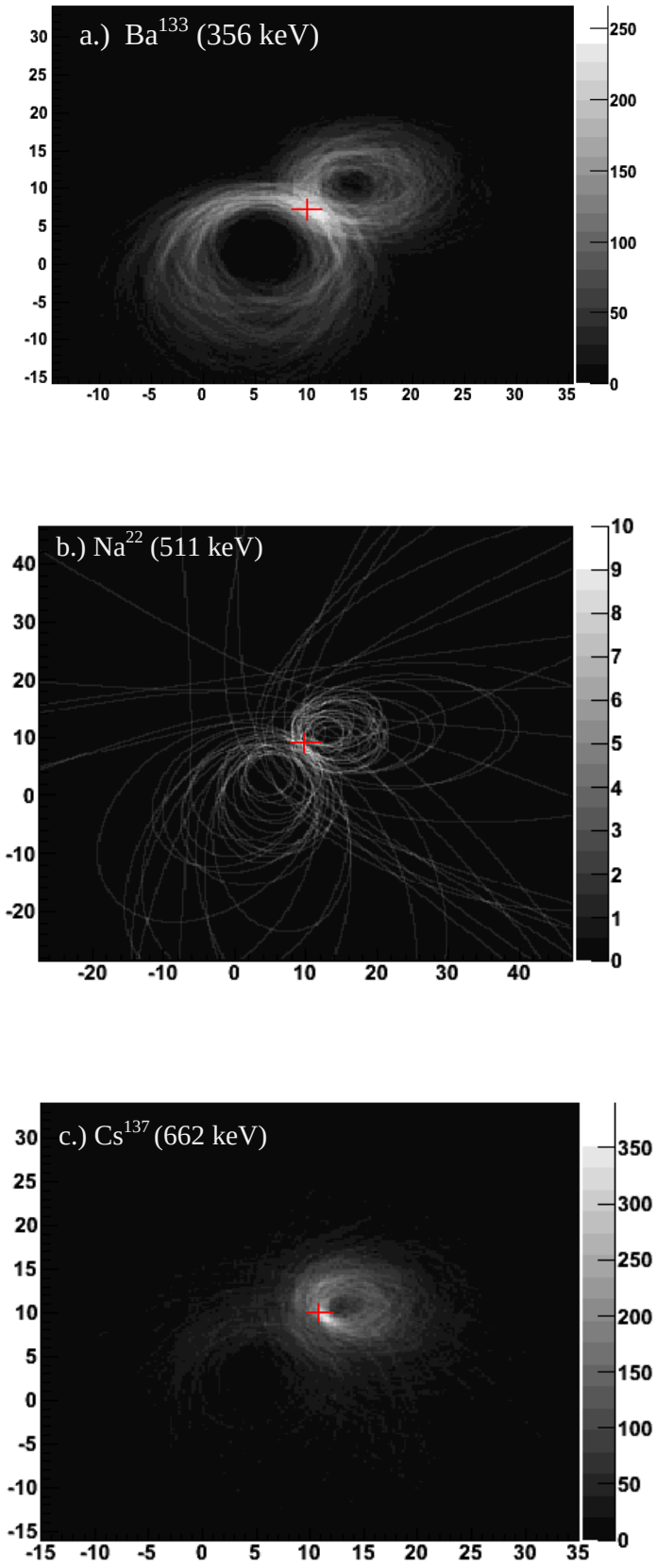

Figure 34: Limited geometry point source images acquired with different source energies (a) 356 keV, (b) 511 keV, and (c) 662 keV. The cross indicates the nominal source position.

These overlapped cones in Figure 34 results in an image artefact which can be removed by using a more sophisticated image reconstruction algorithm as explained in (section 2.3.4). A technique to reconstruct the point source image with a uniform symmetric distribution by acquiring multiple views for the source to overcome the current asymmetric pixels geometry limitation will be discussed in the (section 3.2.3.2).

The FWHM at 5 cm are 7.5, 7.2, and 6.9 ± 2 mm for 356, 511 and 662 keV gamma energies respectively as shown in Table 14. The FWHM value was measured by taken the mean value of the profiles taken from different angles through the point source. The approximated errors in each value equals to one-half the pixel size (Singh 1983). The measured FWHM translates into angular resolution (σ_θ) of the camera using the following formula (Singh 1983):

$$\sigma_\theta = \arctan\left(\frac{FWHM}{d}\right) \quad \textbf{(25)}$$

Where d is the distance between the source and the front detector. Using (25) the measured PSF (mm) translates to angular resolutions of 8.5°, 8.2°, and 7.8° for 356, 511 and 662 keV gamma energies respectively.

E (keV)	356		511		662	
Image type	Exp	theory	Exp	theory	Exp	Theory
FWHM (mm)	7.5	3.7	7.2	3.6	6.9	3.4
Angular resolution	8.5º	4.2 º	8.2º	4.1 º	7.8º	3.9 º

Table 14: The experimental (Exp) measured and the theoretically calculated (theory) angular and spatial resolution at 5 cm from the camera. The error in the measurement is half the pixel size (± 2 mm).

As shown in Table 14 the disagreement between theoretical and experimental values is due to the fact that the effect of the random events, dead time, and the reconstruction algorithm decoding penalty were not considered in the theoretical calculation. The geometry effect resulted in worse than theoretically expected angular resolution as shown in Table 14. The FWHM values in Table 14 were plotted for different source energies as shown in Figure 35 .

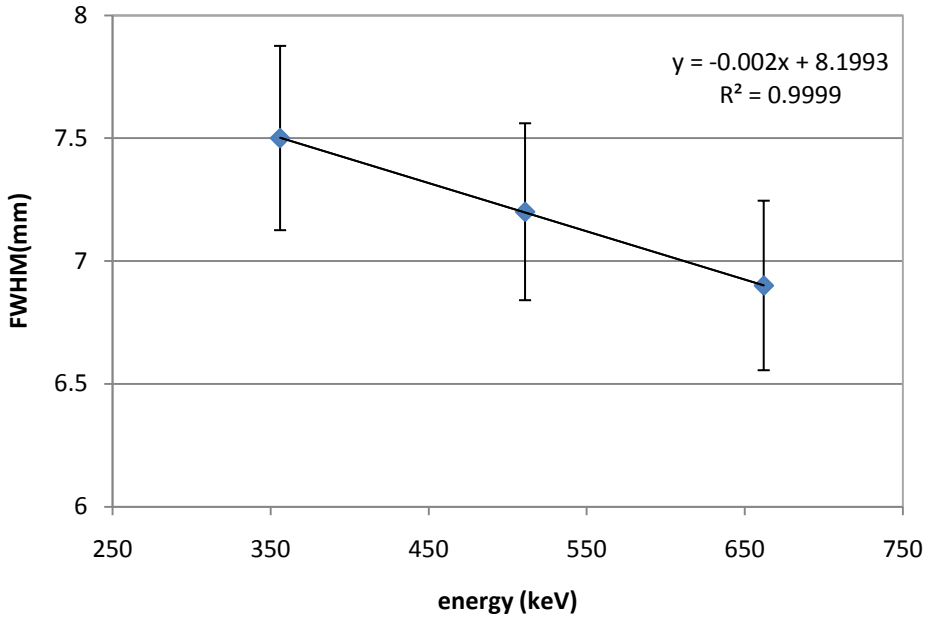

Figure 35: The experimental measured FWHM (mm) for 356, 511, and 662 keV. The R^2 suggests a good fit.

The results in Figure 35 show that the measured spatial resolution is a function of source energy. However, the inherent system spatial resolution limitation makes the relation between the spatial resolution and energy invariable at certain point. From the graph linear equation it can be concluded that the camera resolution at 140 keV gamma energy is 7.9 mm.

3.2.3.2 **Multiple views images**

The limited-angle views of the projection data are insufficient to correctly reconstruct the distribution of activity. Limited-angle imaging presented in the previous section induces image artefacts and produce geometric distortions perpendicular to the direction of the acquired projections. Therefore, the technique mentioned in (section 2.3.6) was used to image a Cs^{137} point from different angles around the camera central axis. The source was placed 3 cm from the front detector and imaged from 8 different positions as shown in Figure 36. Then, all the images acquired at different angles were summed together resulting in an image of cones intersecting from eight different angles at the location of the point source as shown in Figure 37.

The superimposed summed image provides a more accurate representation for the actual source distribution as seen in Figure 37 (b). The number of events collected in each position was 3000 and the final summed image was reconstructed with 24,000 coincidence events. The total acquisition time is 8 days i.e. 24 hours per view. The long acquisition time is mainly due to the limited number of pixels and slow readout electronics.

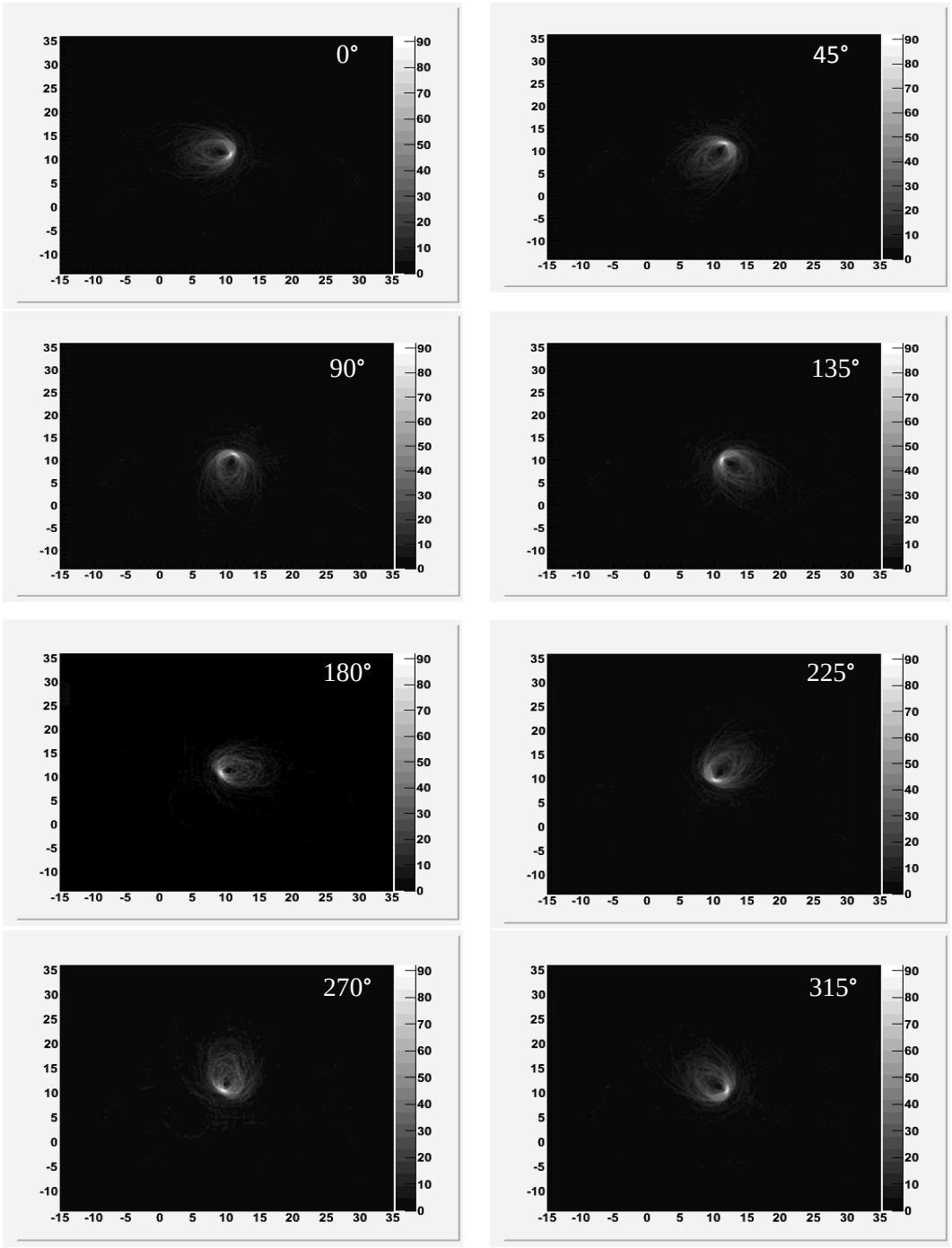

Figure 36: point source images acquired from different angles

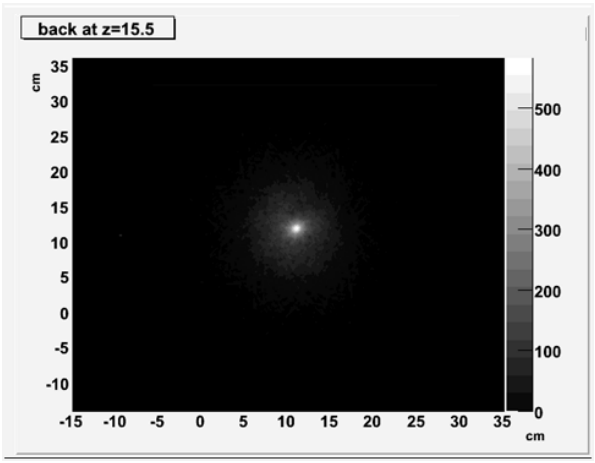

(a)

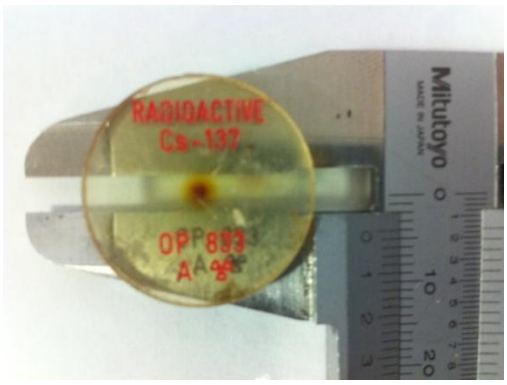

(b)

Figure 37: The 8 views superimposed point source image (a) a photograph of the point source used in this experiment (diameter =2 mm).

a.) Comparison between limited geometry and multiple views images

Horizontal and vertical line profiles have been taken through the point source for the multiple and single view (limited geometry) images obtained at 3 cm from the camera as shown in Figure 38. The statistical theory predicts that the overall response function will always tend toward Gaussian shape (G F Knoll. 1999). Thus, the profiles have been fitted with the sum of Gaussian describing the point source intensity to represent the response function of the detector system. To define the continuum area under the peak a 2^{nd} and 3^{rd} order polynomial curve was fitted to describe the background in Figure 38. Polynomial fitting is an effective way to characterise the variations of the background appearance that results from the presence of any source of intensity changes due to nuisance factors like camera gain variations, noise, and reconstruction artefacts (Rogers et al 2007, Lanza et al 2010).

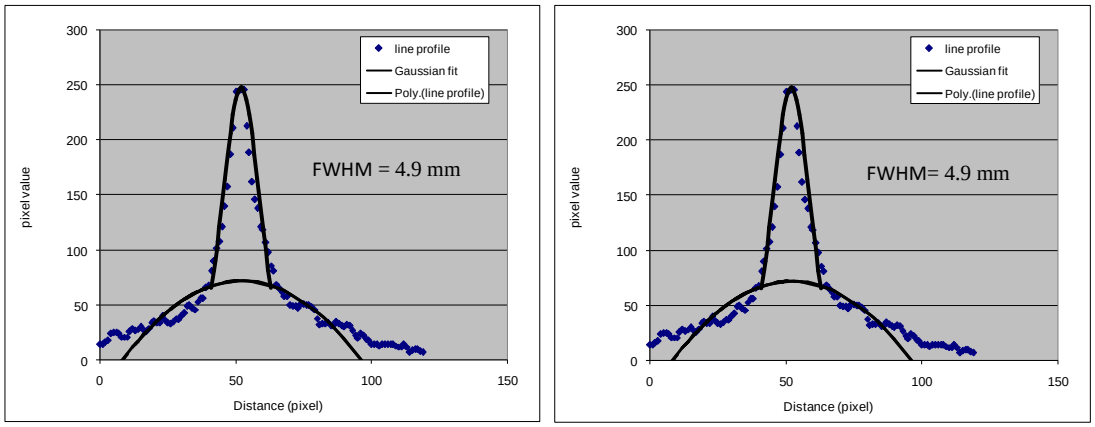

(a) Multiple views horizontal profile (b) Multiple views vertical profile

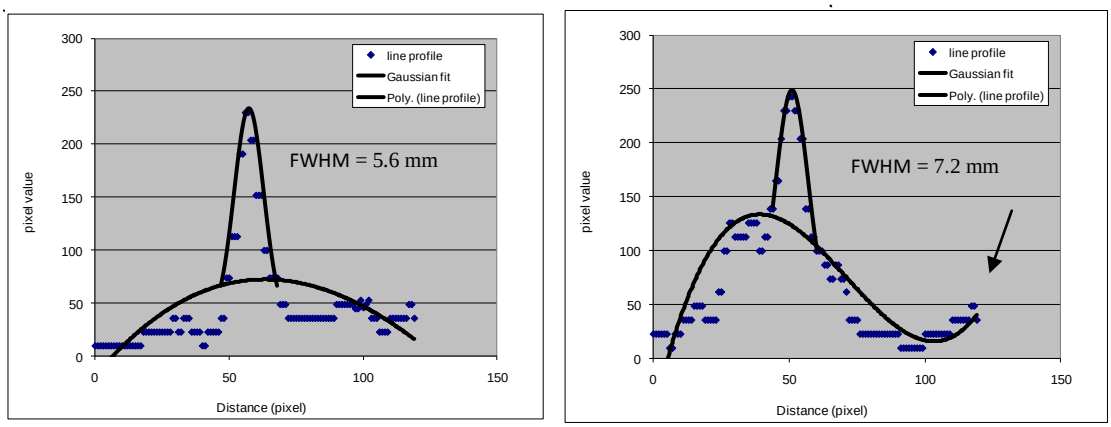

(c) single view horizontal profile (d) single view vertical profile

Figure 38: horizontal and vertical line profiles taken through the centre of the single and multiple view images. The reason of the poor background polynomial fit in (c) and (d) is due to the discrepancies in the background noise intensities along the line profile taken through the single view image at 180º (see figure 36). The cones overlap is perpendicular to the angle of acquisition and, thus, build up an asymmetric increase pixels density in one direction. The shape of profile (d) indicated by the arrow is due to the position and size of the line profile taken that does not cover all the distortion area in the image i.e. by extending the size of the line profile the pixel value will drop to the minimum value.

The results in Figure 38 show that the multiple view method has quantitatively improved the image quality. In the multiple views image the cones are isotropically distributed and intersect uniformly with the image plane in all directions and reflects the expected Gaussian response of the system. Thus, provide more accurate representation of the

imaged object shape. The FWHM value for the multiple view image line profile is 4.9 mm in both x and y directions which translates into 4.6° using (25). The inconsistency of the profile tails shown in Figure 38 (c) and (d) the multiple peaks and the distortion in the profiles caused by the backprojection artefact is seen only from one direction depending on the source position. The discrepancies in the background contribution in the single view images are due to the current system asymmetric active pixel configuration.

In Figure 38, a significant widening of the profile at the base is observed. To specify the severity of tailing the ratio of the full width at tenth maximum (FWTM) to full width at full maximum (FWHM) was calculated. The FWTM/FWHM ratio for the x profile is 6.7 and 5.7 for the single and multiple view images respectively. Table 15 shows a quantitative comparison between multiple and single view images.

	Δx (mm)	*Δy (mm)*	SNR	% Contrast
Single view (limited geometry)	5.6	7.2	3.1	78.2
Multiple view	4.9	4.9	4.2	82.7

Table 15: Quantitative comparison between multiple and single view images at 3 cm.

The results in Table 15 show that the image quality has improve with the multiple view technique compared to the limited pixel geometry image. The contrast has improved in the multiple-view image by 5% and the SNR has improved by 25 % compared the single view image as shown in Table 15. This improvement can be explained by the enhanced image sampling accuracy with the multiple-view imaging of the source.

b.) Partial volume effect (PVE)

The effective source diameter is 2 mm which is smaller than the achievable system spatial resolution. Since the source size is smaller than the theoretically predicted system resolution (~ 4 mm) the apparent size of the source in the image reflects larger than the actual source activity distribution, this effect is known as the partial-volume effect PVE (Sorenson and Phelps 1987). The PVE cause part of the signal from the source to spill out into adjacent image pixels and, hence, the contour of the voxel does not match the actual source contour due to the finite spatial resolution as demonstrated in Figure 39. Note that PVE just displaces the signal in the image and decrease the apparent source intensity without causing any loss of signals.

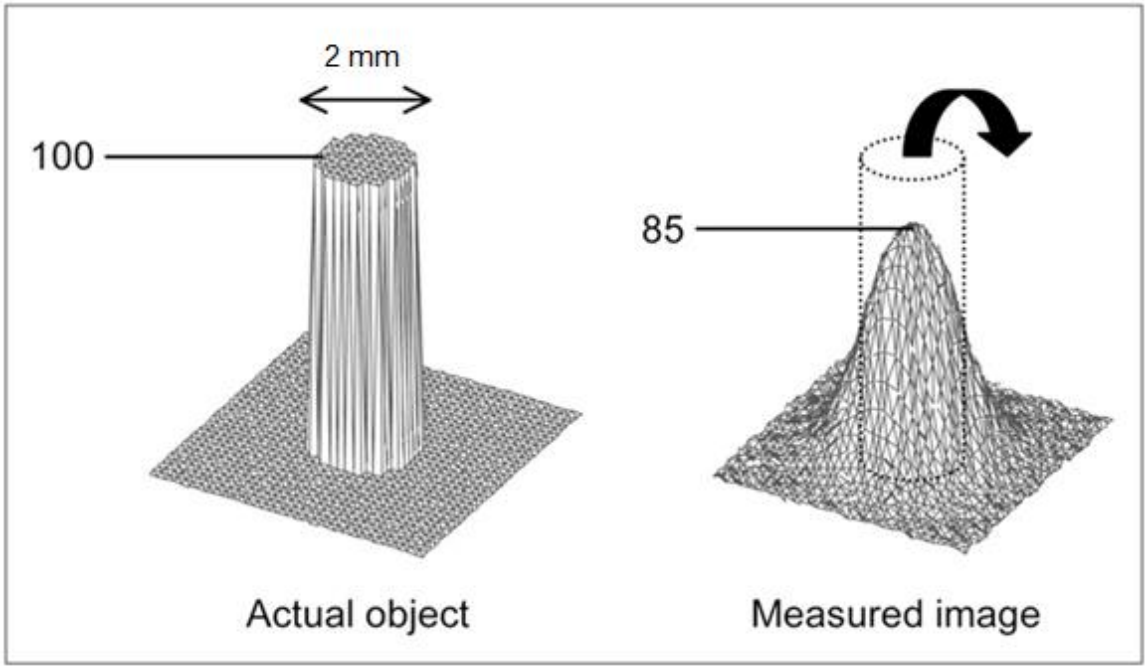

Figure 39: A source with 2 mm diameter of uniform intensity (100 arbitrary units) give a measured image in which part of signal is seen outside actual source. Note that the intensity of measured image is reduced to 85 (Soret et al 2007).

PVE depends mainly on the source size and shape, spatial resolution, image sampling, and the measurement method. This phenomenon not only is an issue in PET and SPECT but also of concern in high resolution imaging modalities like MRI and CT (Soret et al

2007). A number of methods have been used and proposed for accurate PVE quantification and correction in PET as presented for example by Soret et al 2007, Wells et al (2007). The simplest method for PVE correction is the use of a recovery coefficient (RC) which is defined as the ratio between apparent to true activity concentration (Sorenson and Phelps 1987). Basically, if the system has a known uniform spatial resolution and if the source size is known the RC pre-calculated correction factors (Hoffman et al 1979) as a function of source size and for different system resolution can be used to correct for the PVE underestimation of concentration for small source size. For instance, for a 2 mm source diameter imaged by a 5 mm spatial resolution system the RC would be 0.35; therefore the measured activity would have to by multiply the RC factor to obtain the PVE corrected value. The PVE is a source of image distortion that results in a loss of image contrast due to the error in estimating the regional source activity concentration (Hoffman et al 1979).

c.) Number of angular views effects

Theoretically, the sampling requirement placed in terms of detector spatial resolution requires the linear sampling distance across each projection to be $d \leq FWHM/3$. The linear sampling distance sets a resolution limit for any imaging system (Sorenson and Phelps 1987). Improper sampling can result in an image distortion and reduction of spatial resolution. Therefore, the FWHM is a function of the linear sampling distance (d). In emission tomography, the number of angular views obtained across the projections field of view (D) taken over 180° detector position is given by (26) (Sorenson and Phelps 1987):

$$number\ of\ angular\ views = \frac{\pi\, D}{2\, d} \qquad \textbf{(26)}$$

(26) shows that the linear sampling distance and, hence, the FWHM is inversely proportional to the number of angular views. In other words, as the number of views increase the FWHM value decrease. Extending the effect of angular sampling intervals to Compton camera images acquired from multiple views; it is rational that as the number of views increase the spatial resolution improves. Decreasing the number of views will results in an image artifacts due to image under sampling. A study of the effect of the number of angular views on the spatial resolution of the camera is given in Table 16 the FWHM values quoted are for a 2 mm Cs^{137} source placed at 3 cm from the camera face.

Number of views	FWHM (mm)
1	6.9
4	5.7
8	4.9

Table 16: Variation of spatial resolution with the number of camera views.

The results in Table 16 show that the spatial resolution improves with increasing the number of angular views until reaching the detector resolution limit. For instance, the FWHM will improve by 14% with using four angular views compared to one angular view.

3.2.3.3 **Deconvoluted point source image**

As described in section (3.2.3.2) the reconstructed point source image is distorted by the system response, this distortion is characterized by the system PSF. The PSF can be used to improve the image quality by using the deconvolution technique. Deconvolution is a key area of image processing used to de-blur and remove the instrument degradation function which is described by the PSF (Starck et al 2002). Thus, provides a

straightforward way to moderate the effect of instrument noise and improves the image of the point source. Figure 40(b) shows a deconvolved point source image. The deconvolution was done using the "iterative deconvolution" plugin in ImageJ (National Institutes of Health 2005).

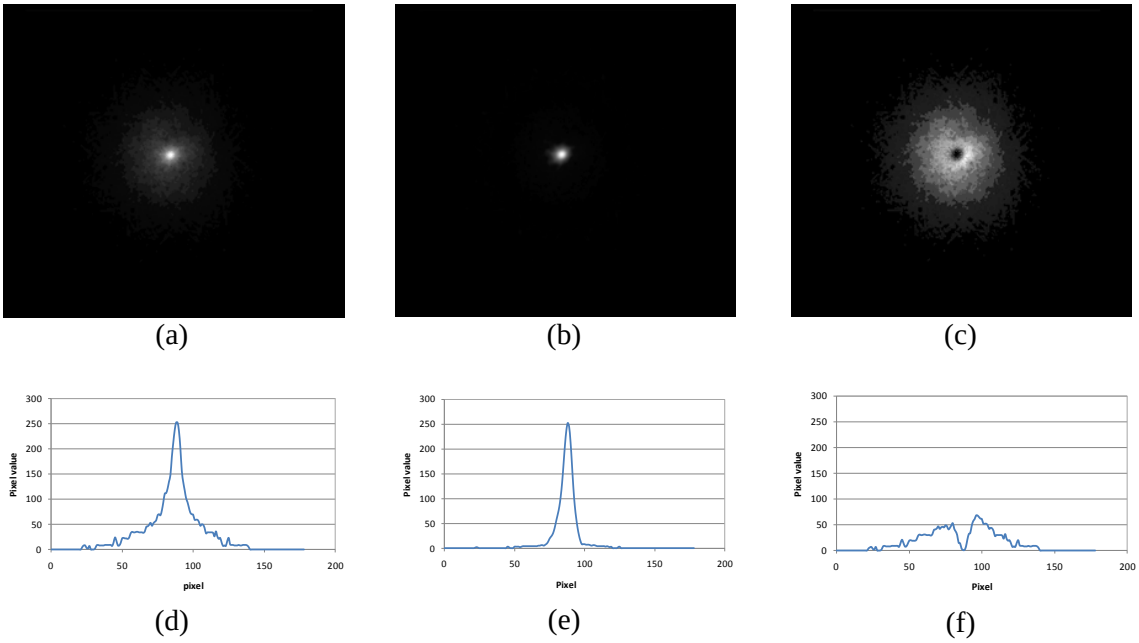

Figure 40: The original backprojected point source image (a) the Deconvoluted point (b) and the difference image(c) along with the line profile taken through each image.

The result in Figure 40 is a simple example of the use of deconvolution to estimate accurately the source distribution and remove the noise in the image as indicated by the suppression of line profile tails in Figure 40 (e) compared to (d) which is shown in the difference between them in Figure 40 (f). If we consider an image characterized by its intensity distribution (I) corresponding to the source real data distribution(S) removed by imaging system. If the imaging system is linear the relation between the data and the image is a convolution given by the following (27):

$$I_{(x,y)} = (P * S)_{(x,y)} + N_{(x,y)} \quad \textbf{(27)}$$

Where P is the point spread function and N is the additive system noise. From (27), if I and P are known the real source distribution $S_{(x,y)}$ can be determined by solving the inverse problem i.e. deconvolution. This method was used successfully in astronomical and nuclear medicine studies to create better image. For instance, Starck et al (2002) used the deconvolution technique to extract scientific content from astronomical images. In addition, Shao and Karp (1991) used a scattering deconvolution method to accurately estimate the scatter fraction in SPECT images by modelling the scattering point source function. Further work is needed to implement a deconvolution algorithm to the reconstructed data for different source distributions by accurately modelling the system response.

3.2.4 Distance dependence

The spatial resolution of the Compton camera images is a function of the distance between the source and the front detector and to demonstrate this concept a Cs^{137} point source was imaged at different distance from the camera front surface with the same acquisition time. The image profile FWHM (mm) was measured for each position and the results is plotted as FWHM (mm) versus distance (cm) from the front detector as seen in Figure 41. This experiment was carried out with limited pixel geometry.

The linear equation of the Figure 41 can be used to indicate the expected FWHM values at different distance. The FWHM of the spatial spread (S_{FWHM}) at a distance D from the front detector is given by (Singh 1983):

$$S_{FWHM} = D \ \tan \Delta\theta \qquad \textbf{(28)}$$

Where $\Delta\theta$ is the angular resolution of the system which can be computed from the quadratic addition in (2). According to Singh's formula ((28)) the spatial resolution of the system is distance dependent. The results in Figure 41 showed that the FWHM is directly proportional to the distance of the source which aggresses with the theoretical expectations. From Figure 41 slope equation the FWHM increased by 0.35 mm for each centimetre of distance. Thus, the geometrical contribution to the angular uncertainty increase with distance as discussed in (section 3.2.2.2).

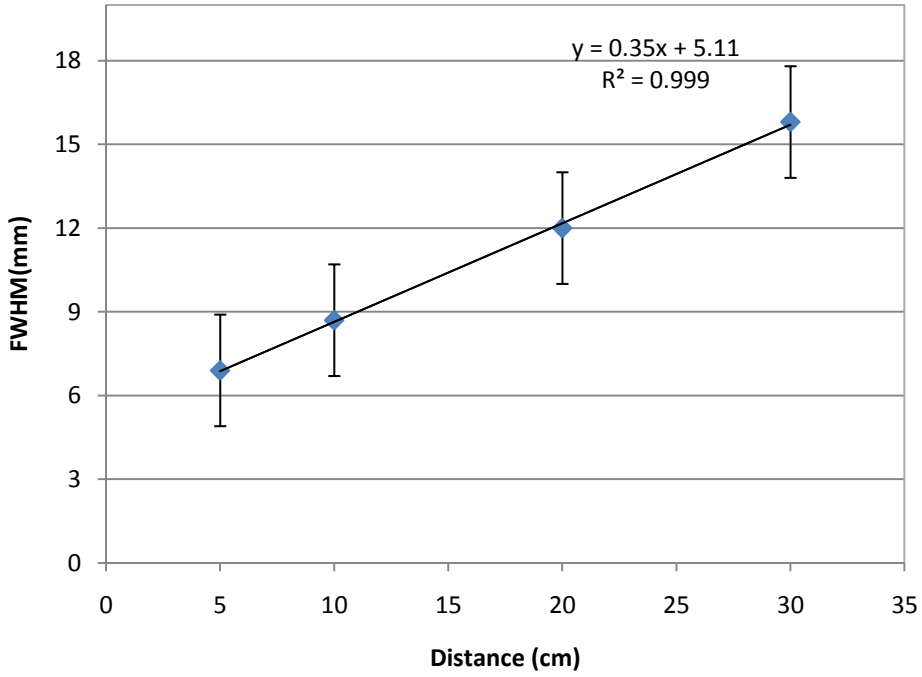

Figure 41: PSF (mm) vs. distance from the front detector (cm), the error bars was obtained by taking the uncertainty of the mean FWHM values which is 2mm. The large error bar is mainly due to the fact that the measurements were taken from the front of the cryostat outer surface rather than the front detector. The R^2 suggests a good fit.

The graph equation shows that the FWHM value (*y*-intercept) will be 5.11 mm if the source is attached to the front camera surface i.e. the distance *x* is replaced by zero, however, the source was placed in front of the cryostat outer surface rather than the front

detector due to the camera design, thus, the source is actually placed at ~ 13.3 mm from the camera front detector, see figure 9 in page 56, adding an additional contribution to the geometrical effect on angular resolution as described by equation 29. Substituting S_{FWHM} by 5.11 mm and the distance D by 13.3 mm results in an angular uncertainty of 10º.

The results indicate that the blurring effect will increase for deep imaged structure within the imaged object, for instance if the source is located at 20 cm from the detector the image FWHM (mm) will be reduced by a factor of 2 compared to a source located at 5 cm. This effect can be compensated by directly incorporate it in the reconstruction algorithm as mentioned by Tashiro et al. (2010) which presented a technique to compensate for this effect with SPECT images. This technique can accurately compensate for the distance-dependent detector response. By modelling the detector point spread function as a 2D Gaussian function whose width is dependent on the source-to-detector distance, a spatially variant inverse filter can be computed and applied to the set of all sinogram slices.

3.2.5 Efficiency

The efficiency of Compton camera was determined by dividing the number of events selected as coincidence (useful events) by the number of photons emitted from the source. For a 3.7 MBq (Cs^{137}) point source placed at 5 cm from the camera front surface. The number of coincident events collected ~ 15,500 events which were acquired over 15 hours. This can be translated 0.27 events per second. In addition, the number of 662 keV gamma-ray photons emitted by Cs^{137} which is 0.935 was taken into consideration. Thus, the intrinsic efficiency of Compton camera is the absolute efficiency multiplied by the geometry factor as calculated from the following formula (J. B Martin et al 1993):

$$\varepsilon = \frac{useful\ events}{emitted\ events} \times \frac{\Omega}{4\pi}$$

(29)

Where Ω is the solid angle calculated by dividing the detector surface area by the source to detector distance squared) subtended by the front detector which is limited to 0.5 sterradian in the current camera limited pixel geometry. The measured intrinsic efficiency of the camera with the current limited pixel geometry is 3.0×10^{-10} for 662 keV source energy.

The detection efficiency for the experimental measured efficiency is lower than theoretically estimated efficiency (in section 2.9.2) by four orders of magnitude due to the limited number of pixels (31 pixels) currently read out. Possible other reasons of this large difference are the poor triggering performance, data filtering and reconstruction decoding penalty, timing resolution issues, and the dead time effects which were not taken into account in the theoretically estimated efficiency.

3.2.6 Timing properties

3.2.6.1 **Time resolution**

In any timing measurement the generation of a logic pulse that indicates the occurrence time of an input pulse always involve some degree of uncertainty (Knoll 1999). This timing inaccuracy can be divided into two categories: random fluctuations in the signal pulse size and shape which is called time jitter and amplitude walk which is derived mainly from the variable amplitude of input pulses. The overall timing uncertainty in the measurement system can be estimated by measuring the full width at half maximum (FWHM) of the time distribution which is called the time resolution (Knoll 1999). The

minimum usable time window width is typically defined by the FWHM of the timing spectrum (J. W. Leblanc et al 1999).

After a gamma ray interaction in the detector the signal from the detector preamplifier split into two signals. The cathode signal is digitized in the ADC and then used for MWD energy determination .The anode signal is fed into a timing filter amplifier (TFA) and a constant fraction discriminator (CFD) for timing measurement as described in (section 2.2.2). The TFA has a constant decay time fixed at 50 us, 250ns rise and shaping time, and decimation 2.

The system timing resolution was measured by taking the FWHM value for the coincidence-timing spectrum shown in Figure 42. The spectrum in Figure 42 represents the number of coincidence events collected versus the ADC bins (12.5ns each). The measured system electronic time resolution is ~ 70 ns.

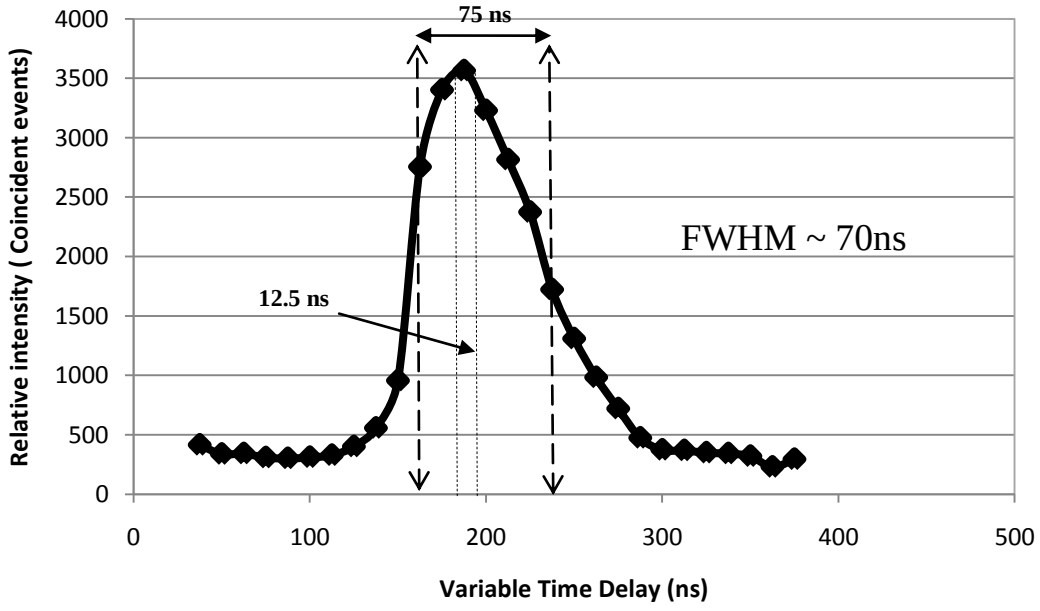

Figure 42: coincident counts collected as a function of channel number. Time window with 75 and 12.5 ns width were projected on the time axis

From Figure 42 it can be seen that 75 ns coincidence time window is sufficient to pass most of true coincidence events i.e. area under the peak. Figure 42 shows that if a narrow time window e.g. 12.5 ns is projected on the time axis it will yields about 18% of the area under the time peak due to the finite timing resolution. Nevertheless, using narrow time window improves the image quality, due to the improved true/random events ratio and reduce the statistical noise in the reconstructed image as described in (section 3.2.6.2) at the expense of sensitivity. The reduction of noise variance factor (f) in PET images is given by (Moses et al 2010):

$$f = \frac{2D}{c\,\Delta t} \qquad \textbf{(30)}$$

Where D is the imaged object diameter, c is the speed of light, and Δt is the time resolution. From (30), the noise variance can be improved and increase the SNR by improving the system timing resolution. The time resolution is affected by several factors related with different component of the detection system. The intrinsic characteristic of the detector crystal, namely the rise and decay time, is the main factor that limits the time resolution (Maurizio Conti 2009). Faster rise and decay time improve the time resolution. Another factor that limits the time resolution is the readout electronics. When the signal is fed into the readout electronics for time triggering and stamping the time jitter and amplitude walk from the electronics component degrades the time resolution of the system (Maurizio Conti 2009). Commercially available state of the art PET (LSO) scanners have achieved 0.5 ns timing resolution (Moses et al 2010). Therefore, optimising the time pick-off (triggering) method to minimise the degree of timing inaccuracy is needed to improve the system time resolution. Improving the timing resolution will enable higher true/random ratio to be collected without sacrificing the sensitivity.

3.2.6.2 **Time window width vs. image quality**

The main advantage of improving the coincidence timing is the reduced random event and eventually improves the image quality. Form (24) (section 3.1.2) the random event is a proportional to the time window. To demonstrate this concept a Cs^{137} point source image was reconstructed with different time window width (12.5 to 100 ns) and the results are shown in Table 17. The narrowest time window attainable with the current readout electronics is 12.5 ns as described in (section 2.2).

Time window (ns)	SNR	Counts
12.5	3.92	1445
25	3.42	5133
50	3.12	6630
75	2.94	7948
100	2.69	9004

Table 17: The time window widths (ns) vs. the SNR and the number of counts collected. The standard error was taken for the result. The standard error (± 0.2) was taken for the SNR.

The results in Table 17 show that the SNR improves linearly with decreasing the time window width due to the improved true/random events ratio. However, the number of coincidence counts and thus the sensitivity decrease with narrowing the time window as shown in Table 17 due to the rejection of many valid true events. The SNR was plotted versus the time window as shown in Figure 43.

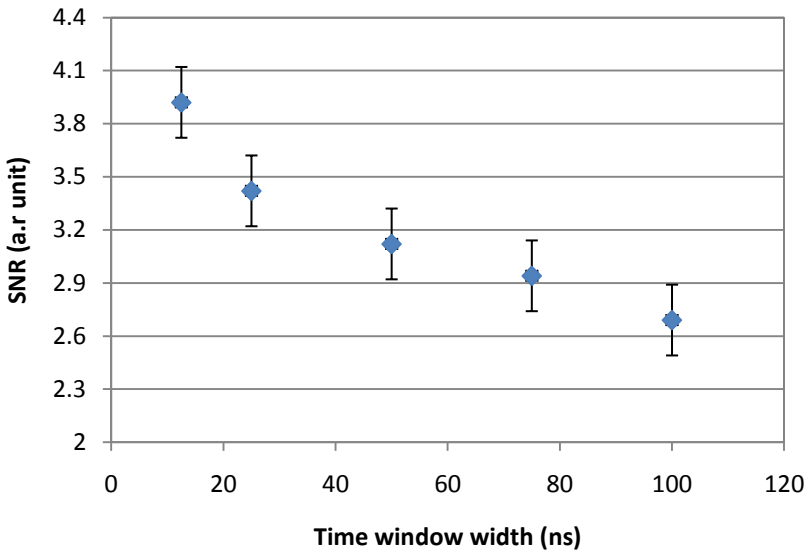

Figure 43: SNR (arbitrary unit) for different time window widths (ns)

Figure 43 shows that the signal-to-noise ratio improves with narrowing the time window width which indicates that the true/random events has increase as expected theoretically by Moses (2003). To achieve high efficiency of true rate the coincidence window width is usually set to twice the coincident timing resolution (Moses 2003).

3.2.6.3 **CFD parameter optimization**

As mentioned in (section 2.2.2) the CFD is a time pick-off method which uses a constant fraction of the input pulse to precisely determine the timing of the output pulse relative to the input signal. The CFD is supposed to provide output whenever the voltage of the input pulse is above the programmable threshold which was set to 9 mV as recommended by the GRT4 developer Lazarus (2004) to initiate triggering. The selection of the CFD threshold set is important to differentiate good signals from noisy signals because the MWD's baseline control is always triggered by the CFD (refer to section 2.2.1).

Therefore, the effect of threshold setting was investigated by imaging a 662 keV point source with different CFD thresholds under the same experiment setup. The threshold setting was varied from 4.5 mV to 10.5 mV by 1 mV step. The smallest threshold value

used is 4.5 mV; below this discriminator level the system dead time becomes prohibitive due to the electronics noise and the system has stopped giving outputs. Table 18, below, summarizes the results obtained with varying the CFD threshold level. The images reconstructed with different threshold levels are shown in Figure 45.

Threshold voltage (mV)	Energy threshold (keV)	Count $_{total}$	SNR
4.5	29.0	4304	3.2
5.5	35.5	4193	3.5
6.5	41.9	3500	3.9
7.5	48.4	3091	4.1
8.5	54.8	2833	4.2
9.5	61.3	2400	4.3
10.5	67.7	2104	4.3

Table 18: summary of the total count and SNR for different CFD threshold levels, the threshold voltage can be converted to threshold energy since 9 mV equals 60 keV (Lazarus 2004).

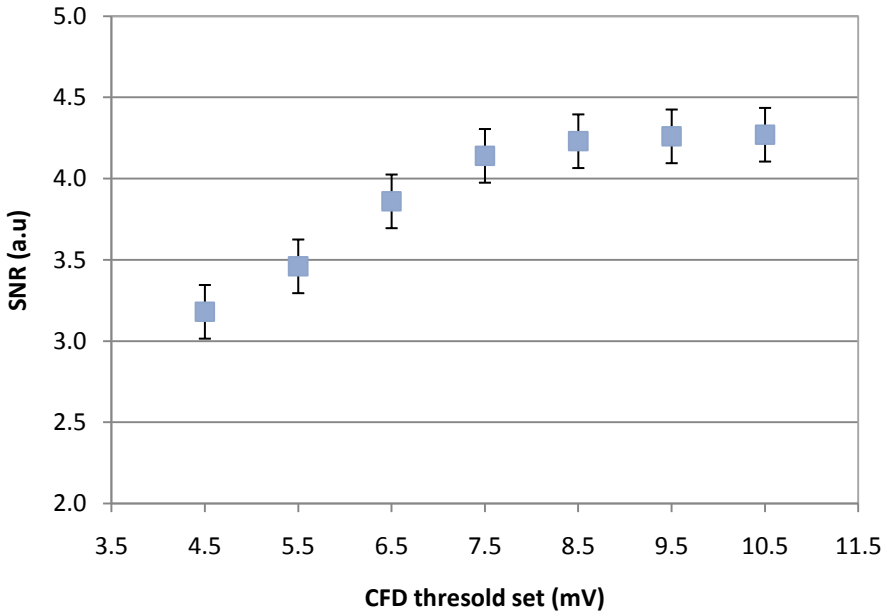

Figure 44: The SNR obtained with different CFD values. The error bars was obtained by taking the standard error of the mean value.

The results in Figure 44 showed that the SNR deteriorate with decreasing the threshold level below 7.5 mV. Changing the threshold amplitude above 7.5 mV has virtually no effect on the behavior of CFD and on the image quality as shown in Figure 44. This is due to the fact that with high threshold level the input pulses will be limited to a very narrow range in amplitude, however, with low thresholds pulses of different amplitudes are processed which add additional contribution of timing inaccuracy (time walk and jitter) and worsen the time resolution (Knoll 1999).

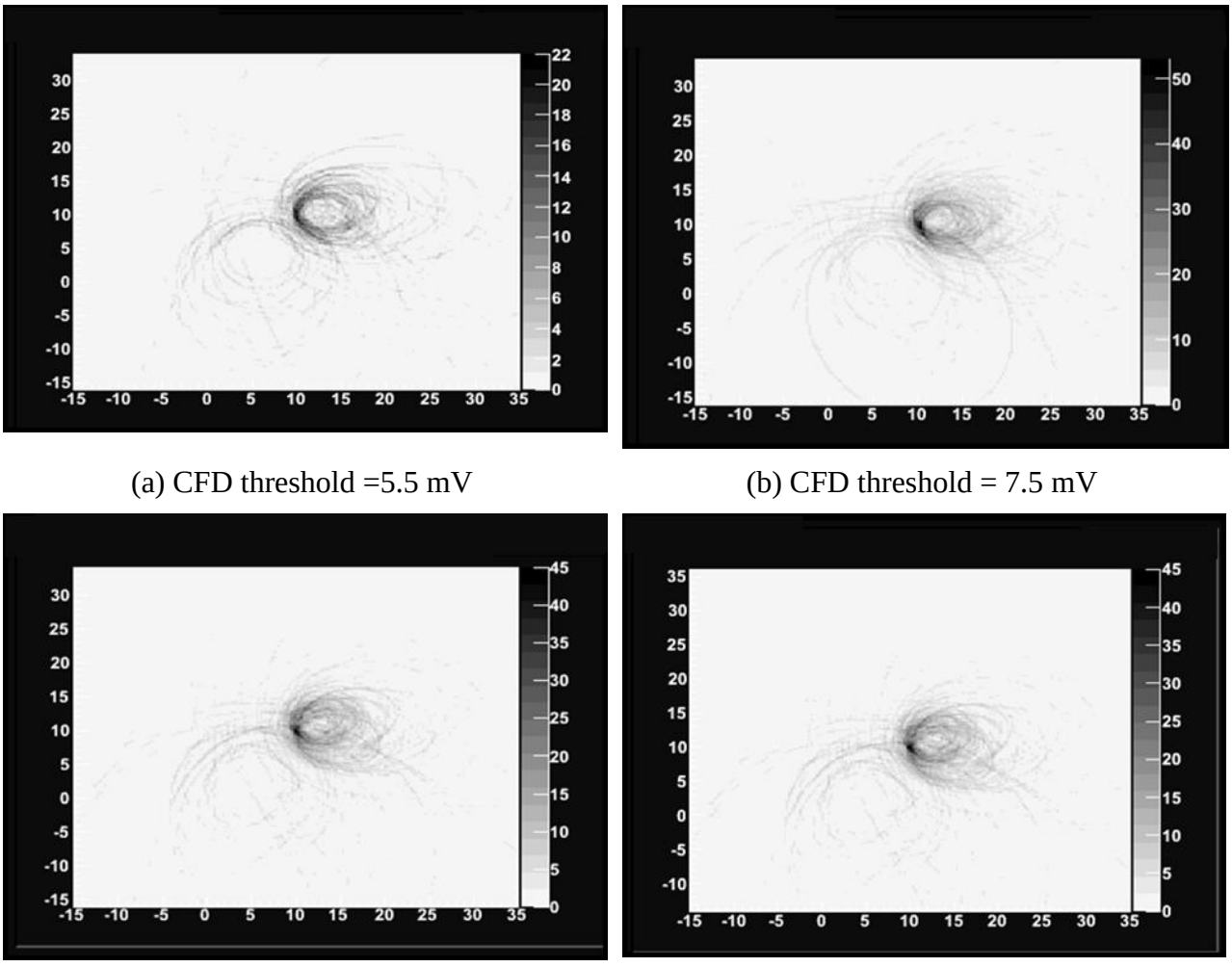

(a) CFD threshold =5.5 mV (b) CFD threshold = 7.5 mV

(c) CFD threshold =9.5 mV (d) CFD threshold = 10.5 mV

Figure 45: images reconstructed with different CFD discriminator levels.

As can be seen in Figure 45 (a) and (b) that the images acquired with low CFD threshold value have a distorted point source shape which is explained by the increase background, noise. This is because at small threshold level the CFD is not able to discriminate between low amplitude genuine and background pulses (Knoll 1999).

Whereas, using higher CFD threshold levels as in Figure 45 (c) and (d) clears the images from background noise, but, at the expense of sensitivity as shown the reduction of the total counts collected with increasing threshold level in Table 18. The degradation of image quality with low thresholds is mainly due to the statistical fluctuations in the number of charge carriers that makes up the signal which is greater for small amplitude pulses. Therefore, setting the threshold to 7.5mV can compromise between the sensitivity and image quality.

3.2.7 Counting limitation

The count rate performance of the system is limited by the relatively slow readout electronics as reflected by the poor timing resolution discussed in (section 3.2.6.1). Under high incident photons flux or with increasing the number of active pixels bottle neck behaviour in the data output pipe was observed as will be discussed in the following paragraphs.

Since the MIDAS data acquisition software does not provide the experiment count rate to the user, the data transfer rate (DTR) which is the speed at which the acquired data is transmitted to the data storage tape was used instead as an indicator of the counting performance.

3.2.7.1 **Effect of activating more pixels**

a.) In the back detector

The geometrical efficiency of the camera is a function of the detector area i.e. the solid angle available to the source as discussed in (section 1.7.2.2). Thus, the count rate is expected to increase linearly with increasing the number of detector pixels. To demonstrate this concept, the data rate was measured with varying the number of pixels used in the front and back detectors as shown in Figure 46 and Figure 47. The graph in Figure 46 shows the data rate (Mbytes/sec) versus the number of back pixels used (from 2 to 25 pixels) to trigger the 27 front pixels.

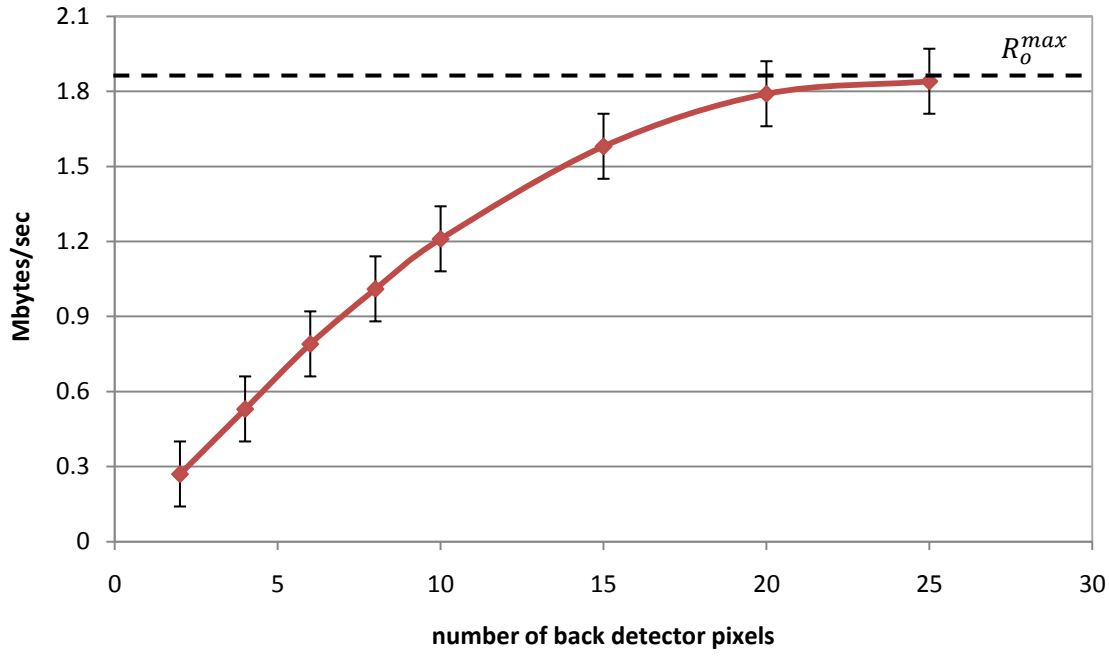

Figure 46: DTR vs. the number of back pixels used to trigger the front. The error bars represents the standard errors.

The results in Figure 46 show that the system have a non-paralyzable behaviour and the data rate is a function of the number of the back detector pixels used to trigger the front pixels. The observed DTR display a linear dependence on the number of pixels used in

the back detector before saturation. With using more than 15 pixels the measured data rate saturate at 1.85 Mbytes/sec as shown in Figure 46. The maximum count rate value R_o^{max} for a non-paralyzable system is given by (Sorenson and Phelps 1987):

$$R_o^{max} = {}^{1}/_{\tau} \quad \textbf{(31)}$$

Where (τ) is the system dead-time that is defined as the length of time required for the counting system to process and records an event during which the system will be busy and cannot rerecord additional events (Knoll 1999). From Figure 46 it can be noticed that the maximum data rate is ~ 1.85 Mbytes/sec which translates to 31 counts per second according to Lazarus et al (2004). Thus, from the maximum count rate the dead time is calculated by replacing R_o^{max} by 31 cps. The estimated system dead time is 32 milliseconds. Theoretically, according to Knoll (1999) the effective dead time can be viewed as half the system clock frequency (1/2 *f*) which is 40 MHz (i.e. τ = 25 millisecond). The discrepancy between theoretical and calculated dead time might be due to the instruments resolving time and pulse pile-up effect which was not taken in considerations in the theoretical estimation.

b.) In the front detector

The effect of increasing the front detector pixels on the DTR is shown in Figure 47. The back detector pixels were fixed in this experiment to only 4 pixels with increasing the number of front pixels from 8 to 27 pixels. The results in Figure 47 show that the data rate increase linearly with the number of the front pixels used due to the increase area of the detector available to the source.

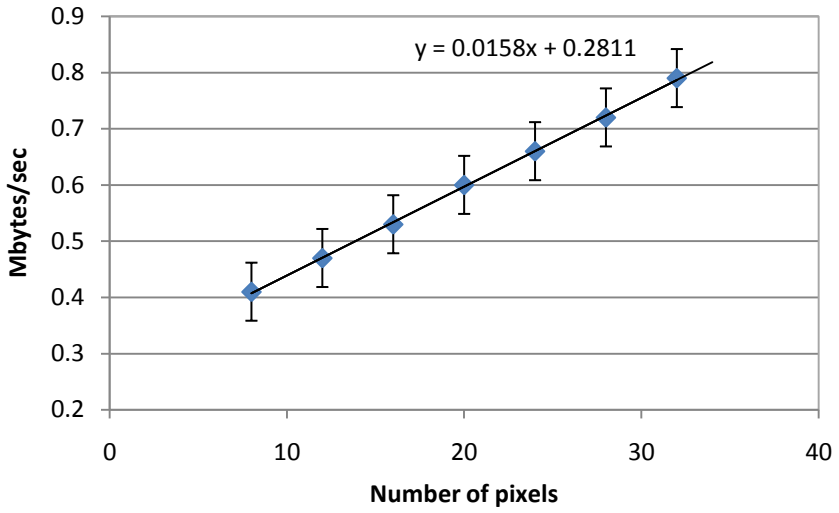

Figure 47: Front pixels used with fixing the back pixels to 4 pixels vs. DTR (Mbytes/sec). The error bars are the standard errors.

Since the DTR saturates at ~ 1.85 Mbytes/sec, then from the slope equation in Figure 47 if the y intercept is replaced by 1.8 Mbytes/second then the x intercept will be 100. Thus, the estimated number of front detector pixels that can be used with the current system counting capabilities is 100 i.e. ~ five pixels clusters. The results show that the counting performance has strong dependence on the number of back pixels compared to the front pixels due to the fact that the back pixels are used to initiate triggering and readout sequences as described in (section2.2.2).

3.2.7.2 **Effects of photons flux**

To study the behaviour of the system with different photon flux the camera was irradiated with different source activities form a fixed position. The incident flux Φ is defined as the number of photons per second per unit area of the detector as given by (32):

$$\Phi = \frac{Activity\ (Bq)}{Area(m^2)} \quad \textbf{(32)}$$

The activity in Bq is the number of photons/sec and the detector area in meter squared. The DTR is show in Figure 48 as a function of the incident photon flux. The results show that the observed DTR display a linear dependence on the incident flux before saturation. Under strong irradiation (flux > $6x10^{12}$ photon/sec/m^2) the measured data rate again saturate at ~ 1.85 Mbytes/sec. This indicates that high flux rate result in a multiple extension of the dead time period following an initial recorded count and the system hardly has time to finish one dead time period before starting another.

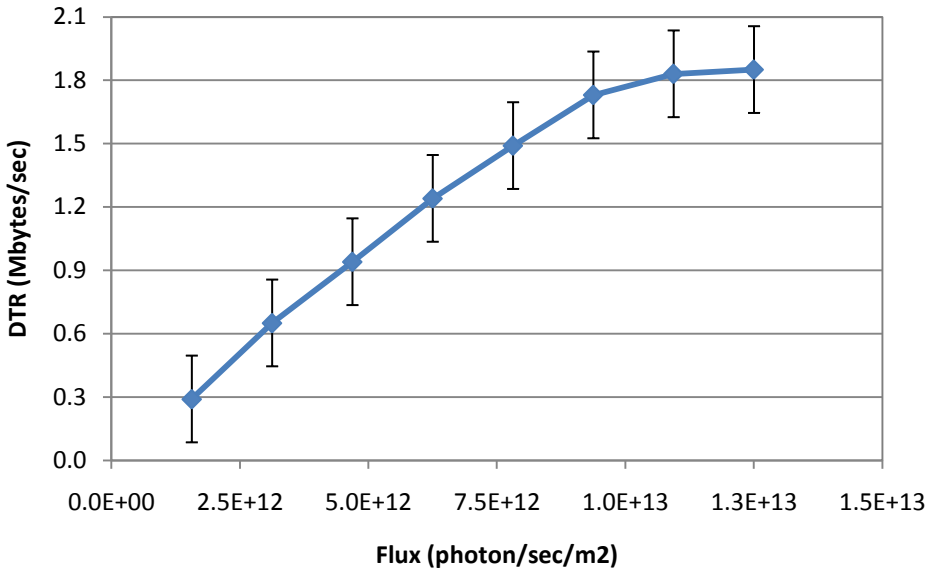

Figure 48: The DTR vs. the incident photons flux. The error bars represents the standard errors.

Figure 48 shows that high photons flux lead to count rate losses due to the system dead time as described in (section 3.2.7.1). Dead time count rate losses are given by the difference between the observed R_o and true count rate R_t, which is the count rate if τ =0, are given by (Sorenson and Phelps 1987):

$$count\ rate\ losses = \left[\frac{(R_t - R_o)}{R_t}\right] x\ 100\% \quad \textbf{(33)}$$

Many methods exist for dead-time correction as described by (Sorenson and Phelps 1987, Kang et al 2008, Chiesa et al 2009) that can be used to compensate for the count rate losses and improve the counting statistics to provide better quantitative accuracy.

3.3 Distributed source images

Objective and quantitative analysis of the system imaging performance that incorporate the combined effects of the basic measured system performance as well as the system processing and the quality of the reconstructed image is presented in this section. In addition the results of the multiple views imaging technique for line and ring source as well as a cylindrical phantom are presented in this section.

3.3.1 Cs^{137} Line source

To test the camera imaging performance with extended source a line source was imaged at 2 cm from the camera front surface by moving a Cs^{137}point source into 8 positions separated by 0.25cm to draw a line shape. The line source image shown in Figure 49 (a) was reconstructed with 16,000 from limited angle geometry as mentioned in (section 2.1).

Horizontal line profile has been taken through the centre of the line source image as shown in Figure 49. The FWHM values obtained are 7.2 ± 2mm. The profile distortion shown in Figure 49(b) is due to the backprojection artefacts which are caused by the ellipses associated with frequent combination of front and back pixels. The intensity is not equally distributed due to the geometrical consideration of sensitivity variation at different source position with the limited area occupied by the detector (Solomon and R J Ott 1988, Dedek et al 2009).

A correction factor can be applied to the image to compensate for the sensitivity variations by multiplying the pixels in the low camera sensitivity by 1.25, since there is

25% difference as indicated by the line profiles taken at different line positions as shown in Figure 49 (c, e, and f). The corrected line source image is shown in Figure 49(b). It is worth emphasising that this is a very simple demonstration of the effect of a correction and further work is needed for more accurate correction by modeling and calculating the relative efficiency at each pixel based upon distance from the source and the scatter angle.

The width of the reconstructed line has been determined at 3 different positions by taken a horizontal profiles at y= 12.25, 11.25 and 10.25 cm. The width of the profiles after the correction is consistent with the results obtained for the point source. The width of the profile gives very similar results after correction at all 3 positions (σ =0.1) compared to the profile width before correction (σ =0.5).

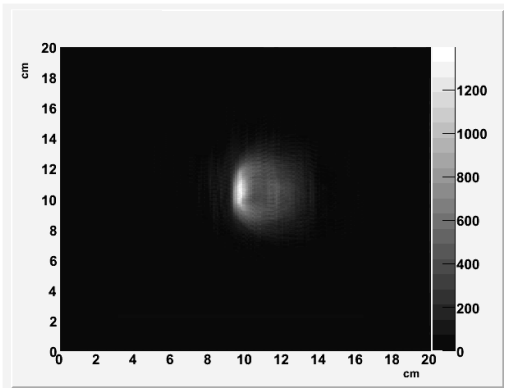

(a)

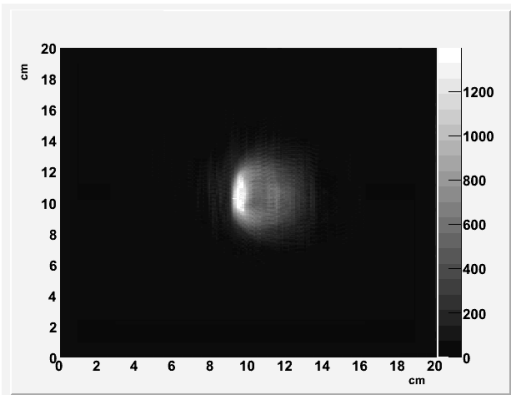

(b)

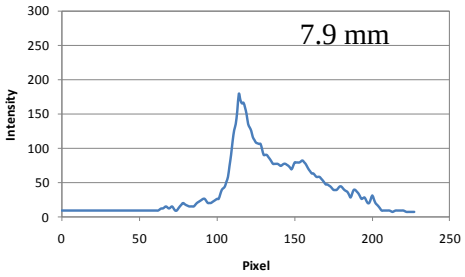

(c)

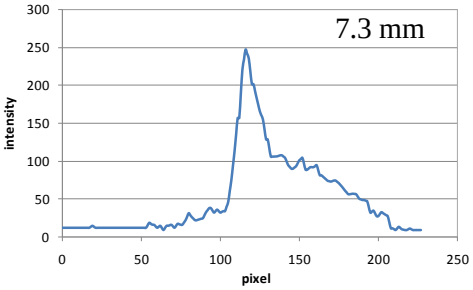

(d)

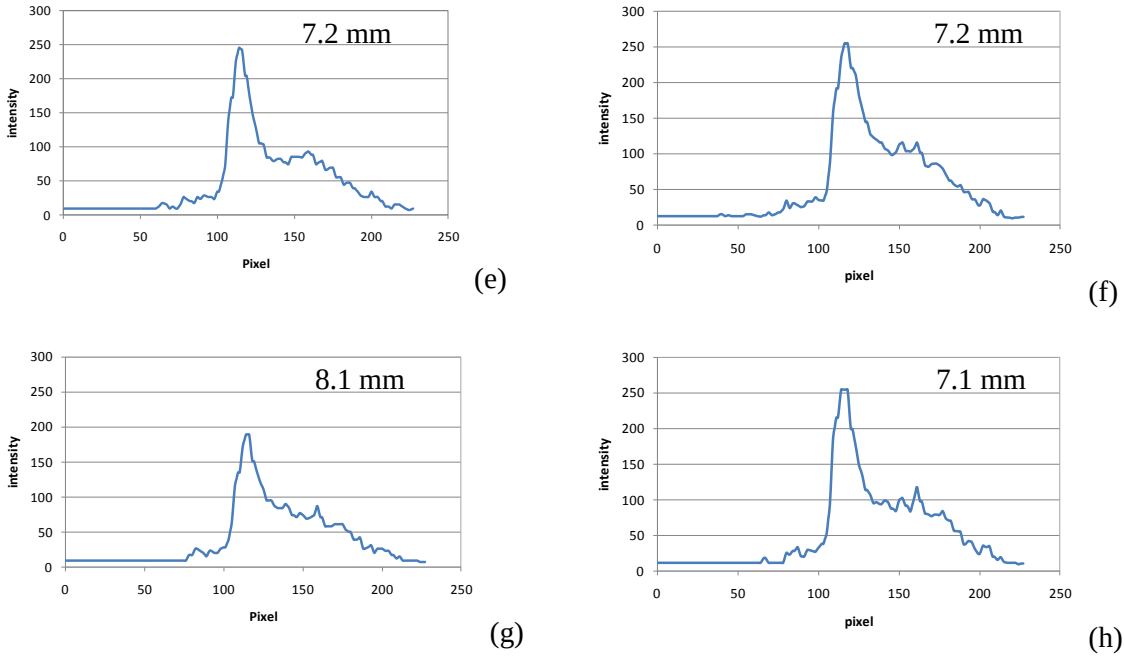

Figure 49 : Cs^{137} line source backprojected image(a) backprojected image with correction (c, e, and f) horizontal line profile at y= 12.25, 11.25 and 10.25 cm respectively for (a) and the same line profiles for (b) are presented in(d, g, and h)

3.3.2 Cs^{137} circular source

A circular source was imaged by moving the Cs^{137} source to draw a circular shape with 1.5 cm radius drawn by mounting a point source on a propeller attached to a motor as described in (section 2.4.2) and shown in Figure 18. The source was placed at 2cm from the camera front surface and 40,000 events were collected in 98 hours.

The pixels sensitivity variations with source position discussed in the previous section 3.3.1) resulted in a distorted incomplete circular shape compared to the actual source distribution (complete circle) as shown in Figure 50. This is because when the source rotates beneath the pixels the sensitivity will be higher compared to it when the source moves away from the pixels (M Alnaaimi et al 2010).

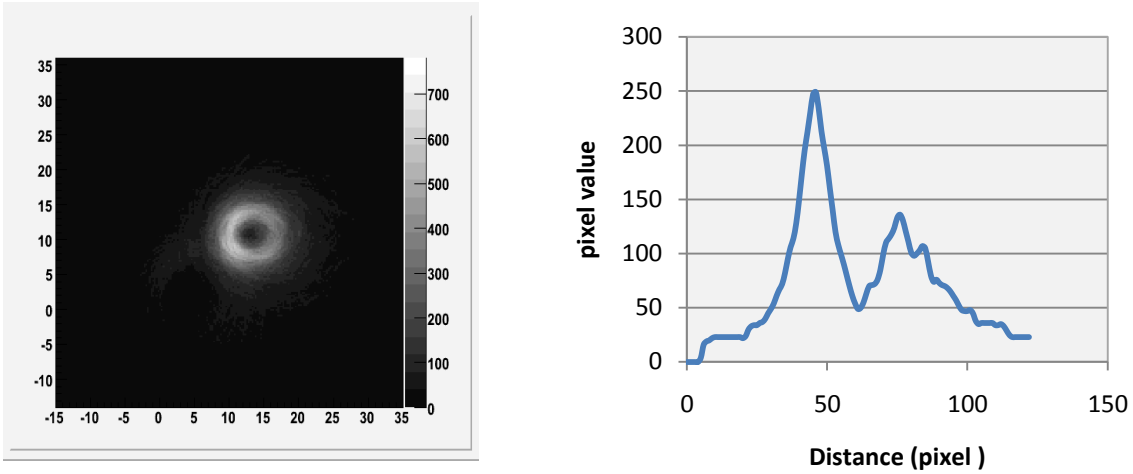

(a) **(b)**

Figure 50: circular source with 1.5 cm diameter reconstructed with backprojection (a) and its corresponding line profile (b).

The results in Figure 50 show that the Compton camera was successfully used to image extended sources. The images have been reconstructed at the expected position; however parts of the source distribution in the region of low camera sensitivity were not reconstructed accurately due to the sensitivity variation. As can be seen in the horizontal profile Figure 50 (b) that the sensitivity varies with source position, hence one prominent peak is seen instead of two peaks which correspond to the actual source distribution, i.e. the two peaks should have equal intensities.

To overcome this problem, a simple approach is to use a correction factor by multiplying the pixels at the low sensitivity area by 1.5 since there is 50% difference in the pixel values (intensity) as shown in Figure 50 profile peaks variation.

3.3.3 Ring source

Distributed ring shape source with different diameters were imaged with the same technique as mentioned in (section 2.3.6). The Cs^{137} point source was mounted on a rotating motor was mounted on a rotating platform and the rotating source was imaged from four equally spaced projection angles at 0°, 90°, 180°, and 270° at the camera central axis as shown in Figure 51.

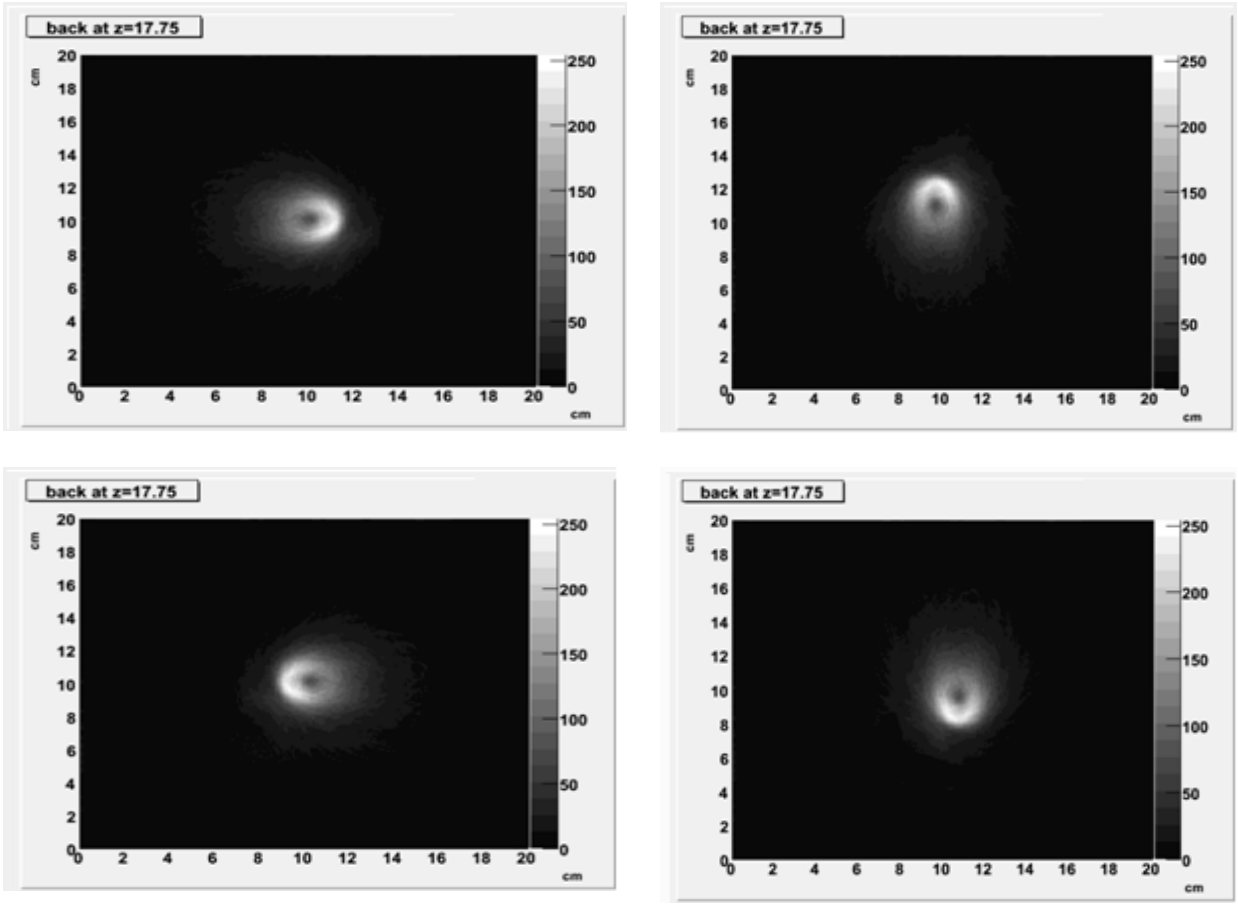

Figure 51: Multiple views for a circular source distribution acquired at 0,90,180, and 270 degrees from the camera central axis

In each position 15,000 coincident events were collected over 48 hours. The total acquisition time is 192 hours with total number of coincidence events equal to 60,000 in the superimposed summed image. The long acquisition time is mainly due to the limited area covered by the front detector pixels and the slow electronics. To improve the detector

efficiency i.e. reduce the scan time more pixels need to be activated in the front detector to cover larger area in conjunction with fast electronics are needed as discussed in section 2.3.10.2. The backprojection summed images for ring with different diameters are shown in Figure 52.

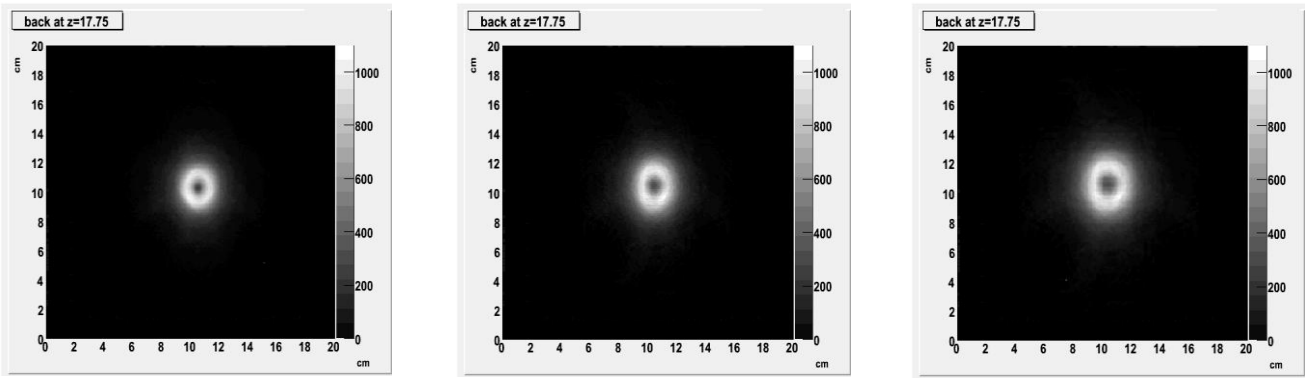

(a) **(b)** **(c)**

Figure 52: The summed image for a circular source with different diameters 1.5, 2, and 3 cm respectively.

The results in Figure 52 show the ability of this system to image distributed source activity. The expected ring position, shape and size were reconstructed successfully. Horizontal line profiles were taken through the center of each ring image in figure 9 and shown in Figure 53. Note that the multiple views technique overcomes the sensitivity variation problem mentioned in (section3.3.1).

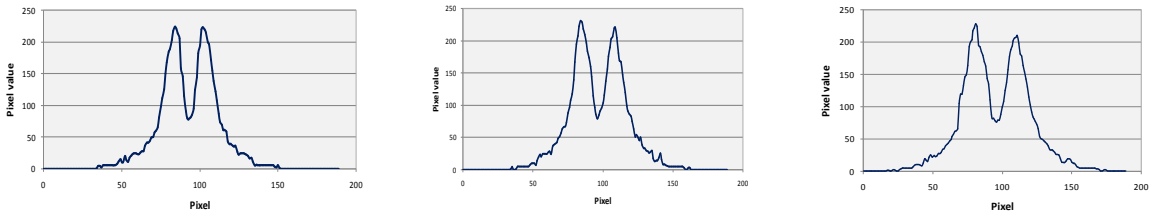

(a) (b) (c)

Figure 53: Line profiles taken through the center of the 1.5, 2, and 3 cm diameters ring image respectively.

The peaks separations in Figure 53 are 1.7, 2.2, and 2.8 ± 0.2 cm respectively. The error corresponds to one-half the pixel size (Singh 1983). The difference between true and measured separations is mainly due to the position uncertainty that leads to angular uncertainty and distort the reconstructed image (Du *et al* 2000).

The main source of position uncertainty as discussed in (section 2.3.10.1) is the size of the pixel and the finite range of the recoil electron in the detector crystal that determines the production of the charge carriers. In addition, the true ring diameter might be misestimated due to the rotating motor geometric positioning errors.

Another source of position uncertainty is the possible misalignment between the source and the pixel position due to the ambiguity in the exact actual pixels locations; small misalignment can cause large distortion in the reconstructed image (Du et al 2000). The SNR and contrast were calculated, as shown in Table 19.

Image	SNR	Contrast
Single view	1.6	0.67
Multiple view	2.5	0.72

Table 19: The SNR and Contrast for the single and multiple views images

An improvement in the SNR by 60% is observed with multiple views image compared to single view. The contrast improved in the multiple view by 7% compared to single view image. Again, this is due to the enhanced image sampling accuracy with the multiple-view imaging which results in a higher quality of reconstruction by reducing the effect of artefact.

3.4 Resolving power

The resolving power is the ability of an imaging device to measure the separation between two adjacent points. This method is a more precise way to measure the FWHM since the distance between the peaks of two curves from the profile histogram represents the known distance between the two points. The maximum profile counts (peak) represents the center of point source and the number of pixels separating the two peaks would be equivalent to the known distance.

The resolving power of the camera was investigated by imaging two Cs^{137} point sources separated by 3.5 mm. The two points are clearly separated and identified as two sources, as shown in figure 54. This image demonstrates Sorenson and Phelps (1987) assumption which states that the resolving power should be between FWHM/2 and FWHM/1.4. Since the FWHM of the system measured for a point source from a multiple view acquisition is 4.9 mm as discussed in (section 3.2.3.2) the resolving power for this system is expected to be 3.5 mm. In addition, the horizontal line profile taken through the two points showed two barely distinguishable peaks. The artefact caused by the reconstruction method resulted in overlapped peaks.

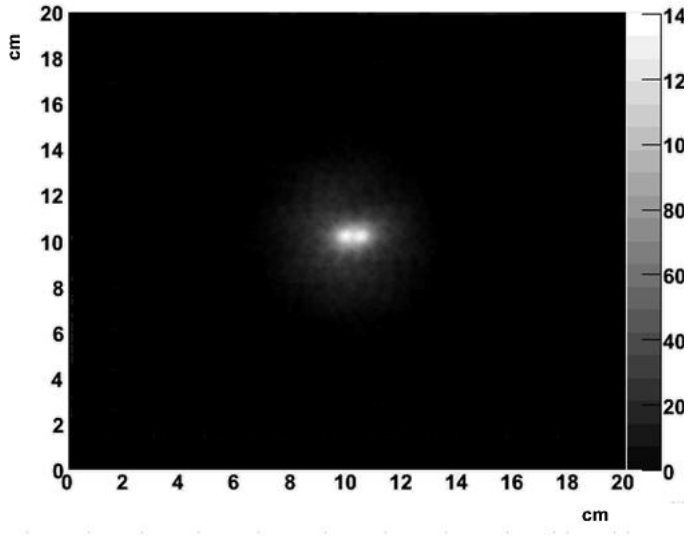

(a)

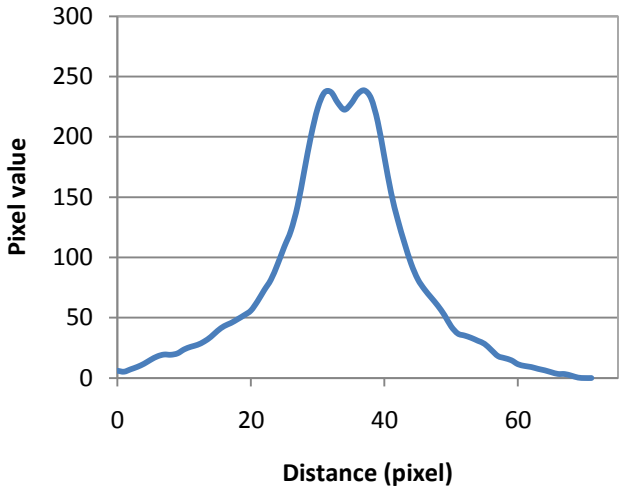

(b)

Figure 54: Two points separated by 3.5 mm backprojection image (a) and its corresponding profile (b).

3.5 Phantom images

The images in this section present the first images of Fluorine-18 and Iodine-131 obtained with the UCL prototype Compton camera. These two radioisotopes are of clinical interest and their physical properties are presented in (section 2.4.1).These images are expected to improve in the future systems with better detectors, electronics, and image reconstruction algorithms.

3.5.1 F^{18} triangles phantom imaging

The cylindrical Perspex phantom described in (section 2.4.3) was filled with water and each tube was filled with 20 MBq of F^{18} fluorodeoxyglucose (FDG). The phantom was placed 5 cm from the camera front detector. The phantom was imaged for 60 hours using four different projections (0°, 90°, 180° and 270°) as shown in Figure 55 and 28,000 events were collected. The UCL Compton camera system has been used to image 511 keV distributed sources for the first time. Figure 56 show the summed four views image reconstructed by simple backprojection. The expected phantom shape and insert locations were successfully reconstructed. Horizontal line profiles were taken through the top, middle, and bottom inserts are shown in Figure 57.

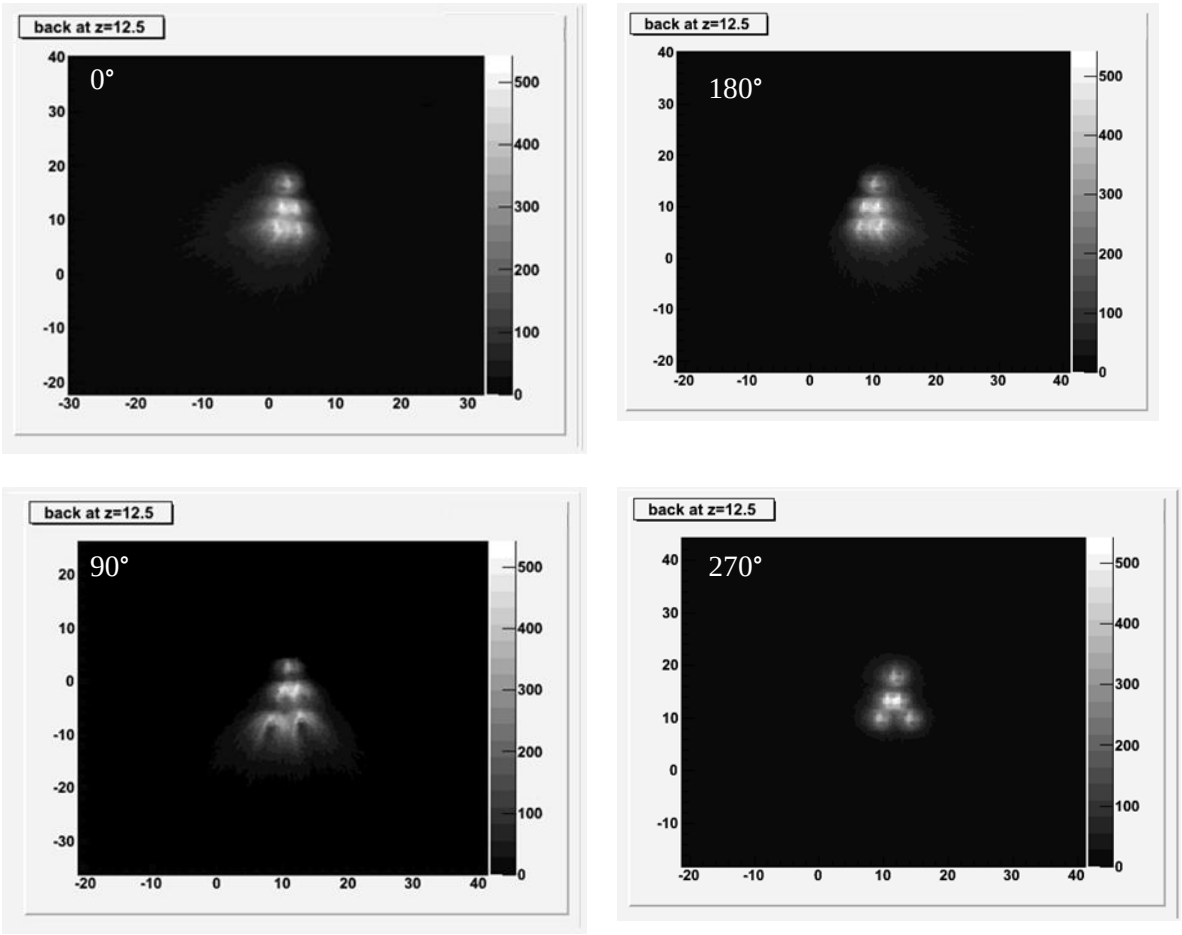

Figure 55: Multiple views for the phantom acquired at 0, 90,180, and 270 degrees from the camera central axis.

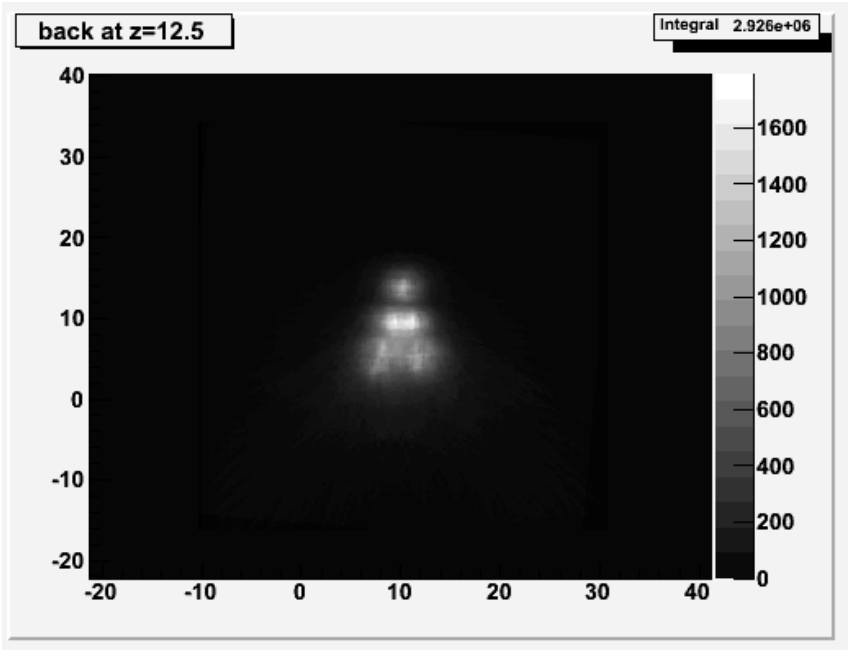

Figure 56: the 4 views backprojected summed image for the F^{18} triangles phantom

The results in Figure 55 and Figure 56 demonstrate the capability of this prototype Compton camera to image a distributed 511 keV source and resolve two F^{18} tubes separated by 2 cm. The nominal tubes position, shape and size were reconstructed as shown in Figure 56(a). The diameter of the F^{18} cylinders was 9 mm. The reconstruction artefacts are clearly present in each image and may be minimised through increased angular sampling as indicated by Table 16.

Figure 57 shows the horizontal line profiles taken through the center of each cylinder row in Figure 56. The FHWM for a single 9 mm diameter cylinder (Figure 57 a) is 3.3 ± 0.2 cm, where the error corresponds to one half of the pixel size (Singh 1983). The peak separations for profiles (b) and (c) in Figure 57 are 2.2 and 4.3 cm respectively. Note that the actual separations are 2 and 4 ± 0.1 cm respectively.

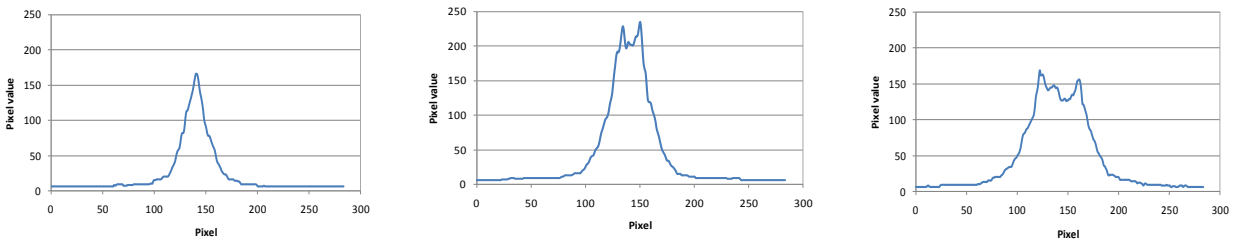

(a) (b) (c)

Figure 57: Line profiles taken through (a) the top row, (b) the middle row and (c) the bottom row.

The intensity of the inserts varies according to their position relative to the active front detector pixels due to the fact that the camera sensitivity varies with the source position, as mentioned by Dedek *et al* (2009). The middle row of inserts in Figure 56 shows a higher intensity than the other rows because they are positioned centrally over the active pixel cluster.

The line profile of the middle row of inserts shown in Figure 57(b) indicates that they have ~ 30% higher intensity compared to other rows. Therefore, a correction factor can be

applied for the top and bottom row of inserts to compensate for the intensity variations simply by multiplying each pixel value by 1.3 to increase their intensities by 30% as shown in Figure 59.

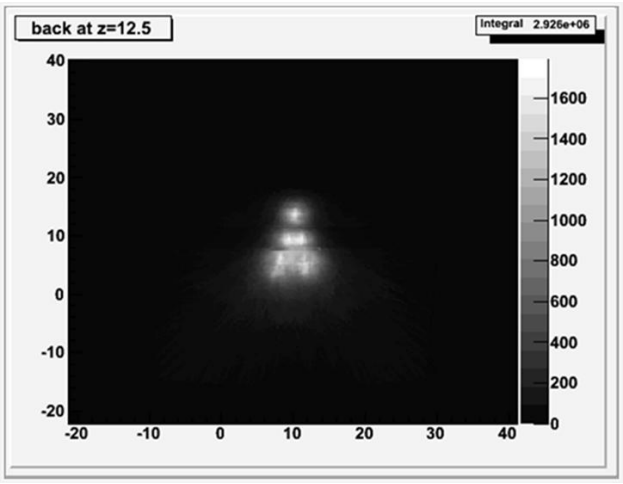

Figure 58: the F^{18} triangles phantom after applying a correction factor to the top and bottom rows. Note the recovered top and bottom intensity compared to Figure 56.

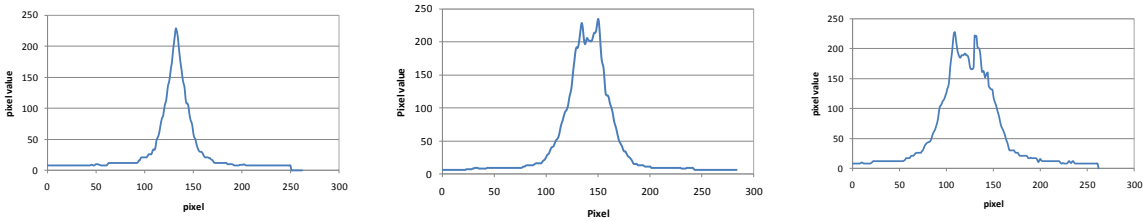

Figure 59: Line profiles taken through (a) the top row, (b) the middle row and (c) the bottom row with applying a correction factor for the top and bottom rows.

The profiles in Figure 59 (a) and (c) have similar intensity regardless of the inserts position relative to the active front detector pixels. Thus, the effect of sensitivity variations with source position on the image can be corrected by multiplying each pixel by the correction factor as shown in Figure 58.

The relative performance of Compton camera decreases with increasing the object size due to the fact that the signal from the central pixel is spatially multiplexed with the

signals from all other pixels, hence, the noise is propagated to the pixel of interest (Wernick and Aarsvold 2004). The dependency of object size can be noticed in this experiment (9 mm insert) compared to the 511 keV point source image presented in (section 3.2.3.1). This dependence of image noise on object diameter is also observed in tomographic imaging (Wernick and Aarsvold 2004).

3.5.2 I^{131} imaging

Iodine-131 radioisotope which is widely used in nuclear medicine for diagnosis and therapy was used in a various experiment setups and imaged with the UCL Compton camera for the first time. The physical properties of I^{131} is discussed in (section 2.4.1)

3.5.2.1 I^{131} triangle phantom images

A phantom study was carried out to investigate the imaging performance of the camera with a distributed 360 keV source. The triangles phantom shown in Figure 21 was used. Each tube was filled with 10 Mbq of I^{131} and the main phantom container was filled with normal water. The total acquisition time is 96 hours and the phantom was imaged from four equally spaced projection angles.

The summed image was reconstructed with 38,000 events as shown in Figure 60. Figure 60 demonstrates the ability of the Compton camera to image I^{131} distributed source. The nominal tubes positions were reconstructed with some degree of distortion (blur) in their shapes.

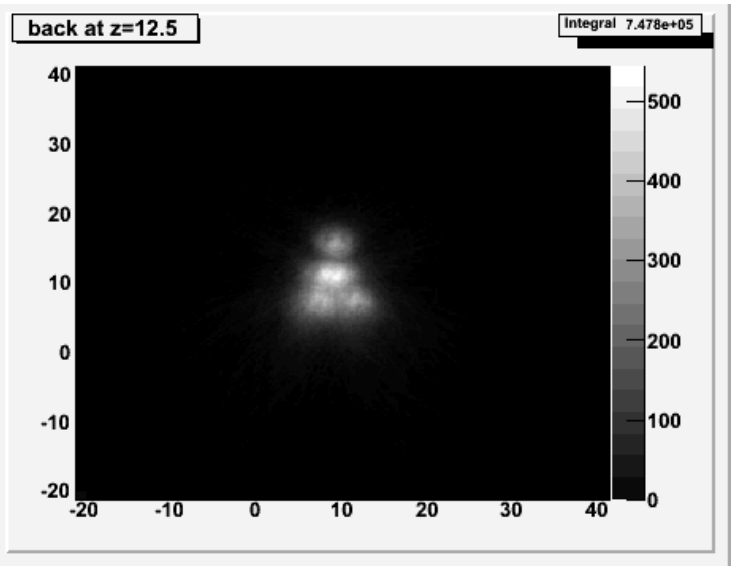

Figure 60: I131 triangle summed four views image.

As seen in Figure 60 it is difficult to separate between the tube (target) and background particularly for middle tubes. This is due to the scatter effect of the photons in water and the partial volume effect which is significant at 360 keV photon energies as a result of to the finite system spatial resolution (Dewaraja et al 2009). The partial volume effect leads to spill-out of counts from the target (tube) to the background (Dewaraja et al 2006), hence, decreases and underestimates the counts in the target as shown in Figure 61 (a) and (c). Again the intensity of the tubes varies with the position of the tubes relative to the active front detector pixels due to the fact that the camera sensitivity varies with the source position, however, this can be corrected by multiplying the pixels with a correction factor as shown in Figure 62 and discussed in (section 3.5.1). A method to compensate for the PVE is discussed in (section 3.2.3.2)

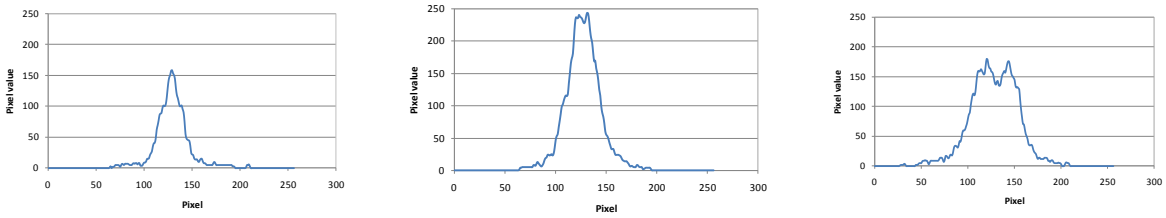

(a) (b) (c)

Figure 61: Line profiles taken through (a) the top row, (b) the middle row and (c) the bottom row.

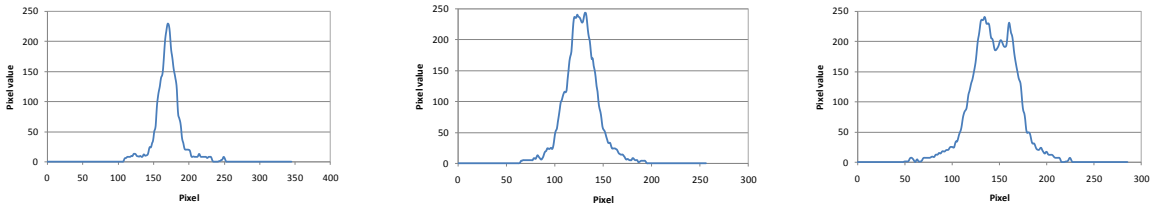

(a) (b) (c)

Figure 62: the corrected line profiles taken through (a) the top row, (b) the middle row and (c) the bottom row.

The FWHM value for the horizontal line profile taken through the centre of the top tube is 3.75 cm as shown in Figure 61(a) note that the actual tube diameter is 0.9 cm. The peaks separation for profile (b) and (c) in Figure 61 are 2.7 and 6.25 cm respectively. Note that the actual tubes separation is 2 and 4 cm for the middle and bottom tubes respectively. The profiles are noisy and the peaks are distorted due to the increased image noise particularly in the area separating the tubes.

The resolution degradation is mainly due to the effect of Doppler broadening which is considered as a limiting factor for 360 keV photons imaging (Han et al 2008) and results in an uncertainty in identifying the gamma-ray interaction position. Using (7), the contribution of Doppler broadening to the angular uncertainty was calculated for 360 keV and 662 keV gamma rays after a single Compton scattering by 45° in the front detector. The theoretical calculations of the angular uncertainty due to the Doppler broadening indicates that at 360 keV the effect of Doppler broadening on the angular uncertainty is a factor of 3 more than its effect at 662 keV source energy as discussed in (section 3.2.2.1).

This is due to the fact that part of the incident photon energy will be used to break the binding of struck electron to the atom and, hence, not all electron momentum states can results in Compton scattering of the low energy incident photon which consequently lead to a significant source of energy uncertainty (Ordonez et al 1997).

Despite the poor imaging performance of this prototype Compton camera with I^{131} phantom imaging, in principle the Compton camera is expected to be 20 times better than gamma camera for detecting 360 keV photons in the same acquisition time providing that an appropriate image reconstruction and data corrections are used (Han et al 2008).

3.5.2.2 I^{131} vial imaging

The I^{131} vial was positioned horizontally at 3 cm from the camera front surface as shown in Figure 19 and multiple views have been taken. In each projection the image was reconstructed with 5,900 events collected in each view over 12 hours. The final superimposed image was reconstructed with 47,000 events.

The summed image in water was reconstructed with 38,000 events collected over 96 hrs. Note the difference in the number of events collected for the vial in air imaged with the same acquisition time. This is mainly due to photon attenuation in water. A comparison between the I^{131} image acquired in air and water is presented in Figure 63.

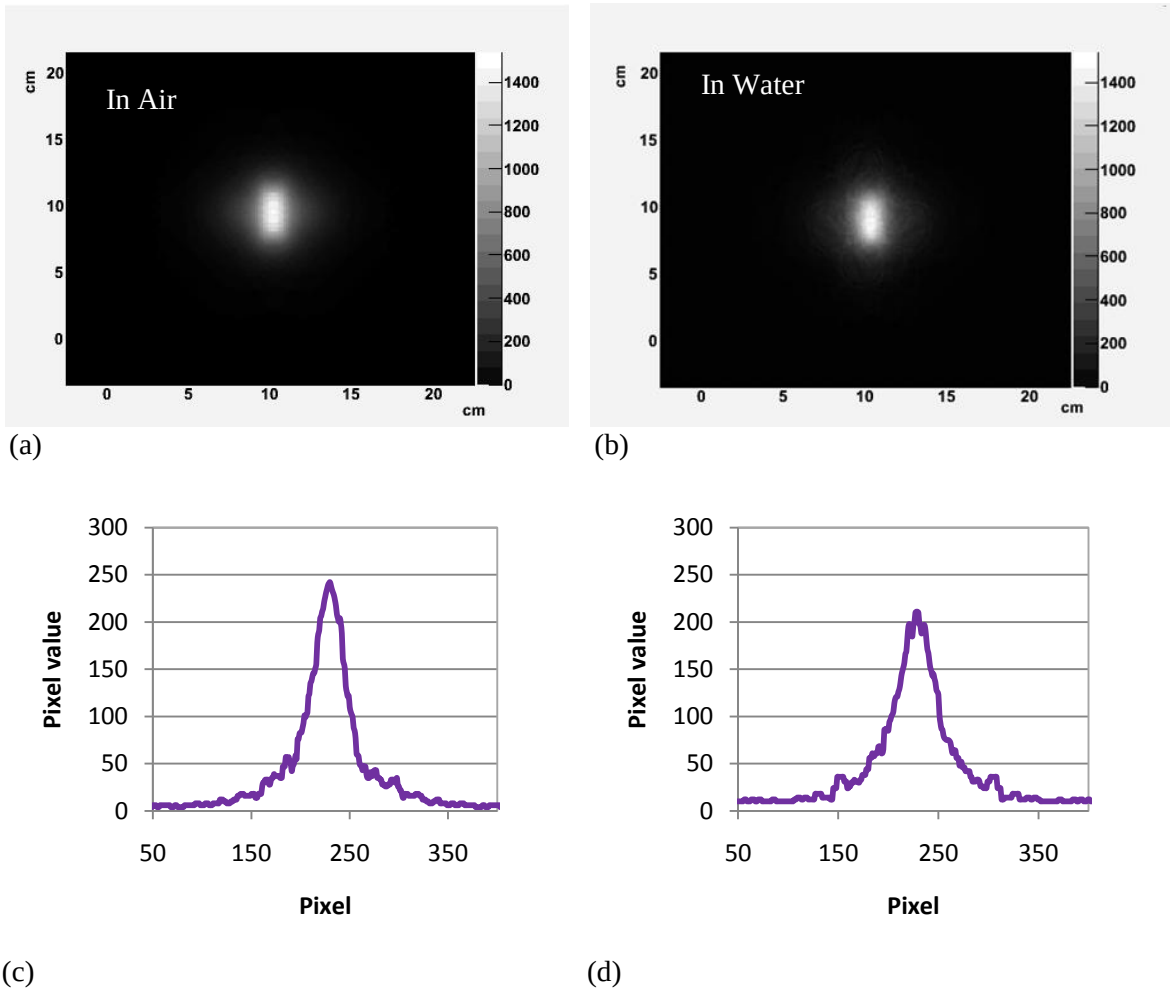

Figure 63: The vial image in air (a) water (b) with horizontal line profile through the centre of the image in air(c) and water (d)

The expected source shape and location were successfully reconstructed as shown in Figure 63. In Figure 63 (c) and (d) horizontal profiles have been taken through the centre of both images. The FWHM value is 42 and 44 mm for the vial in air and water respectively; note that the actual vial width is 20 mm. As mentioned earlier the resolution degradation at 360 keV imaging is mainly due to the effect of Doppler broadening on angular resolution (Han et al 2008). The image profiles have a uniform (1/r) blurring distribution as shown in Figure 63 (c) and (d). The results are summarised in Table 20. To quantify the difference between the two images the profile full width values at 66, 50, and 10% of the peak maximum value was measured as shown in Table 20.

	FW2/3M (mm)	FWHM (mm)	FWTM (mm)
Vial in air	22	42	135
Vial in water	31	44	163

Table 20: The horizontal profile FW2/3, FWHM, and FWTM values for the air and water vial images.

As shown in Table 20 that the FW2/3M values are close to the actual vial diameter (20mm) compared to the FWHM value. The FWTM value is high due to the background noise propagation. Theoretically, correcting the profile in Figure 63 (d) for attenuation is done by using the linear attenuation coefficient (μ) for 364 keV photons in water which is 0.11 cm^{-1} (Berger et al 1990). (34) is used to determine the average attenuation path length for each pixel (x) and a constant value (0.11 cm^{-1}) of the attenuation coefficient is used.

$$I = I_o e^{-\mu x} \quad \textbf{(34)}$$

From (34) it can be seen that the detected photon intensity represent 80% of the actual source activity. The apparent activity of the source is underestimated by 20% due to photon attenuation which matches the reduction in pixel intensity in Figure 63 (d). Note that (34) does not take into accounts the effect of random events in the reconstructed image which is influenced by the presence of scattering material and is another source of image distortion as discussed in section 3.1.2.

Table 20 and Figure 63 (d) show the broadening of the profile as well as suppression in peak intensity due to photons attenuation in water. Normalizing of the FWTM in water by that in air shows the effect of the scattering medium on the profile widening (van Lingen et al 1992). From Table 20 the FWTM water/air ratio is 1.20 which indicates 20% difference and matches the theoretical estimations of (34), and hence a correction factor

can be used to correct this issue as discussed in section (3.3.1).The SNR and contrast were measured for both images as shown in Table 21.

Image	SNR	Contrast
Multiple view (air)	4.0	0.77
Multiple view (water)	3.3	0.61

Table 21: The SNR and contrast for image in air and water.

Table 21 shows that the photons scattered in water resulted in decreasing the SNR by 17% and contrast by 20% compared to the image in air. Therefore, attenuation corrections need to be applied to I^{131} images to improve the quantitative efficiency of the camera.

3.5.2.3 I^{131} Disk shape source

The same vial was positioned and imaged vertically to reproduce a 2 cm cylinder shape source imaged in air and water as shown in Figure 20 with the same acquisition time and experiment setup mentioned in the previous section. The image in air was reconstructed with 42,000 events and the image in water with 34,000 events. The images along with horizontal line profiles are shown in Figure 64and a quantitative analysis of the images is shown in Table 22.

As shown in Figure 64 the expected source shape and location was reconstructed. As shown in Figure 64 (b) the disk image is blurred compared to Figure 64 (a) due to the expected increase in image noise from scattered photons. This noise propagates among all of the pixels along the cone produced in the backprojection processes. Again, with 360 keV source the Doppler broadening affects the resolution of the Compton camera images as mentioned discussed in (section 3.5.2.2)

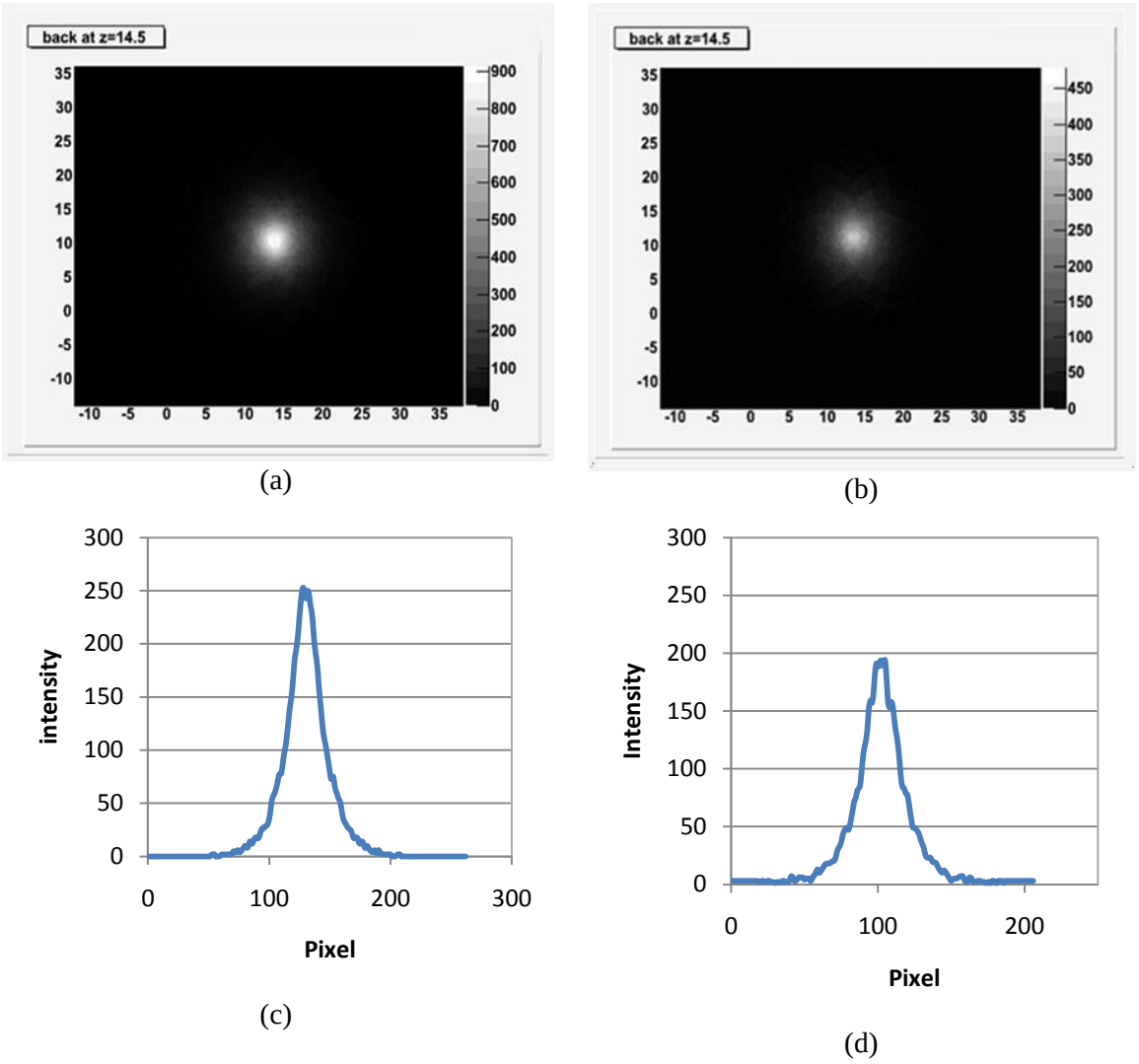

Figure 64: The disk shape image in air (a) water (b) with horizontal line profile through the centre of the image in air(c) and water (d)

Image	SNR	Contrast	FWTM(mm)
Multiple view (air)	2.5	0.47	68
Multiple view (water)	1.9	0.45	84

Table 22: The FWHM, signal to noise ratio and contrast for the I131 image in air compared to water.

The effect of photon attenuation in water degrades the SNR by ~ 25% and the contrast by ~ 5% compared to the image acquired in air as shown in Table 22. The image in Figure

64 (b) shows a suppression of counts especially at the centre of the image as can be seen in the reduced count profile intensity Figure 64 (d).

The fraction of the gamma ray beam attenuated in 2 cm of water was calculated by the photons survival probability in (19). The theoretical estimation agrees with the observed ~ 20% reduction in the profile peak intensity Figure 64 (d) compared to peak intensity Figure 64(c). From Table 22 the FWTM water/air ratio is 1.23 which indicates 23% difference due to the increased background noise from the scattering medium. The FWTM water/air ratio has a good agreement with the theoretical estimations of (34). Again, a correction factor can be used to correct for the intensity variation.

3.6 Comparison with gamma camera and PET

This section presents a comparison between the imaging performance of the prototype Compton camera to a commercially available gamma and PET cameras. It is complicated to compare between a prototype Compton camera with a state-of-the-art gamma or PET system. The collimated camera images are a direct representation of the source distribution blurred by 1/r Gaussian like function. On the other hands, the raw images from the Compton camera is a superposition of conic sections that gives an indirect representation of the source distribution and give a point response function similar to a truncated 1/r function. Therefore, a reconstruction or decoding action is required to get a usable image (Wernick and Aarsvold 2004).

The images presented in this section were reconstructed with simple backprojection and routine corrections used for gamma and PET systems were disabled. It is worth mentioning that the reconstruction process amplifies image noise so that a simple

comparison does not predict the relative imaging performance accurately (Wernick and Aarsvold 2004). Thus, it is required to have an analytical method that is independent of the reconstruction method to compare the performance of the Compton camera with other systems.

3.6.1 PET images

A PET scanner (specifications mentioned in section 2.4.4) was used for the comparison to set a benchmark since it is used as the gold standard for 511 keV imaging (Saha 2010). Simple Back projection without filters, scatter correction, and uniformity correction was used to reconstruct the phantom images. The fused PET/CT and the PET images are shown in Figure 65. The count rate (True, random, and scatter) is shown in Table 23 for three minutes scanning time.

Event type	Count rate
True	201107 cps
Random	13601 cps
Scatter	35108 cps

Table 23: The true, random, and scatter count rates

From Table 23 the noise equivalent count rate (NECR) which is a parameter used to characterized image noise was calculated by using the following equation:

$$NECR = T^2/T+R+S \quad (35)$$

Where T, S, and R are the True, random, and scatter count rate respectively. The square root of the NECR is proportional to the signal-to-noise (SNR) ratio in the final reconstructed images and, therefore, serves as a good parameter to compare the

performances of different PET scanners (Saha 2010). From Table 23 and (35), the NECR equals 108 kcps and thus the expected SNR is 10.4 in the reconstructed image.

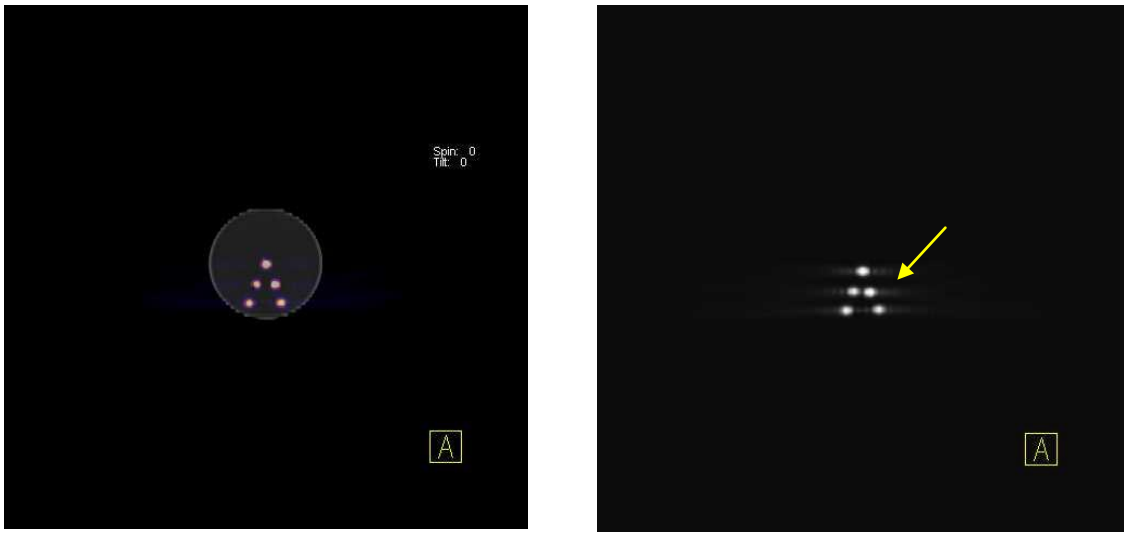

(a) Fused PET/CT (b) PET image

Figure 65: the triangles phantom fused PET/CT image (a) and PET image (b). The A letter inside the box is an indicator for the Anterior view

The PET image in Figure 65 (b) shows an artefact indicated by the arrow which results from the influence of the distributed counts among all pixels along the line of response (LOR) due to the absence of the reconstruction filters. Nevertheless, the line profiles taken through the top, middle and bottom rows as shown in Figure 66 indicate an excellent system response characterised by the 1.1 cm FHWM value for the 0.9 cm diameter cylinder (Figure 66).

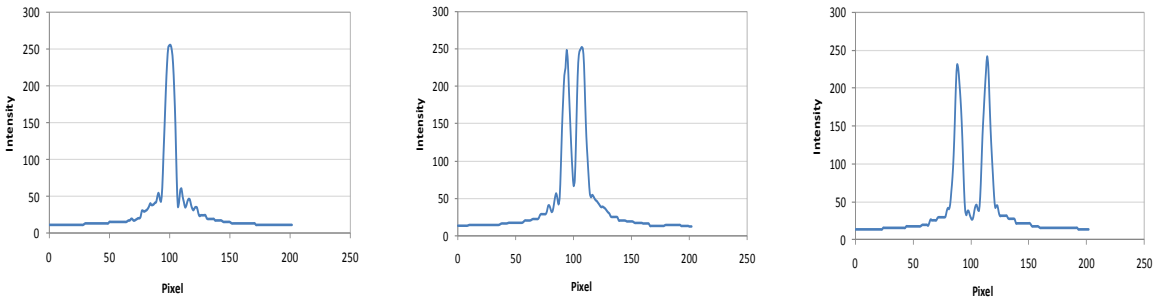

(a) (b) (c)

Figure 66: Line profiles taken through (a) the top row, (b) the middle row and (c) the bottom row.

The peak separations for profiles (b) and (c) in Figure 66 are 2.0 and 4.0 cm respectively which match the actual tubes separations. The intensity of the peaks in Figure 66 is the same which indicates consistent sensitivity of the PET camera unlike the prototype Compton camera sensitivity variations mentioned in (section 3.5.1). The small peaks seen in the profiles tail are due to the LOR artifact resulted from the absences of the reconstruction filters.

Figure 67 shows a comparison between Compton and PET camera for F^{18} triangle phantom imaging. Both images are reconstructed by simple backprojection. However, different backprojection algorithms were used for each image due to the difference in response function of each scanner. The backprojection algorithm used for Compton camera was developed by the UCL radiation physics group (section 2.3) and by Siemens Corporation for PET scanner. Therefore, different quality of image reconstruction is expected as shown in Figure 67.

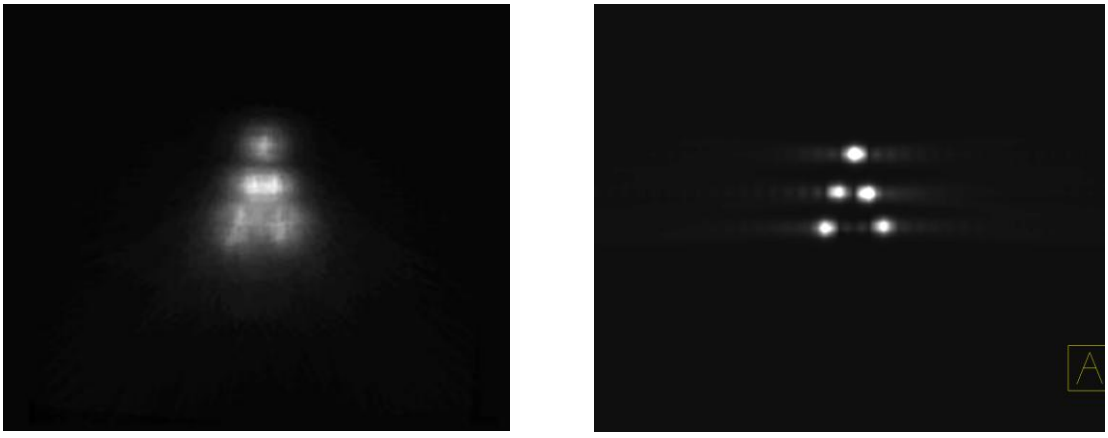

(a) (b)

Figure 67: the triangles phantom imaged with Compton camera (a) and PET (b)

Table 24 shows a quantitative comparison between Compton and PET camera for F^{18} imaging. The quantitative comparison presented in Table 24 shows that PET image has 4 times better SNR than Compton images along with an enhanced contrast. As shown in Figure 67, PET image qualitatively and quantitatively outperforms the Compton camera image at 511 keV imaging. The confounding influence of the image reconstruction algorithm used to for Compton camera is a key limitation. Eliminating this effect by implementing better reconstruction algorithm as discussed in section 2.3 could improve this comparison.

	Compton camera	PET
SNR	1.8	7.7
% Contrast	74	88

Table 24 : The measured SNR and % contrast for Compton camera and PET images

Although the comparison provides valuable information about the relative performance of the Compton camera compared to PET, the comparison has some limitation. Firstly, some corrections (attenuation and deadtime correction, sinogram uniformity, normalisation of PMT gains etc.) could not be disabled while acquiring the PET image, and hence, adds an advantage for PET over Compton camera image. Also, routine quality control tests are carried out regularly (daily or weekly) for PET scanner to ensure high quality of the images (Saha 2010). In addition, the angular sampling in PET is better than Compton camera since the detection area is bigger (64 detectors) i.e. 64 views compared to the limited number of views with the Compton camera. The backprojection algorithm used to reconstruct PET image is far more sophisticated than the crude reconstruction algorithm used for Compton camera images. Lastly, the images were reconstructed with different number of counts because the PET image was acquired with a list mode whole body scan

protocol by which the counts are received in series and saved as individual events as they occur.

Nevertheless, the Compton camera in principle can provide an alternative portable imaging system for 511 keV imaging. With an efficient image reconstruction algorithm the Compton camera can detect lesions as small as 4 mm as indicated by the theoretical estimations in (section 3.2.2). In addition, the expected sensitivity advantage of the Compton camera can potentially lead to a short scanning time and lower patient administered dose (Royle et al 2003).

3.6.2 Gamma camera planar images

This section compares the imaging performance of the conventional gamma camera (specifications mentioned in section 2.4.4) to the Compton camera for I^{131} imaging. The imaging performance of the gamma camera is determined mainly by the properties of the collimator as discussed in (section 1.2). The gamma camera planar image reconstructed with 38,000 counts is shown in Figure 68.

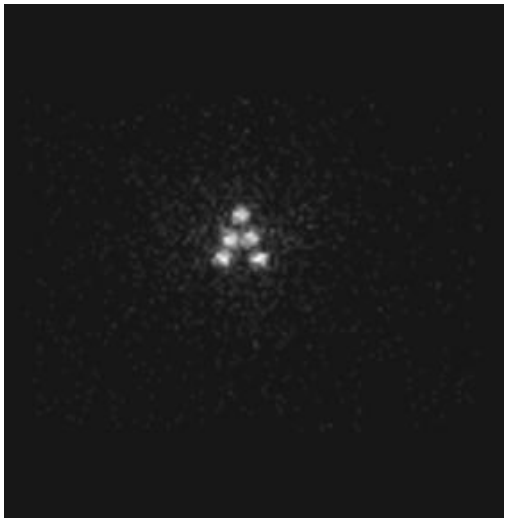

Figure 68: I^{131} planar gamma camera image reconstructed with 38,000 counts

The effect of collimator septal penetration due to the high energy of I^{131} can be observed in Figure 68 by the increased noise. Most of the photons detected from the I^{131} main energy peak are detected after septal penetration (Rault et al 2007). Septal penetration and scatter in the collimator results in degradation of spatial resolution and image blurring (Webb 1988). The horizontal line profiles taken through the top, middle and bottom rows are shown in Figure 69.

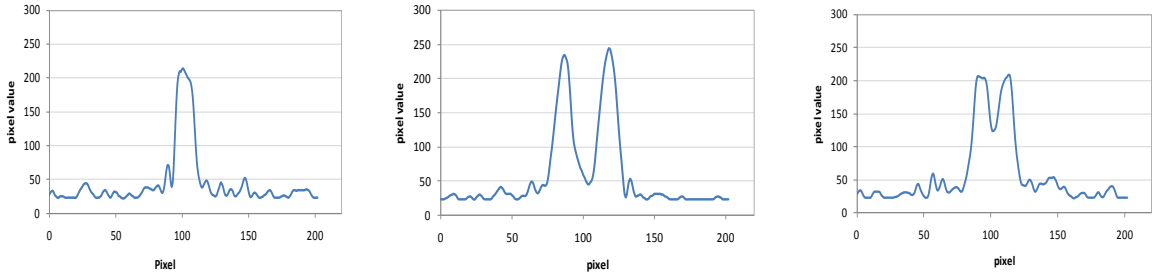

(a) (b) (c)

Figure 69: Line profiles taken through (a) the top row, (b) the middle row and (c) the bottom row.

The FHWM for a single 0.9 cm diameter cylinder (Figure 69 a) is 3.5 cm. The peak separations for profiles (b) and (c) in Figure 69 are 2.4 and 4.3 cm respectively which are close to the actual tubes separations. The results in Figure 69 demonstrate that for I^{131} imaging the gamma camera outperforms the Compton camera (section 3.5.2.1) when the same number of counts is used for reconstruction. This is mainly due to the effect of Doppler broadening on angular resolution at 360 keV and the confound influence of the image reconstruction algorithm used for Compton camera which has degraded the image quality. Likewise, Hua (2000) results showed that the gamma camera outperforms the Compton camera for equal detected counts.

However, the attractive aspect of Compton camera is that the sensitivity can increase without scarifying the resolution. Since the Compton camera is expected in principle to

have 20 times better sensitivity than gamma camera for detecting 360 keV photons in the same acquisition time (Han et al 2008), thus, the comparison should be done by comparing Compton image with 20 times more counts than gamma camera image. Using Han et al (2008) assumption the triangle phantom was imaged by gamma camera with 20 times less counts than Compton camera image and the images are shown in Figure 70. The gamma camera planar image was reconstructed with 1900 counts and the Compton image with 38,000 events (20 times more) as shown in Figure 70 (a) and (b). The FWHM of the horizontal line profile shown taken through the centre of the top row shown in Figure 70 (c) and (d) indicates that the Compton camera result in a limited improvement in the spatial resolution compared to gamma camera image which is mainly due to the crude reconstruction method used.

The gamma camera image in Figure 70 (b) is affected by photons that penetrate the septa and scatter in the collimator which resulted in degrading the FWHM as shown by the broadening of the line profile in Figure 70 (d). Table 25 shows a quantitative comparison between Compton and gamma camera in terms of the SNR and contrast.

	Compton camera	Gamma camera-Planar
SNR	2.4	1.2
% contrast	78	97

Table 25: The SNR and % contrast for Compton camera vs. gamma camera

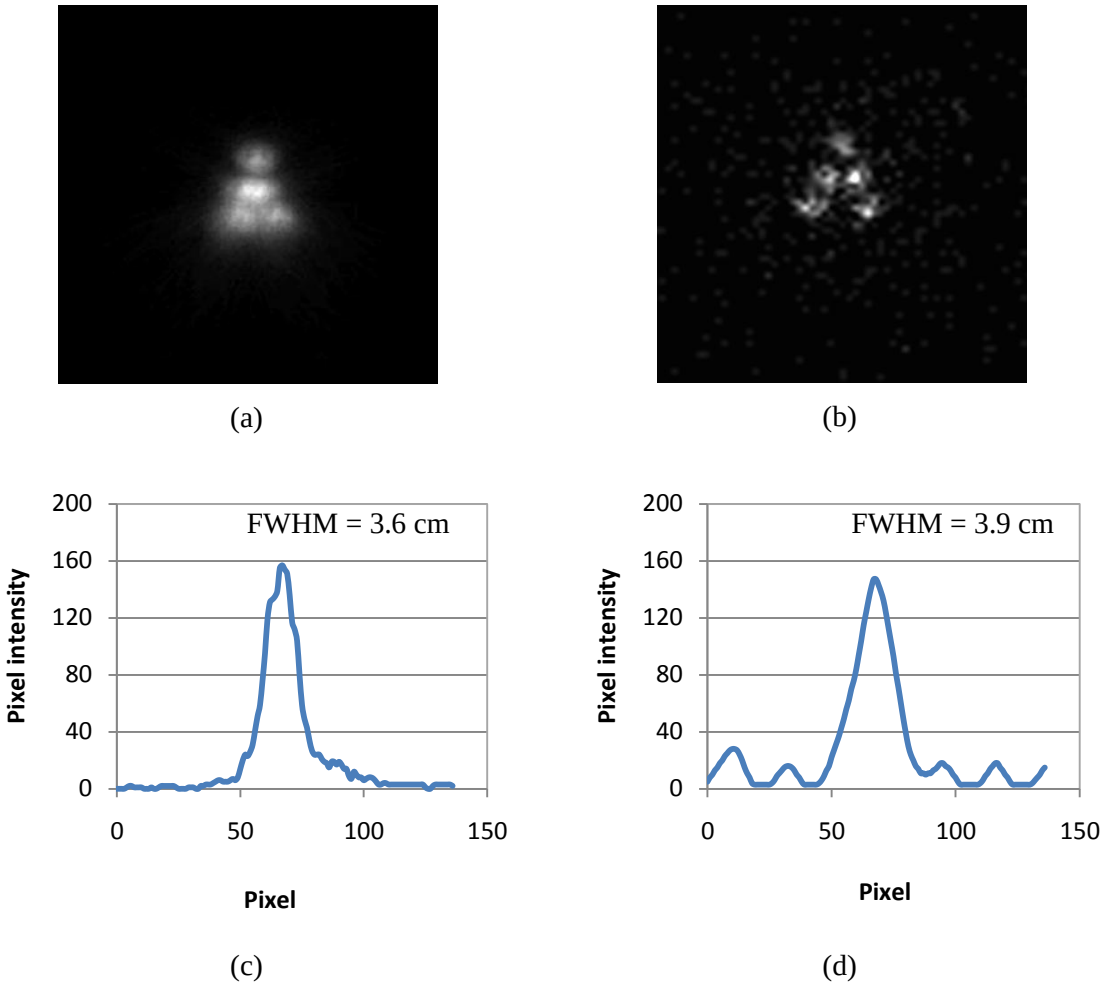

Figure 70: The triangles phantom filled with I131 (10MBq/tube) imaged by Compton system with 38,000 events (a) and gamma camera with 1900 events(b) along with the horizontal line profiles for Compton camera image (c) and gamma camera(d)

The results in Table 25 show that the SNR of the Compton camera image improved by a factor of 2 compared to gamma camera image. The contrast of Compton camera image is lower than the gamma camera due to small ROI area used in this comparison that enclosed most of the noise introduced by the Compton camera reconstruction method artifact. This has the effect of reducing the number of counts falling into the source profile peak relative to the background and thus reduces the contrast.

Nevertheless, the Compton camera sensitivity advantage resulted in decreasing the noise and, hence, improving the SNR. Han et al (2008) reported that the Compton camera

showed better noise performance than gamma camera when imaging source size below ~10 mm diameter size. Therefore, the results show that the Compton camera is a promising imaging system for I^{131} imaging that can provide an improved sensitivity and better noise performance than gamma camera, and hence, provides better diagnostic quality and increase patient comfort by decreasing the scanning time. This comparison can be improved by employing a more sophisticated image reconstruction algorithm e.g. MLEM as indicated by Han et al (2008) in order to improve the achievable image quality.

4 Conclusions and Future Work

This chapter summarizes the work and results presented in previous chapters. Conclusions are made based on experimental results and theoretical analysis. Future work for improving the Compton camera system design, imaging performance, image reconstruction algorithm and readout electronics are described.

4.1 Summary

The main goal of this research is to improve nuclear medicine imagining by using electronic photon collimation technique. In this study, an electronic collimation method based on Compton scattering imaging has been introduced and evaluated. The results presented in this work show how Compton scattered events in the Compton camera system may be successfully used for imaging. This thesis demonstrates the current performance of the UCL Compton camera system and provides a point from which additional development work may carry on. This is likely to focus on three main areas of the system; implementation of high-count-rate capabilities readout digital electronics, development of online data processing and PSA techniques and the innovation of sophisticated image reconstruction algorithms.

In Chapter 1, the general principles of gamma ray imaging in nuclear medicine, gamma camera, and PET were described. The physical limitations of current systems have been identified and compared to current approaches of improving camera performance. Then the principle, advantages, and the historical development of an electronic collimation technique based on Compton scattering physics have been demonstrated.

Chapter 2 demonstrate the materials and methods used in this work. The UCL HPGe prototype Compton camera design, specifications, and associated readout electronics were explained in details. The coincidence imaging operation mode, image reconstruction, and experimental setup have been demonstrated. In addition, the data analysis tools used to quantify the image quality was explained.

The results obtained for this work are shown in chapter 3. The results include the interaction probabilities, system performance characteristics and the imaging performance of the Compton camera with different source distributions. The results were interpreted quantitatively and compared to other cameras used in nuclear medicine.

Conclusions for the work presented in this work were drawn and future directions were defined in chapter 4.

4.2 Conclusions

The Compton camera offers many potential advantages for gamma-ray imaging applications. In principle, the Compton camera can provide better spatial resolution and sensitivity for high gamma-ray energies (>300 keV) compared to gamma camera. Therefore, a variety of high energy possible applications can benefit from Compton imaging: including I^{131} (364 keV) for thyroid and monoclonal antibodies, In^{113m} (393 keV) which can be used as a substitute for In^{111} to label blood cells in order to investigate infections and inflammation sites, and positron emitting isotopes.

Although there are a number of limitations in the current prototype camera some potentially useful qualities have been demonstrated and distributed sources have been imaged. This thesis shows that the multiple-view technique results in a significant improvement in the image quality by minimizing the image geometrical distortion and is

an effective way to accurately reconstruct the source distribution, and hence, provides a practical way to the Compton camera development research field to improve the quality of the images obtained. To the best of my knowledge, this work present experimentally for the first time the ability of a Ge Compton camera for quantitative I^{131} and F^{18} phantom imaging . In addition, a quantitative comparison between Compton camera and gamma camera for I^{131} imaging and with PET scanner for F^{18} imaging was carried out. This work confirmed that the Compton camera can be used with a factor of 2 improvements in the SNR compared to the mechanically collimated gamma camera for I^{131}. Even though PET scanner outperforms the Compton camera in 511 keV imaging, the Compton camera in principle can provide an alternative portable imaging system with high spatial resolution and sensitivity for 511 keV imaging. A portable system provides the possibility of obtaining intra-operative images that can help to confirm the location of lesion and whether it is correctly removed. Thus, avoiding future surgical procedures. More focus is needed by the Compton camera researchers to the potentials of the camera with these two widely used nuclear medicine radioisotopes.

The key limitations in the current prototype are acquisition time, processing time and image reconstruction. The current arrangement for the readout electronics employed in this camera have shown significant limitations at high count rates, which has lead to long acquisition times in the current prototype. However, techniques are available to significantly improve this and an improved parallel approach is currently being implemented. The offline post-processing method to select coincidence events currently being used also is time consuming. The system collects the deposited charge in all pixels regardless of where the interaction actually occurred and then converts it to digital numbers before passing them to a PC sequentially. Thus, this method results in a high

dead time, pulse pileup, and a data bottle neck. A fast online coincidence events selection algorithm is also being developed.

Theoretical investigation of the probabilities of interaction with the scatter and absorber detectors was carried out. The results showed that the energy deposited in the both detectors is a function of source energy and with using high source energy (>360 keV) more than 90% of the photons will interact with the detectors by Compton scattering. Based on the calculated front energies in Table 9 the energy threshold was set to 10 keV for all measurement (unless mentioned) to accept only gamma-ray photons scattered by > 20° in the front detector and minimize the detector noise effect. The uncertainty in measuring the scatter angle increases by using low gamma-ray source energy due to the very little energy measured in the front detector as well as the effect of Doppler broadening.

The camera performance characteristics were investigated. The energy resolution for the camera achieved using the MWD energy extraction algorithm is 1.2 % and 0.7% for 356 and 662 keV respectively. The results showed that energy resolution values depend strongly on the width of the deconvolution window and a minimum window of 8 μs is needed to obtain good energy resolution, and the best FWHM was obtained with 11 μs window.

The angular resolution was estimated theoretically using Singh's (1983) formulas and measured experimentally by imaging different point source energies. The theoretical estimation showed that the angular uncertainty is dominated by the geometrical contribution of the detectors. Different radioisotope point sources (Ba^{133}, Na^{22}, and Cs^{137}) were imaged and reconstructed for the first time with the UCL camera. The measured FWHM at 5 cm are 7.5, 7.2, and 6.9 ± 2 mm for 356, 511 and 662 keV gamma energies

respectively which translate to angular resolutions 8.5°, 8.2°, and 7.8° for 356, 511 and 662 keV gamma energies respectively.

The disagreement between theoretical and experimental values is due to the fact that the effect of the random events, dead time, and the reconstruction algorithm decoding penalty were not considered in the theoretical calculation. In addition, The results show that the spatial resolution is distance dependent.

Due to the limited active area and readout electronics a technique to reconstruct the point source image with a uniform symmetric distribution by acquiring multiple views was carried out. The results show that this technique improved the image spatial resolution. This technique was used to maximize the information yield from Compton camera images and simulate the proposed full camera. This technique proved that the camera FWHM and SNR can be improved by populating the full camera pixels.

The camera imaging performance with extended source distributions (line source, ring source, and Perspex phantom) were investigated and imaged and successfully reconstructed. In addition, the results showed the ability of this system to resolve two point sources separated by 0.3 mm. Thus, this system has the potential to detect small lesions separated by few millimeters.

The measured intrinsic efficiency of the camera with the current limited pixel geometry is $3.5x10^{-10}$.The detection efficiency for the experimental measured efficiency is lower than theoretically estimated efficiency (in section 2.9.2) by five orders of magnitude due to the limited number of pixels (31 pixels) and the counting limitations of the system.

The system timing resolution was measured by taking the FWHM value for the coincidence-timing spectrum shown in Figure 42. The measured system electronic time resolution is about 70 ns. Therefore, the coincidence time window was set to 75 ns which

are sufficient to pass most of the true coincidence events. The SNR improves linearly with decreasing the time window width due to the improved true/random events ratio while scarifying the number of coincidence counts decrease.

The count rate performance of the system is limited by the relatively slow readout electronics as revealed by the poor timing resolution. Under high incident photons flux or with increasing the number of active pixels bottle neck behaviour in the data output pipe was observed. From Figure 46 it can be noticed that the maximum data rate is ~ 1.85 Mbytes/sec which translates to 31 counts per second. The estimated system dead time is 32 milliseconds. The results show that the counting performance has strong dependence on the number of back pixels compared to the front pixels due to the fact that the back pixels are used to initiate triggering and readout sequences.

The faction of scatter photons detected depends mainly on the density of the scattering medium, source energy, the depth of the source, detector energy resolution and the energy window width. The scatter fraction increases with increasing the energy window width. Using narrow energy window width is possible with the excellent germanium energy resolution but at the expense of sensitivity.

The images in section 3.5 present the first images of Fluorine-18 and Iodine-131 obtained with the UCL prototype Compton camera. The expected phantom shape and insert locations were successfully reconstructed. The intensity of the inserts varies according to their position relative to the active front detector pixels due to the fact that the camera sensitivity varies with the source position. However, a correction factor was applied for the top and bottom row of inserts to compensate for the intensity variations. The resolution degradation for Iodine-131 imaging is mainly due to the effect of Doppler

broadening. The theoretical calculations of the angular uncertainty due to the Doppler broadening indicates that at 360 keV the effect of Doppler broadening on the angular uncertainty is a factor of 3 more than its effect at 662 keV source energy. These results showed the feasibility of using Compton camera for nuclear medicine studies providing that the current prototype limitations are treated.

A comparison between the imaging performances of the prototype Compton camera to a commercially available PET camera is presented in (section 3.5.1). The images were reconstructed by simple backprojection algorithm. However, different algorithms were used for each image due to the difference in response function of each scanner. The results show that PET qualitatively outperforms the Compton camera at 511 keV imaging and achieves 4 times better SNR. Although the comparison provides valuable information about the relative performance of the Compton camera compared to PET, the comparison has some limitation. Firstly, some corrections could not be disabled while acquiring the PET image, and hence, adds an advantage for PET over Compton camera image. In addition, the angular sampling in PET is superior since the detection area is bigger (64 detectors) i.e. 64 views compared to the limited number of views with the Compton camera. Finally, the backprojection algorithm used to reconstruct PET image is more sophisticated than the crude reconstruction algorithm used for Compton camera images. Therefore, this comparison can be improve by using a statistical image reconstruction method (e.g. MLEM) or analytically simulate both systems and use the same number of counts for image reconstruction with disabling all filters and corrections in PET to have like with like comparison.

Section 3.5.2 compares the imaging performance of the conventional gamma camera to the Compton camera for I^{131} imaging. The results show that the gamma camera outperforms the Compton camera for I^{131} imaging when the same number of counts is

used for reconstruction. This is mainly due to the effect of Doppler broadening on angular resolution at 360 keV and the confound influence of the image reconstruction algorithm used for Compton camera. However, the attractive aspect of Compton camera is that the sensitivity can increase without scarifying the resolution. The Compton camera is expected in principle to have 20 times better sensitivity than gamma camera for detecting 360 keV photons in the same acquisition time (Han et al 2008). Therefore, another comparison was done by comparing Compton image with 20 times more counts than gamma camera image. The results show that the SNR of the Compton camera image improved by a factor of 2 compared to the gamma camera image.

Assuming that a much better electronics system and image reconstruction is used the the spatial resolution and sensitivity achievable with the current system is only dependent upon its geometry and detector material which will affect the ultimate imaging performance of the system. The system geometry impose a limitation on the angular resolution and sensitivity. As discussed in section…. that the pixels width, thickness, and the separation between the detectors results in an inherent angular uncertainty of 3° for all measurements. Also, the sensitivity of the system is limited by the small thickness of the back detector which results in transmitting most of the photons incident toward the back detector without interaction and hence, reduce the sensitivity of the system. Another factor that affects the sensitivity of the system is the high number of single events in the back detector due to the camera geometry. Based on the results presented in this thesis, I believe that the camera geometry is not optimal and future development should have an optimized geometry such that the detectors thicknesses and coverage area increase and the detectors setup in an adjustable separation which can be modified according to the required application e.g. for high sensitivity imaging the separation should be reduced and increased for high angular resolution.

According to the results obtained in this work the most promising clinical area that can benefit from Compton imaging is high energy >300 keV imaging including: I^{131} studies for diagnosing and following up thyroid diseases, monoclonal antibodies, In^{113m} (393 keV) which can be used as a substitute for In^{111} to label blood cells in order to investigate infections and inflammation sites, and positron emitting isotopes. Also, Compton camera can be used for radiotherapy dose reconstruction by imaging prompt gamma- ray during ion beam and proton therapy to accurately the range of the beam (Mundy and Herman 2010). Thus, the future should see more focus in this field.

4.3 Future work

The work presented in this dissertation is part of ongoing research to achieve the long term goal of developing a compact portable imaging system to image gamma-ray emissions in nuclear medicine examinations with high spatial resolution and detection sensitivity. Even though preliminary conclusions have been drawn, there are several improvements to be made for our Compton camera and performance assessment studies. These improvements are described in the following paragraphs.

The long conversion time and data transfer time has significantly increased the system dead time, which substantially decreases sensitivity. The current readout electronics showed counting limitation especially with high count rate, thus improving the readout electronics is critical. The readout electronics should be customized to handle high count rate without significant pulse pileup and low noise to allow for high energy resolution measurement. Future designs need to improve data conversion and transfer speed.

In addition, fast pulse shaping is required for coincidence detection. An interesting approach that might provide a solution for the counting limitation with the GRT4 has been developed by (Cajipe et al 2008) . They developed a chip called RENA (Readout Electronics for Nuclear Applications) which has multi-channel charge sensitive amplifier for reading position sensitive solid state detectors and can potentially provide an enhanced counting capabilities. The new readout system should allow data taking at about twice the present rate.

The cooling requirements for Ge make it an undesirable choice for a clinical environment. The ongoing development of mechanically cooled HPGe detectors (Upp et al 2005) may relieve operational problems associated with liquid Nitrogen cooling easing the integration of HPGe-based devices into any clinical imaging systems. Other detectors

with good energy resolution e.g. CZT that doesn't require cooling process is more desirable especially if used as a back (absorption) detector (Harkness et al 2009).

Image reconstruction for Compton camera data is challenging and work is needed for fast, efficient algorithms suitable for clinical use. Although list mode backprojection reconstruction is simple and fast, in Compton scatter imaging the intersection of the backprojected ellipses and the source plane results in image error or artefacts. Iterative algorithms like MLEM (Maximum Likelihood Expectation Maximization) or ordered subset expectation maximization (OSEM) could be used to overcome these problems and result in a correct estimate of the source activities and location particularly for extended source distribution (Parra 2000). They are however computationally intensive and their convergence points can be ambiguous (Wieczorek 2010). A possible alternative solution could be provided using the stochastic origin ensembles (SOE) algorithm (Andreyev et al 2010).

Since this system is intended to be used clinically, it is critical to develop attenuation and random reduction techniques for Compton camera similar to those used in SPECT and PET. Similar to PET cameras, transmission scans can be used to generate attenuation maps .Compton camera suffers from random coincidence events similar to PET system. One correction approach is to acquire delayed coincidence sinogram to correct for random events. Further research is required to determine whether the delayed window approach can be applied for Compton cameras and whether random coincidences can be corrected by approximating the distribution of random coincidence measurements in the system and incorporate it to image reconstruction. Alternatively, a statistical model developed to estimate the attenuation and random events and use them as a priori information that can be incorporated in the reconstruction process.

Currently, the data-acquisition software is unstable and crushes frequently. Using this software requires familiarity with Linux to initiate the MVEM5500 power PC card and the acquisition software. Another issue to pay attention to is the long data transfer time between the detector and the computer. A future design could improve the speed significantly by developing online coincidence selection by programming the FPGA with an online filtering algorithm. By using this method the circuit will only reads out the two pixels in which the event occurs. This new system will substantially reduce the data transfer time because only data associated with a few pixels will be transferred instead of all pixels. Along with faster ADCs, the system dead time is expected to decrease. In addition, live image reconstruction is desirable to optimize the system for clinical use. Thus, efficient data flow and data acquisition program will save time to exclusively collect good events.

The camera should be used to image radioisotopes with different energies simultaneously and prove its abilities e.g. imaging I^{131} and F^{18} at the same time. Also, the ability of Compton camera to take three-dimensional images from a fixed position and, therefore, does not require a large ring-type structure, making it possible to fit it into an existing CT or MRI system, without requiring major modification to the system. Thus, provides a hybrid imaging system for a combination of functional and anatomical imaging modalities that could provide better clinical care for patients.

In this research a preliminary measure of the system performance has been carried out with simulating the full system by using multiple views technique. However, the performance of an imaging system cannot be fully defined by only a few images acquired at different angles. The full camera pixels need to be populated and then experiments under a variety of conditions including: source energy, number of counts, test objects,

source distance, and effect of reconstruction method need to be carried out.These images will be useful in verifying performance predictions and the multiple views results.

Once the performance has been optimized, it is also necessary to take phantom images with background radiation or anthropomorphic phantoms that reflect real clinical situations and study the effect of the background radiation on the image quality. Before introducing the camera to the clinical arena, the system need to be assembled in a portable mode which can be easily done by placing the camera with its associated electronics in a heavy duty four wheels trolley. The final step will be nuclear imaging on human subjects. Qualitative and quantitative comparison between Compton cameras and conventional camera to determine which camera is better and in what specific area.

Appendix

Procedures for F^{18} experiment with Compton camera

LOCAL RADIATION PHYSICS X-RAY LAB RULES WILL BE FOLLOWED.

1. The phantom must only be filled with radioactive materials and sealed in the UCLH nuclear medicine department.
2. Then, the sealed phantom shall be placed in a shielded trolley (the phantom top should be shielded with a lead slab).
3. Move the phantom to the UCL x-ray lab(room 2.09).
4. In the UCL x-ray lab,
   - 4.1. Place the phantom inside the spill control tray beneath the Compton camera.
   - 4.2. Shield the area around the phantom .
   - 4.3. Set up a controlled area around the camera(2 meters diameter) by placing a barrier with clear signs of the radioactive material type and activity used.
   - 4.4. The dark room(room 2.09c) must be locked and remain empty during the experiment.
   - 4.5. Start the experiment.
   - 4.6. After finishing the experiment place the phantom in the shielded trolly and move it back to the UCLH nuclear medicine department for disposal.

In case of emergency contact the Radiation Protection Supervisors (RPS):

Prof. Robert Speller	or	Dr. Gary Royle
Room number: 2.05		Room number: 2.06
Internal: x0263		Internal: x0262

Phantom transportation Plan

1. The estimated time to transport the phantom from UCLH nuclear medicine dept to the UCL medical physics dept is *20 min*.
2. For 4.4 Mbq **Tc^{99m}** dose at 1 meter distance the cumulative dose is ***0.03uSv*** *per trip*.
3. For 4.4 Mbq **I^{131}** dose at 1 meter distance the cumulative dose is ***0.09uSv*** *per trip*.
4. For 200 Mbq **F^{18}** dose at 1 meter distance the cumulative dose is ***9.56uSv*** *per trip*.
5. Two people will be involved in the transportment, one pulling the trolley and the other at a distance of 2 meter behind. The 2 people will alternate pulling the trolley on successive trips. Thus, the cumulative dose will be reduced to half the values mentioned in the previous point when the job is shared by two.
6. A member of staff in the medical physics dept will be informed before and after the transportment with an estimated time of arrival.
7. The details of the transportment is (*refer to the attached map)* :-

(a) The phantom will be placed in a lead shielded carry case in UCLH NM dept(5^{th} floor) and then the stairs will be used to go to the ground floor. Then, the lead case will be placed in the trolly .

(b) Walk down Gower street towards Torrington place i.e. Chadwick building on the left hand side and Arthur Tattersal House on the right hand side. Avoid walking through pedestrian crowds.

(c) Then at the intersection between Gower street and Torrington place cross the pedestrian lane to the left and walk few meters down the road to reach Malet Place entrance on the left hand side.

(d) Enter Malet Place and go to Malet Place Engineering building (2^{nd} building on the left hand side) use the stairs and go to the 2^{nd} floor. Go to the x-ray lab (room 2.09).

CONTINGENCY PLANS

SPILLAGE – RESPONSE ACTIONS

In the event of spillage of radioactive substances that are likely to have potential for causing airborne or surface contamination, carry out the following actions:

1. Follow immediate action drills to isolate the spillage by applying absorbent material etc evacuate the immediate area and isolate the area concerned, closing doors, and windows.

2. Any suspected contamination of personnel or cuts or injuries sustained during the occurrence should be drawn to the immediate attention of supervisors and medical staff.
3. Prevent access to the area suspected of being contaminated (such as by erecting barriers and attaching warning notices).

4. Where personnel are suspected of being contaminated, they should firstly be assisted to remove and bag contaminated over garments (lab coats etc), then provided with coverall and overshoes if they need to be moved to a separate area for decontamination and monitoring.

(a) Equipment that can be re-used should be decontaminated, but if contamination remains the equipment should be appropriately marked and, if necessary, packaged. Materials and articles should be disposed of as radioactive waste if they are not to be re-used.

(b) Re-monitor the area to ensure that the levels of contamination are less than the maximum prescribed for normal operations in the area concerned. RPA advice may be necessary as to acceptable levels of residual contamination.

(a) Seek the advice of the RPA where contamination cannot be reduced to prescribed levels by repeated cleaning. When the area has been adequately decontaminated remove the additional barriers and allow return to normal procedures for access to the area.

Removal of personal contamination

The following actions should be taken by medical personnel as quickly as possible when a person with skin contamination arrives at the medical department.

- Moist-swab the skin with plain water (soap should not be used initially). When removing contamination from the face, swab away from the mouth, nose, eyes, ears and
  any wound. Contamination in any orifice may be removed by irrigation with normal saline
  or similar infusion, or even plain water. Care should be taken to ensure that the skin is not reddened or broken when removing contamination.

- If repeated monitoring indicates that the contamination is being removed the use of plain water should be continued. If not, soap or other detergent may be used.

- If the use of soap fails to reduce the contamination levels below limits recommended by the RPA, the appointed doctor should be consulted.

- All clothing, swabs and washings must be treated as potentially contaminated and retained
  for disposal through an appropriate waste disposal route.

Breakage kit

Each kit is to be clearly labeled so as to indicate its purpose and is to contain the following:

- 1 pair of rubber gloves.
- 1 pair of tongs or tweezers.
- Soft cloths.
- 1 small roll of adhesive tape.
- Disposal container (e.g. paint type tin) with sealable lid.
- Safety glasses/goggles.
- Bottle of water.

DECONTAMINATION AND CLEAN-UP

- After completing any immediate actions to minimise the decontamination hazard and clean-up is to be conducted as follows:

    - Put on rubber gloves and, if appropriate, wear safety glasses.

    - Pick up all visible fragments and other items liable to be contaminated, using tongs or
      Tweezers and place them in the disposal container.

    - Pick up small particles with adhesive tape, using only light pressure, and place adhesive tape in disposal container.

    - Dampen the cloth and wipe over the area in which the breakage has occurred, using light straight strokes to avoid rubbing particles into the surface being cleaned. Fold the cloth in half after each stroke, and keep the clean side out.

    - When the wiping surface of the cloth becomes too small, replace with the other clean dampened cloth. Place the cloth in the disposal container.

    - Remove rubber gloves. Place them in the disposal container and secure the lid.

    - Wash hands thoroughly.

Bibliography

Ahmed S N 2007 *Physics and engineering of radiation detection* (USA: Academic Press(Elsevier))

Alnaaimi M A, Royle G J, Ghoggali W, Banoqitah E, Cullum I and Speller R D 2011 Performance evaluation of a pixellated Ge Compton camera *Phys. Med. Biol.* **56** 3473-3486

Alnaaimi M, Royle G, Ghoggali W and Speller R 2010 Performance Evaluation of the UCL Compton Camera IEEE Nuclear Science Symposium and Medical Imaging Conference vol N41-150 (USA) pp 1104-1107

Andreyev A, Sitek A and Celler A 2011 Fast image reconstruction for Compton camera using stochastic origin ensemble approach *Med. Phys.* **38** 429

Anger H 1958 Scintillation Camera *Review of Scientific Instruments* **29** 27-33

Bateman J E, Connolly J F, Stephenson R and Flesher A C 1980 The development of the Rutherford laboratory MWPC positron camera *Nuclear Instruments and Methods* **176** 83-88

Beekman F and Have F 2006 The pinhole: gateway to ultra-high-resolution three-dimensional radionuclide imaging *Eur J Nucl Med Mol Imaging* **34** 151-161

Berger M J, Hubbell J H, Seltzer S M, Chang J, Zucker D.S., and Olsen K. 1990 XCOM: Germanium *NIST- XCOM: Photon Cross Sections Database http://www.nist.gov/pml/data/xcom/index.cfm*

Bergström s, holgersson g, bergqvist j-e, bergqvist m, ekman s and stenström M 2010 Dual-headed Coincidence PET vs. Dedicated PET/CT in the Evaluation of Thoracic Malignancies *In Vivo* **24** 235 -238

Bisogni M G, Collazuol G M, Marcatili S, Melcher C L and Del Guerra A. 2011 Characterization of Ca co-doped LSO:Ce scintillators coupled to SiPM for PET applications *Nuclear Instruments and Methods in Physics Research Section A: Accelerators, Spectrometers, Detectors and Associated Equipment* **628** 423-425

Blankespoor S C, Wu X, Kalki K, Brown J K, Tang H R, Cann C E and Hasegawa B H 1996 Attenuation correction of SPECT using x-ray CT on an emission-transmission CT system: Myocardial perfusion assessment *IEEE Transactions on Nuclear Science* **4** 2263-2274

Bolozdynya A, Ordonez C E and Chang W 1997 A concept of cylindrical Compton camera for SPECT vol 2 pp 1047-1051

Boston H C, Gillam J, Boston A J, Cooper R J, Cresswell J, Grint A N, Mather A R, Nolan P J, Scraggs D P, Turk G, Hall C J, Lazarus I, Berry A, Beveridge T and Lewis R 2007 Orthogonal strip HPGe planar SmartPET detectors in Compton configuration *Nuclear Instruments and Methods in Physics Research Section A: Accelerators, Spectrometers, Detectors and Associated Equipment* **580** 929 -933

Brownell and Sweet 1953 Localization of brain tumors with positron emitters *Nucleonics* **11** 40-45

Brzymialkiewicz C N, Tornai M P, McKinley R L and Bowsher J E 2005 Evaluation of fully 3-D emission mammotomography with a compact cadmium zinc telluride detector *IEEE Trans Med Imaging* **24** 868-877

Budinger T F 1998 PET instrumentation: What are the limits? *Seminars in Nuclear Medicine* **28** 247-267

Cajipe V B, Clajus M, Hayakawa S, Matteson J, James, Skelton, Tumer O T and Volkovskii, A 2008 Performance of the RENA-3 IC with position-sensitive CZT and CdTe detectors Nuclear Science Symposium Conference Record, 2008. NSS '08. IEEE vol 1 (Dresden, Germany) pp 300 - 307

Chiesa C, Negri A, Albertini C, Azzeroni R, Setti E, Mainardi L, Aliberti G, E Seregni E and Bombardieri E 2009 A practical dead time correction method in planar activity quantification for dosimetry during radionuclide therapy *Q J Nucl Med Mol Imaging* **53** *6 658-670*

Christensen N L, Hammer B E, Heil B G and Fetterly K 1995 Positron emission tomography within a magnetic field using photomultiplier tubes and lightguides *Phys Med Biol* **40** 691-697

Conti Maurizio 2009 State of the art and challenges of time-of-flight PET *Physica Medica* **25** 1-11

Conti Maurizio, Bendriem B, Casey M, Chen M, Kehren F, Michel C and Panin V 2005 First experimental results of time-of-flight reconstruction on an LSO PET scanner *Phys. Med. Biol.* **50** 4507-4526

Cooper R J, Boston A J, Boston H C, Cresswell J R, Grint A N, Mather A R, Nolan P J, Scraggs D P, Turk G, Hall C J, Lazarus I, Berry A, Beveridge T, Gillam J and Lewis R A 2007 SmartPET: Applying HPGe and pulse shape analysis to small-animal PET *Nuclear Instruments and Methods in Physics Research Section A: Accelerators, Spectrometers, Detectors and Associated Equipment* **579** 313 -317

Crespi F C L, Vandone V, Brambilla S, Camera F, Million B, Riboldi S and Wieland O 2010 HPGe detectors timing using pulse shape analysis techniques *Nuclear Instruments and Methods in Physics Research Section A: Accelerators, Spectrometers, Detectors and Associated Equipment* **620** 299-304

Dahlbom M, Schiepers C and Czernin J 2005 Comparison of Noise Equivalent Count Rates and Image Noise *IEEE Transactions on Nuclear Science* **52** 1386-1390

Daube-Witherspoon M E, Surti S, Perkins A, Kyba C C M, Wiener R, Werner M E, Kulp R and Karp J S 2010 The imaging performance of a LaBr3based PET scanner *Phys. Med. Biol.* **55** 45-64

Dedek N, Speller R D, Spendley P and Horrocks J A 2008 Performance Evaluation of 98 CZT Sensors for Their Use in Gamma-Ray Imaging *Nuclear Science, IEEE Transactions on* **55** 2689-2697

Derenzo S E, Weber M J, Bourret-Courchesne E and Klintenberg M K 2003 The quest for the ideal inorganic scintillator *Nuclear Instruments and Methods in Physics Research Section A: Accelerators, Spectrometers, Detectors and Associated Equipment* **505** 111-117

Descovich M 2002 *Improving the position resolution of highly segmented HPGE detectors using pulse shape analysis methods* Ph.D. Thesis (Oliver Lodge Laboratory: Liverpool)

Dewaraja Y K, Ljungberg M and Fessler J A 2006 3-D Monte Carlo-Based Scatter Compensation in Quantitative I-131 SPECT Reconstruction *IEEE Transactions on Nuclear Science* **53** 181-188

Dewaraja, Koral and Fessler 2009 Quantitative I-131 SPECT Reconstruction using CTSide Information from Hybrid Imaging *Nuclear Science Symposium Conference Record (NSS/MIC), 2009 IEEE* 2523 - 2529

Dolgoshein B, Balagura V, Buzhan P, Danilov M, Filatov L, Garutti E, Groll M, Ilyin A, Kantserov V, Kaplin V, Karakash A, Kayumov F, Klemin S, Korbel V, Meyer H, Mizuk R, Morgunov V, Novikov E, Pakhlov P, Popova E, Rusinov V, Sefkow F, Tarkovsky E and Tikhomirov I 2006 Status report on silicon photomultiplier development and its applications *Nuclear Instruments and Methods in Physics Research Section A: Accelerators, Spectrometers, Detectors and Associated Equipment* **563** 368-376

Du Y F, He Z, Knoll G F and Wehe D K 2000 Effects of mechanical alignment errors on Compton scatter imaging *IEEE Transactions on Nuclear Science* **47** 885-889

Du Y F, He Z, Knoll G F, Wehe D K and Li W 2001 Evaluation of a Compton scattering camera using 3-D position sensitive CdZnTe detectors *Nuclear Instruments and Methods in Physics Research Section A: Accelerators, Spectrometers, Detectors and Associated Equipment* **457** 203-211

Floyd C E, Jaszczak R J and Coleman R E 1988 Scatter detection in SPECT imaging: dependence on source depth, energy, and energy window *Phys. Med. Biol.* **33** 1075-1081

Georgiev A, Gast W and Lieder R M 1994 An analog-to-digital conversion based on a moving window deconvolution *IEEE Trans. Nucl. Sci.* **41** 1116-1124

Ghoggali W, Speller R D, Royle G J, Gabathuse J, Sellin P J, Lazarus I H and Appelbe D E 2004 Detector characteristics of a pixellated germanium Compton camera for nuclear medicine vol 4 pp 2216-2220

Giauque R D, Goulding F S, Jaklevic J M and Pehl R H 1973 Trace element determination with semiconductor detector x-ray spectrometers *Analytical Chemistry* **45** 671-681

Glick S J, Penney B C, King M A and Byrne C L 1994 Noniterative compensation for the distance-dependent detector response and photon attenuation in SPECT imaging *IEEE Trans Med Imaging* **13** 363-374

Goetze S, Brown T L, Lavely W C, Zhang Z and Bengel F M 2007 Attenuation Correction in Myocardial Perfusion SPECT/CT: Effects of Misregistration and Value of Reregistration *J Nucl Med* **48** 1090-1095

Guerra D A., Bandettini A, Conti M., De Pascalis G, Maiano P, Rizzo C and Perez Mendez V 1988 3-D PET with MWPCs: Preliminary tests with the HISPET prototype *Nuclear Instruments and Methods in Physics Research Section A: Accelerators, Spectrometers, Detectors and Associated Equipment* **269** 425-429

Del Guerra Alberto and Belcari N 2007 State-of-the-art of PET, SPECT and CT for small animal imaging *Nuclear Instruments and Methods in Physics Research Section A: Accelerators, Spectrometers, Detectors and Associated Equipment* **583** 119-124

Han L and Clinthorne Neal H. 2009 Performance Comparison and System Modelling of a Compton Medical Imaging System and a Collimated Anger Camera *Nuclear Science Symposium Conference Record.* 4553 - 4558

Han L, Rogers W Leslie, Huh S S and Clinthorne N 2008 Statistical performance evaluation and comparison of a Compton medical imaging system and a collimated Anger camera for higher energy photon imaging *Physics in Medicine and Biology* **53** 7029-7045

Harkness L J, Boston A J, Boston H C, Cooper R J, Cresswell J R, Grint A N, Nolan P J, Oxley D C, Scraggs D P, Beveridge T, Gillam J and Lazarus I 2009 Optimisation of a dual head semiconductor Compton camera using Geant4 *Nuclear Instruments and Methods in Physics Research Section A: Accelerators, Spectrometers, Detectors and Associated Equipment* **604** issue1 351-354**.**

Heller G 2004 American Society of Nuclear Cardiology and Society of Nuclear Medicine joint position statement: attenuation correction of myocardial perfusion SPECT scintigraphy *Journal of Nuclear Cardiology* **11** 229

Herzo D, Koga R, Millard W A, Moon S, Ryan J, Wilson R, Zych A D and White R S 1975 A large double scatter telescope for gamma rays and neutrons *Nuclear Instruments and Methods* **123** 583-597

Hirasawa M and Tomitani T 2004 Effect of compensation for scattering angular uncertainty in analytical Compton camera reconstruction *Phys. Med. Biol.* **49** 2083-2093

Hoffman E J, Huang S C and Phelps M E 1979 Quantitation in positron emission computed tomography: 1. Effect of object size *J Comput Assist Tomogr* **3** 299-308

Hsieh J, Molthen R C, Dawson C A and Johnson R H 2000 An iterative approach to the beam hardening correction in cone beam CT *Med. Phys.* **27** 23-30

Hua C H, Clinthorne N.H., Wilderman S J, LeBlanc J W and Rogers W.L. 1999 Quantitative evaluation of information loss for Compton cameras *Nuclear Science, IEEE Transactions on* **46** 587-593

Hua C 2000 *Compton imaging system development and performance assessment* Ph.D. Thesis (USA: University of Michigan)

J Gabathuse 2006 *Evaluation of the UCL Ge Compton camera Imaging Performance for Nuclear Medicine Applications* Ph.D. Thesis (University College London: Medical Physics Dept)

J. W. Leblanc, X. Bai, N. H. Clinthorne, C. Hua, D. Meier, W. L. Rogers, D. K. Wehe, P. Weilhammer and S. J. Wilderman 1999 99m Tc Imaging Performance of the C-SPRINT Compton Camera IEEE Nuclear Science Symposium, Conference Record. pp 545 - 552

Jong H de, F. B, M. V and Rijk P van 2002 Simultaneous 99m Tc/ 201 Tl dual-isotope SPET with Monte Carlo-based down-scatter correction *European Journal of Nuclear Medicine and Molecular Imaging* **29** 1063-1071

K Iniewski 2009 *Medical Imaging: Principles, Detectors, and Electronics* (USA: WILEY)

Kabuki S, Kimura H, Amano H and Nakamoto Y 2010 Imaging study of a phantom and small animal with a two-head electron-tracking Compton gamma-ray camera Nuclear Science Symposium Conference Record (NSS/MIC), 2010 IEEE pp 2844-2847

Kabuki S, Kimura H, Amano H, Nakamoto T and Kubo H. 2009 Imaging reagents study for nuclear medicine using an electron-tracking Compton gamma-ray camera Nuclear Science Symposium Conference Record (NSS/MIC), 2009 IEEE pp 2813-2816

Kabuki S., Hattori K, Kawashima, H., Kimura, R. K, Kubo, A and Kurosawa 2006 Development of a Electron Tracking Compton Gamma-Ray Camera Using a Gas Micro-Tracking Device for Nuclear Medicine Nuclear Science Symposium Conference Record (NSS/MIC), 2006 IEEE pp 2971-2975

Kabuki Shigeto, Kimura Hiroyuki, Amano Hiroo, Nakamoto Yuji, Kubo Hidetoshi, Miuchi K, Kurosawa S, Takahashi M, Kawashima H, Ueda M, Okada T, Kubo A, Kunieda E, Nakahara T, Kohara R, Miyazaki O, Nakazawa T, Shirahata T, Yamamoto E, Ogawa K, Togashi K, Saji H and Tanimori T 2010 Electron-tracking Compton gamma-ray camera for small animal and phantom imaging *Nuclear Instruments and Methods in Physics Research Section A: Accelerators, Spectrometers, Detectors and Associated Equipment* **623** 606-607

Kang M S, Lee D-H, Lee J, Lee J Y, Choi S-K and Park H S 2008 Dead time correction in coincidence counting of photon pairs *Metrologia* **45** 382-388

Kim, Lee J S, Lee C S, Kim C H, Lee M C, Lee D S and Lee S-J 2010 Fully three-dimensional OSEM-based image reconstruction for Compton imaging using optimized ordering schemes *Phys. Med. Biol.* **55** 5007-5027

Knoll G F 1999 *Radiation Detection and Measurements.* (Wiley: New York)

Krane K S 1988 *Introductory Nuclear Physics* (Wiley: New York)

Lanza A, Tombari F and Stefano L D 2010 Accurate and Efficient Background Subtraction by Monotonic Second-Degree Polynomial Fitting *Proceedings of the 2010 7th IEEE International Conference on Advanced Video and Signal Based Surveillance* AVSS '10 (Washington, DC, USA: IEEE Computer Society) pp 376–383

Lazarus I H 2006 GRT Card. Manual (version 3 revised Aug 2006)

Lazarus I H, Appelbe D E, Boston A J, Coleman-Smith P J, Cresswell J R, Descovich M, Gros S A A, Lauer M, Norman J, Pearson C J, Pucknell V F E, Sampson J A, Turk G and Valiente-Dobon J J 2004 The GRT4 VME pulse processing card for segmented germanium detectors Nuclear Science Symposium Conference Record *IEEE* **51** 1353-1357

Leblanc J W, Clinthorne N. H., Hua C-H, Nygard E, Rogers W. L., Wehe D K, Weilhammer P and Wilderman S J 1998 C-SPRINT: a prototype Compton camera system for low energy gamma ray imaging *IEEE Transactions on Nuclear Science* **45** 943-949

Lee S H, Seo H, An S H, Lee J S and Kim C H 2008 Performance evaluation of a table-top Compton camera for various detector parameters *Nuclear Instruments and Methods in Physics Research Section A: Accelerators, Spectrometers, Detectors and Associated Equipment* **591** 88 -91

van Lingen A, Huijgens P C, Visser F C, Ossenkoppele G J, Hoekstra O S, Martens H J, Huitink H, Herscheid K D, Green M V and Teule G J 1992 Performance characteristics of a 511-keV collimator for imaging positron emitters with a standard gamma-camera *Eur J Nucl Med* **19** 315-321

Liu Y, Ji Y, Ghosh K, Clark R A F, Huang L and Rafailovich M H 2009 Effects of fiber orientation and diameter on the behavior of human dermal fibroblasts on electrospun PMMA scaffolds *J Biomed Mater Res A* **90** 1092-1106

Lodge M A, Webb S, Flower M A and Binnie D M 1996 A prototype rotating slat collimator for single photon emission computed tomography *IEEE Trans Med Imaging* **15** 500-511

M Scannavini 2001 *Medical Compton Cameras Based On Semiconductor Detectors: Design And Expermintal Development* PhD thesis (London: University College London)

Madsen M T 2007 Recent Advances in SPECT Imaging *J Nucl Med* **48** 661-673

Martin J B, Dogan N, Gormley J E, Knoll G F, O'Donnell M and Wehe D K 1994 Imaging multi-energy gamma-ray fields with a Compton scatter camera *Nuclear Science, IEEE Transactions on* **41** 1019 -1025

Moehrs S, Del Guerra Alberto, Herbert D J and Mandelkern M A 2006 A detector head design for small-animal PET with silicon photomultipliers (SiPM) *Phys Med Biol* **51** 1113-1127

Moses W 2003 Time of flight in pet revisited *IEEE Transactions on Nuclear Science* **50** 1325-1330

Moses W W, Janecek M, Spurrier M A, Szupryczynski P, Choong W-S, Melcher C L and Andreaco M 2010 Optimization of a LSO-Based Detector Module for Time-of-Flight PET *IEEE Transactions on Nuclear Science* **57** 1570-1576

Mundy D W and Herman M G 2010 Uncertainty analysis of a Compton camera imaging system for radiation therapy dose reconstruction *Med. Phys.* **37** 2341

National Institutes of Health 2005 *ImageJ: Image Processing and Analysis in Java* (Bethesda, Maryland, USA) *http://rsbweb.nih.gov/ij/*

ORTEC 2011 Review of the Physics of Semiconductor Detectors *http://www.ortec-online.com/detectors/review_physics/intro.htm*

Oliver J F and Rafecas M 2010 Improving the singles rate method for modeling accidental coincidences in high-resolution PET *Phys. Med. Biol.* **55** 6951-6971

Ordonez C E, Bolozdynya A and Chang W 1997 Doppler broadening of energy spectra in Compton cameras vol 2 pp 1361-1365

Ott R J 1986 Emission computed tomography *J Med Eng Technol* **10** 105-114

Ott R J 1996 Imaging technologies for radionuclide dosimetry *Phys. Med. Biol.* **41** 1885-1894

Ott R J, Batty V, Webb S, Flower M A, Leach M O, Clack R, Marsden P K, McCready V R, Bateman J E, Sharma H and Smith A 1987 Measurement of radiation dose to the thyroid using positron emission tomography *Br J Radiol* **60** 245-251

Ott R J, Tait D, Flower M A, Babich J W and Lambrecht R M 1992 Treatment planning for 131I-mIBG radiotherapy of neural crest tumours using 124I-mIBG positron emission tomography *Br J Radiol* **65** 787-791

Ott R J 1993 Wire chambers revisited *Eur J Nucl Med* **20** (4) 348-358

Ottaviani G, Canali C and Quaranta A A 1975 Charge Carrier Transport Properties of Semiconductor Materials Suitable for Nuclear Radiation Detectors *IEEE Trans. Nucl. Sci.* **22** 192-204

Parra L C 2000 Reconstruction of cone-beam projections from Compton scattered data *Nuclear Science, IEEE Transactions on* **47** 1543-1550

Patton J A and Turkington T G 1999 Coincidence imaging with a dual-head scintillation camera *J. Nucl. Med* **40** 432-441

Pennant M, Takwoingi Y, Pennant L, Davenport C, Fry-Smith A, Eisinga A, Andronis L, Arvanitis T, Deeks J and Hyde C 2010 A systematic review of positron emission tomography (PET) and positron emission tomography/computed tomography (PET/CT) for the diagnosis of breast cancer recurrence *Health Technol Assess* **14** 1-103

Phillips G W 1995 Gamma-ray imaging with Compton cameras *Nuclear Instruments and Methods in Physics Research Section B: Beam Interactions with Materials and Atoms* **99** 674 -677

Pichler B J, Judenhofer M S, Catana C, Walton J H, Kneilling M, Nutt R E, Siegel S B, Claussen C D and Cherry S R 2006 Performance Test of an LSO-APD Detector in a 7-T MRI Scanner for Simultaneous PET/MRI *J Nucl Med* **47** 639-647

V. Pucknell 2004 *Multi instance data acquisition system (MIDAS) http://npg.dl.ac.uk/MIDAS/*

Rahmim A and Zaidi H 2008 PET versus SPECT: strengths, limitations and challenges *Nuclear Medicine Communications* **29** 193-207

Rault E, Vandenberghe S, Van Holen R, De Beenhouwer J, Staelens S and Lemahieu I 2007 Comparison of image quality of different iodine isotopes (I-123, I-124, and I-131) *Cancer Biother. Radiopharm* **22** 423-430

Reed W A and Eisenberger P 1972a Gamma-Ray Compton Profiles of Diamond, Silicon, and Germanium *Phys. Rev. B* **6** 4596

Rogers S S, Waigh T A, Zhao X and Lu J R 2007 Precise particle tracking against a complicated background: polynomial fitting with Gaussian weight *Phys. Biol.* **4** 220-227

Royle G J, Speller R D, Sellin P, Gabathuse J and Ghoggali W 2003 Development of a pixellated germanium Compton camera for nuclear medicine 2003 IEEE Nuclear Science Symposium Conference Record vol 5-1 pp 3687-3690

Saha G B 2010 *Basics of PET Imaging: Physics, Chemistry, and Regulations* (Springer)

Scannavini M G 2001 *Medical Compton Imaging Based On Semiconductor Detectors: Design And Experimantal Development* Ph.D. Thesis (UCL)

Selivanov V V, Picard Y, Cadorette J, Rodrigue S and Lecomte R 2000 Detector response models for statistical iterative image reconstruction in high resolution PET *IEEE Transactions on Nuclear Science* **47** 1168-1175

Seo H, Kim C H, Park J H, Kim J K, Lee J H, Lee C S and Lee J S 2010 Development of double-scattering-type Compton camera with double-sided silicon strip detectors and NaI(Tl) scintillation detector *Nuclear Instruments and Methods in Physics Research Section A: Accelerators, Spectrometers, Detectors and Associated Equipment* **615** 333-339

Shah K S, Grazioso R, Farrell R, Glodo J, McClish M, Entine G, Dokhale P and Cherry S R 2004 Position sensitive APDs for small animal PET imaging

Shao and Karp 1991 Cross-plane scattering correction-point source deconvolution in PET *Medical Imaging, IEEE Transactions on* **10** 234-239

Singh M. 1983 An electronically collimated gamma camera for single photon emission computed tomography. Part I: Theoretical considerations and design criteria *Medical Physics* **10** 421

Singh M. and Doria D 1983 An electronically collimated gamma camera for single photon emission computed tomography. Part II: Image reconstruction and preliminary experimental measurements *Medical Physics* **10** 428

Singh M. and Doria D 1985 Single photon imaging with electronic collimation *IEEE Trans. Nucl. Sci.; (United States); Journal Volume: NS-32:1; Conference: Nuclear science symposium, Orlando, FL, USA, 31 Oct 1984* **32** 843-847

Singh M., Leahy R, Brechner R and Hebert T 1988 Noise propagation in electronically collimated single photon imaging *IEEE Nuclear science symposium* **35** 772-777

Singh Manbir and Brechner R R 1990 Experimental Test-Object Study of Electronically Collimated SPECT *J Nucl Med* **31** 178-186

Solomon C J and Ott R J 1988 Gamma ray imaging with silicon detectors -- A Compton camera for radionuclide imaging in medicine *Nuclear Instruments and Methods in Physics Research Section A: Accelerators, Spectrometers, Detectors and Associated Equipment* **273** 787 -792

Sorenson and Phelps 1987 *Physics in Nuclear Medicine* (USA: W B Saunders)

Starck J L, Pantin E and Murtagh F 2002 Deconvolution in Astronomy: A Review *Publications of the Astronomical Society of the Pacific* **114** 1051-1069

Surti Suleman, Kuhn A, Werner Matthew E., Perkins A E, Kolthammer J and Karp Joel S. 2007 Performance of Philips Gemini TF PET/CT Scanner with Special Consideration for Its Time-of-Flight Imaging Capabilities *J Nucl Med* **48** 471-480

Takeda S, Aono H, Okuyama S, Ishikawa S-N, Odaka H, Watanabe S, Kokubun M, Takahashi T, Nakazawa K, Tajima H and Kawachi N 2009 Experimental Results of the Gamma-Ray Imaging Capability With a Si/CdTe Semiconductor Compton Camera *IEEE Transactions on Nuclear Science* **56** 783-790

Takeda S, Fukuchi T, Kanayama Y, Motomura S, Hiromura M, Takahashi T and Enomoto S 2010 Millimeter-order imaging technique from 100 keV to MeV based on germanium Compton camera Hard X-Ray, Gamma-Ray, and Neutron Detector Physics **7805** (San Diego, California, USA: SPIE) pp 780515-9

Todd R W, Nightingale J M and Everett D B 1974 A proposed γ camera *Nature* **251** 132-134

Tomitani Takehiro 1981 Image Reconstruction and Noise Evaluation in Photon Time-of-Flight Assisted Positron Emission Tomography *IEEE Trans. Nucl. Sci.* **28** 4581-4589

Upp D L, Keyser R M and Twomey T R 2005 New cooling methods for HPGE detectors and associated electronics *J Radioanal Nucl Chem* **264** 121-126

Vandenberghe S, Holen R V, Staelens S and Lemahieu I 2006 System characteristics of SPECT with a slat collimated strip detector *Phys. Med. Biol.* **51** 391-405

Vastenhouw B and Beekman F 2007 Submillimeter Total-Body Murine Imaging with U-SPECT-I *J Nucl Med* **48** 487-493

Vetter K, Burks M and Mihailescu L 2004 Gamma-ray imaging with position-sensitive HPGe detectors *Nuclear Instruments and Methods in Physics Research Section A: Accelerators, Spectrometers, Detectors and Associated Equipment* **525** 322 -327

Wagner J-M, Noo F and Clackdoyle R 2002 Exact inversion of the exponential x-ray transform for rotating slant-hole (RSH) SPECT *Phys. Med. Biol.* **47** 2713-2726

Webb S 1988 *The Physics of Medical Imaging* (New york: Taylor and Francis Group)

Wells K, Visvikis D, Ott R J, Zweit J (Royal M H, Bateman J E, Stephenson R, Connolly J and Tappern G Rutherford A L 1994 Performance of a BaF2-TMAE prototype detector for use in PET Nuclear Science Symposium and Medical Imaging Conference 41(2) pp 2737-2742

Wells K, Chiverton J, Partridge M, Barry M, Kadhem H and Ott B 2007 Quantifying the Partial Volume Effect in PET Using Benford's Law *IEEE Transactions on Nuclear Science* **54** 1616-1625

Wells K, Goswami B, Rahni A, Jones J, Alnowami M, Lewis E and Guy M 2010 A flexible approach to motion correction in nuclear medicine *Nuclear Science Symposium Conference Record (NSS/MIC), 2009 IEEE* pp 2534-2539

Wernick M N and Aarsvold J N 2004 *Emission tomography: the fundamentals of PET and SPECT* (Academic Press)

Wieczorek H 2010 The image quality of FBP and MLEM reconstruction *Physics in Medicine and Biology* **55** 3161-3176

Wilderman S J, Rogers W.L., Knoll G F and Engdahl J C 1998 Fast algorithm for list mode back-projection of Compton scatter camera data *Nuclear Science, IEEE Transactions on* **45** 957-962

Zaidi H and Hasegawa B 2003 Determination of the Attenuation Map in Emission Tomography *J Nucl Med* **44** 291-315

Zaidi H and Koral K F 2004 Scatter modelling and compensation in emission tomography *European Journal of Nuclear Medicine and Molecular Imaging* **31** 761-782

Zoglauer A. 2005 *First Light for the Next Generationof Compton and Pair Telescopes* PhD thesis (TU Munich)